ISSN 1854-0171

ACTA GEOTECHNICA SLOVENICA

2017/2
VOL. 14

ISSN: 1854-0171

ACTA GEOTECHNICA SLOVENICA

Ustanovitelji | Founders

Univerza v Mariboru, Fakulteta za gradbeništvo, prometno inženirstvo in arhitekturo
University of Maribor, Faculty of Civil Engineering, Transportation Engineering and Architecture

Univerza v Ljubljani, Fakulteta za gradbeništvo in geodezijo
University of Ljubljana, Faculty of Civil and Geodetic Engineering

Univerza v Ljubljani, Naravoslovnotehniška fakulteta
University of Ljubljana, Faculty of Natural Sciences and Engineering

Slovensko geotehniško društvo
Slovenian Geotechnical Society

Društvo za podzemne in geotehniške konstrukcije
Society for Underground and Geotechnical Constructions

Izdajatelj | Publisher

Univerza v Mariboru, Fakulteta za gradbeništvo, prometno inženirstvo in arhitekturo
Faculty of Civil Engineering, Transportation Engineering and Architecture

Odgovorni urednik | Editor–in–Chief

Bojana Dolinar — University of Maribor

Uredniki | Co–Editors

Jakob Likar	Geoportal d.o.o.
Janko Logar	University of Ljubljana
Borut Macuh	University of Maribor
Stanislav Škrabl	University of Maribor
Milivoj Vulić	University of Ljubljana
Bojan Žlender	University of Maribor

Posvetovalni uredniki | Advisory Editors

Heinz Brandl	Vienna University of Technology
Chandrakant. S. Desai	University of Arizona
Bojan Majes	University of Ljubljana
Pedro Seco e Pinto	National Laboratory of Civil Eng.

Lektor | Proof–Reader

Paul McGuiness

Naklada | Circulation

200 izvodov - issues

Cena | Price

25 EUR/letnik - 25 EUR/vol.; (50 EUR for institutions/za institucije)

Tisk | Print

Tiskarna Saje

Revija redno izhaja dvakrat letno. Članki v reviji so recenzirani s strani priznanih mednarodnih strokovnjakov. Baze podatkov v katerih je revija indeksirana: SCIE - Science Citation Index Expanded, JCR – Journal Citation Reports / Science Edition, ICONDA - The international Construction database, GeoRef. Izid publikacije je finančno podprla Javna agencija za raziskovalno dejavnost Republike Slovenije iz naslova razpisa za sofinanciranje domačih periodičnih publikacij.

Naslov uredništva | Address

ACTA GEOTECHNICA SLOVENICA
Univerza v Mariboru, Fakulteta za gradbeništvo, prometno inženirstvo in arhitekturo
Smetanova ulica 17, 2000 Maribor, Slovenija
Telefon / Telephone: +386 (0)2 22 94 300
Faks / Fax: +386 (0)2 25 24 179
E-pošta / E-mail: ags@uni-mb.si

Spletni naslov | web Address

http://www.fg.uni-mb.si/journal-ags/

The journal is published twice a year. Papers are peer reviewed by renowned international experts. Indexation data bases of the journal: SCIE - Science Citation Index Expanded, JCR – Journal Citation Reports / Science Edition, ICONDA- The international Construction database, GeoRef. The publication was financially supported by Slovenian Research Agency according to the Tender for co-financing of domestic periodicals.

VPLIVI RAZLIČNIH FAKTORJEV NA PRECEJANJE IN DVIGOVANJE ZEMLJE ZARADI VBRIZGAVANJA STISNJENEGA ZRAKA

Zang Yongge
Tianjin University,
State Key Laboratory of Hydraulic Engineering Simulation and Safety
Tianjin 300072, Ljudska republika Kitajska
E-pošta: zangyongge2011@163.com

Sun Dongmei *(vodilni avtor)*
Tianjin University,
State Key Laboratory of Hydraulic Engineering Simulation and Safety
Tianjin 300072, Ljudska republika Kitajska
E-pošta: sundongmei@tju.edu.cn

Feng Ping
Tianjin University,
State Key Laboratory of Hydraulic Engineering Simulation and Safety
Tianjin 300072, Ljudska republika Kitajska
E-pošta: fengping@tju.edu.cn

Stephan Semprich
Graz University of Technology,
Institute of Soil Mechanics and Foundation Engineering
8010 Graz, Avstrija
E-pošta: stephan.semprich@tugraz.at

Ključne besede

ohlapno povezani dvofazni pretok in geomehanski model; in-situ preskus zračnega pretoka; injektiranje s komprimiranim zrakom; večfazni pretok; dvigovanje tal; izguba zraka.

Izvleček

V tej študiji so bili, z uporabo in-situ preizkusa zračnega pretoka v Essnu, z numeričnimi simulacijami raziskani vplivi različnih faktorjev na večfazni pretok in dvigovanje zemlje med in po injektiranju s stisnjenim zrakom. Za simuliranje in situ preizkusa zračnega pretoka in primerjavo simuliranih in merjenih rezultatov smo uporabili ohlapno povezan dvofazni pretok in geomehanski modelni pristop, ki povezuje dve programski kodi (TOUGH2/EOS3 in FLAC^{3D}). Ko se stisnjen zrak vbrizga, teče navzgor in bočno, vertikalna efektivna napetost blizu in nad injektiranimi območji pa se zmanjša zaradi povečanja pornega tlaka, kar povzroča razširitev ogrodja zemljine v pripadajočih območjih. Dvigovanje zemlje, ki ga povzročajo predvsem podporni vplivi iz nižjih deformiranih zemljin, je pomemben za porazdelitev povečanj poroznosti v notranjosti zemljine in se hitro povečuje med vbrizgavanjem zraka. Ko se stisnjen zrak zaustavi, se dvigovanje zemlje zaradi razpršitve nadtlaka postopoma zmanjšuje do nič. S kombinacijo intenzivnih padavin je dvigovanje zemlje nekoliko večje v bližini vrtine, znatno večje pa na oddaljenosti od vrtine kot je v primerih brez ali majhnih padavin. Pri tem stopnja vbrizgavanja zraka ostaja skoraj nespremenjena zaradi nespremenljivih pornih tlakov v bližini območja injiciranja. Ko se osnovna prepustnost povečuje ali tlak vstopnega zraka zmanjša v vbrizganih slojih, se povečata tako dvig zemlje kot tudi hitrost vbrizgavanja zraka. Čas, ki je potreben za dvigovanje zemlje, se približa vrednosti nič, če je rahlo pospešen z majhno prepustnostjo ali visokim vstopnim zračnim tlakom.

IMPACTS OF DIFFERENT FACTORS ON SEEPAGE AND LAND UPLIFT DUE TO COMPRESSED-AIR INJECTION

Zang Yongge
Tianjin University,
State Key Laboratory of Hydraulic Engineering Simulation and Safety
Tianjin 300072, China
E-mail: zangyongge2011@163.com

Sun Dongmei *(corresponding author)*
Tianjin University,
State Key Laboratory of Hydraulic Engineering Simulation and Safety
Tianjin 300072, China
E-mail: sundongmei@tju.edu.cn

Feng Ping
Tianjin University,
State Key Laboratory of Hydraulic Engineering Simulation and Safety
Tianjin 300072, China
E-mail: fengping@tju.edu.cn

Stephan Semprich
Graz University of Technology,
Institute of Soil Mechanics and Foundation Engineering
8010 Graz, Austria
E-mail: stephan.semprich@tugraz.at

Keywords

loosely coupled two-phase flow and geo-mechanical model; in-situ, air-flow test; compressed-air injection; multiphase flow; land uplift; air loss

Abstract

In this study, using an in-situ, air-flow test in Essen, the impacts of different factors on multiphase flow and land uplift during and after compressed-air injection were investigated using numerical simulations. A loosely coupled, two-phase flow and geo-mechanical modeling approach, linking two numerical codes (TOUGH2/EOS3 and FLAC^{3D}) was employed to simulate the in-situ, air-flow test for comparing the simulated and measured results. As the compressed air is injected, it flows upwards and laterally, and the vertical effective stress near and above the injection zones decreases owing to the pore pressure increasing here, causing an expansion of the soil skeleton in the corresponding zones. The land uplift, induced mainly by support actions from lower deformed soils, is relevant to the distribution of the porosity increments in the soil interior, and it increases rapidly during air injection. After the compressed-air injection stops, the land uplift decreases gradually to zero due to the overpressure dissipation. With a combination of intensive rainfall, the land uplift is slightly greater near the borehole, but it is significantly greater at a distance from the borehole than the land uplift with no or low rainfall, but the air-injection rate remains almost unchanged due to the unchangeable pore pressure near the injection region. As the intrinsic permeability increases or the air entry pressure decreases in the injected strata, both the land uplift and the air-injection rate increase, but the time required for the land uplift to become zero is slightly advanced with either a small permeability or a high air entry pressure.

1 INTRODUCTION

During tunnel construction below the groundwater table, due to the relatively higher groundwater pressure and the greater hydraulic conductivity, the pore-water in soil voids flows into the work space through the excavated surface, which may hinder the progress of the construction or even cause the collapse of the tunnel. It would, therefore, be advantageous to apply the compressed-air technique during the tunnel's construction [1-2]. By introducing pressurized air into the tunnel space, the groundwater inflow through the excavated surface could be prevented and the surface settlement can also be reduced, which is very critical in an urban area where the damage of settlements on the existing buildings must be concerned. It is important to note that the applied compressed-air pressure in the tunnel space must be equal to or greater than the magnitude of the groundwater pressure at the tunnel invert, so that the compressed air can permeate into the surrounding soils due to the pressure gradient. In

addition to this application, subsurface fluid injection has been applied extensively for energy development and environmental management, such as enhancing oil production, storing useful gas or oil in depleted gas/oil fields, recharging an over-drafted aquifer system, arresting or mitigating land subsidence, and disposing of contaminants and hazardous wastes, and other applications [3-6].

Actually, these applications of pressurized fluid injection all involve an interaction between multiphase fluid flow and geo-mechanical processes, and they could affect the variation of the seepage and the stress state in the porous media [5, 7-9]. The simultaneous consideration of the gas phase, liquid phase, and solid phase underground could therefore produce a more realistic result. Numerical analyses, compared to analytical solutions, can dispose of the complicated initial and boundary conditions, the multi-layered soils and the complex geometry of many engineering problems, and is a better choice to analyze the coupling processes between multiphase fluid flows and soil deformation. Selvadurai and Kim developed a mathematical solution to study the caprock-storage formation interactions during the injection of fluids into a poroelastic storage formation and the ground subsidence caused by the uniform extraction of fluids from a disc-shaped region [10-11]. A loosely coupled methodology, linking two numerical codes (TOUGH2, used for solving multi-phase multi-component flow equations [12]; and FLAC^{3D}, used for solving geo-mechanical, stress-strain equations [13]), was proposed by Rutqvist et al. [14] and Rutqvist and Tsang [15] to simulate the interactive processes between the geo-mechanical and fluid-flow processes. This coupled simulator has been widely applied in many geo-environmental situations, such as nuclear waste disposal, CO_2 sequestration, geothermal energy extraction, naturally occurring CO_2 upwelling with surface deformations, and gas production from hydrate-bearing sediments [16-20].

Therefore, in this study, on the platform of the in-situ, air-flow test in Essen conducted by Kramer and Semprich [1], the water-air, two-phase flow processes and soil deformation during and after compressed-air injection were investigated using the coupled TOUGH2-FLAC^{3D} simulator. Notably, the in-situ, air-flow test was carried out to explore the behavior of the outcropping soils before the subway construction using the compressed-air technique in Essen, Germany. Then, the impacts of the different factors on the multiphase flow and land uplift during and after compressed-air injection were analyzed, including the occurrence of a rain event, and a sensibility analysis of the values of the permeability and air entry pressure of the injected strata.

2 COUPLING PROCEDURES

TOUGH2/EOS3 is a module in TOUGH2 for non-isothermal, water-air, two-phase flow in three-dimensional, unsaturated-saturated porous and fractured media, in which the transformation and dissolution processes occurring between the liquid and gas phases are explained by mass-balance equations. These balance equations are discretized in space by the integral finite difference and in time by the first-order finite difference. FLAC^{3D} is a three-dimensional and explicit finite-difference computer code for solving geo-mechanical stress-strain equations. In the coupled two-phase flow and geo-mechanical process, the seepage process affects the stress field by changing the pore pressure and the effective stress, whereas the stress field affects the seepage through changing the porosity, the capillary pressure and the intrinsic permeability.

2.1 Update of Geo-mechanical Variables

In the loosely coupled procedure, the pore water pressure p_l, the pore air pressure p_g, and the liquid saturation S_l provided by TOUGH2 (the pore pressure is referred to the local atmospheric pressure, and the same below) are sent to FLAC^{3D} to calculate the average pore pressure p[14]:

$$p = S_l p_l + (1 - S_l) p_g \qquad (1)$$

This expression for the average pore pressure is applied to porous sedimentary rock [14, 21], and the medium was assumed to be porous media in this study. Then, the average pore pressure is incorporated into the calculations of the soil skeleton stress, the strain, and the effective stress σ_{ij}' ($\sigma_{ij}' = \sigma_{ij} - p\delta_{ij}$, where σ_{ij}' is the total stress and δ_{ij} is the Kronecker function (for $i = j$, $\delta_{ij} = 1$; for $i \neq j$, $\delta_{ij} = 0$)). The change in porosity $d\phi$ induced by the soil deformation can be expressed as follows:

$$\begin{aligned} d\phi = d(V_p / V_t) = (V_t dV_p - V_p dV_t) / V_t^2 = \\ = dV_p / V_t - \phi_0 dV_t / V_t \end{aligned} \qquad (2)$$

where V_p is the pore volume, V_t is the total volume, and ϕ_0 is the initial porosity at the initial stress. The total volume V_t is equal to the sum of the pore volume V_p and the solid grain volume V_s. Here, it is assumed that the deformation of the solid grains is much less than that of the soil skeleton, and can be negligible. Therefore, the change in the total volume V_t is equal to the change in the pore volume V_p, i.e., $dV_t = dV_p$, and the change in porosity $d\phi$ can be given by

$$d\phi = (1 - \phi_0) dV_t / V_t = (1 - \phi_0) \varepsilon_v \qquad (3)$$

where ε_v is the volumetric strain.

2.2 Update of Hydraulic Variables

The geo-mechanically induced $d\phi$ has an immediate effect on the fluid flow behavior, including the intrinsic permeability and the capillary pressure. The Kozeny-Carman Equation suggests that there should be a linear relation between the hydraulic conductivity k (or the intrinsic permeability K, $k = K\gamma_w / \mu_w$, where γ_w is the unit weight of water and μ_w is the dynamic viscosity of water) and $e^3/(1+e)$ (or $\phi^3/(1-\phi)^2$, where e is the void ratio and ϕ is the porosity) of porous materials. Furthermore, according to Chapuis and Aubertin [22], the Kozeny-Carman Equation predicts the hydraulic conductivity of most soils (for 10^{-1} to 10^{-11} m/s) fairly well and can be applied to the soils encountered in this study. Hence, for a given soil, the ratio of the intrinsic permeability $K_n(\phi_n)$ at the time step n to the initial intrinsic permeability $K_0(\phi_0)$ can be expressed as follows:

$$\frac{K_n}{K_0} = \frac{\phi_n^3 / (1-\phi_n)^2}{\phi_0^3 / (1-\phi_0)^2} \qquad (4)$$

where ϕ_n is the porosity at the time step n. Therefore, the intrinsic permeability K_n at the time step n can be defined with Eq. (5). This relationship has also been used by Taylor to estimate the unknown hydraulic conductivity at a porosity from a known hydraulic conductivity at another porosity for the same soil [23].

$$K_n = K_0 \left(\frac{\phi_n}{\phi_0} \right)^3 \left(\frac{1-\phi_0}{1-\phi_n} \right)^2 \qquad (5)$$

According to Rutqvist and Tsang [15], with respect to porous media, the capillary pressure is scaled with the intrinsic permeability and porosity according to a function by Leverett [24].

$$p_{cLn} = p_{cn} \frac{\sqrt{K_0 / \phi_0}}{\sqrt{K_n / \phi_n}} \qquad (6)$$

where p_{cLn} is the corrected capillary pressure at the time step n and p_{cn} is the calculated capillary pressure dependent on the liquid saturation at the time step n.

2.3 Coupling Procedure

The loosely coupling process between TOUGH2 and FLAC^{3D} is typically developed according to the procedure in Fig.1. Some input data files for TOUGH2 and FLAC^{3D}, such as the soil properties, mesh, boundary and initial conditions, must be initially prepared. Then TOUGH2 is executed for a sufficient simulation time to obtain an initial steady state, and FLAC^{3D} is also operated under gravitational loads to establish initial equilibrium stress gradients and outputs the initial porosity ϕ_0 of each element. Hereafter, the coupling process of TOUGH2-FLAC^{3D} starts. The initial porosity ϕ_0 from the FLAC^{3D} element is mapped to the TOUGH2 element, which is used to update the intrinsic permeability according to Eq.5. TOUGH2 is firstly executed for the first time-step, and the capillary pressure is corrected using Eq.6. When convergence is reached at the end of this time-step, the pore water pressure p_l , the pore air pressure p_g , and the liquid saturation S_l of each element in TOUGH2 are obtained and are mapped to the FLAC^{3D} nodes using a weighted distance interpolation. Then FLAC^{3D} runs under loads of average pore pressure for each node (which can be calculated using Eq.1), until an equilibrium state is reached. At this point the change in the porosity at the FLAC^{3D} element can be calculated according to the strain increment (by Eq.3). Afterwards, the updated porosity at the FLAC^{3D} element is sent back to the TOUGH2 element by interpolation. Utilizing the updated porosity, the intrinsic permeability is updated again according to Eq.5, and TOUGH2 is executed for the next time-step. And then the above coupling processes are repeated until the specified simulation time (Sum-time) is reached.

3 EXPERIMENT AND NUMERICAL SIMULATION OF THE IN-SITU AIR-FLOW TEST IN ESSEN

3.1 Description of the In-situ Air-Flow Test

An in-situ, air-flow test was carried out by Kramer and Semprich [1] to investigate the air permeability of the Essen soil, determine the extent of the airflow field, and analyze the effect of compressed airflow on the deformation of the soil skeleton and in particular on the surface displacement. Fig. 2 shows a schematic diagram of the experimental setup for the in-situ, air-flow test. According to the description of the related experiment [1], the soil profile in Essen can be divided into the following four distinct layers: a fill layer, a thick silt layer, a thin permeable sand layer and a thick layer of marl that is rather weathered in the upper region and presents pronounced joints. The groundwater table is approximately 4.75 m below the ground surface and is located in the silt layer.

Compressed air can be introduced into the ground through a 1.5-m diameter borehole in the injection well. A thin steel pipe can be installed inside the borehole, the lower part of the pipe being perforated for air permeating into soils and the top of the pipe being connected to an air compressor (which was used to control the air pressure) [1]. In test 1B under consideration here, the

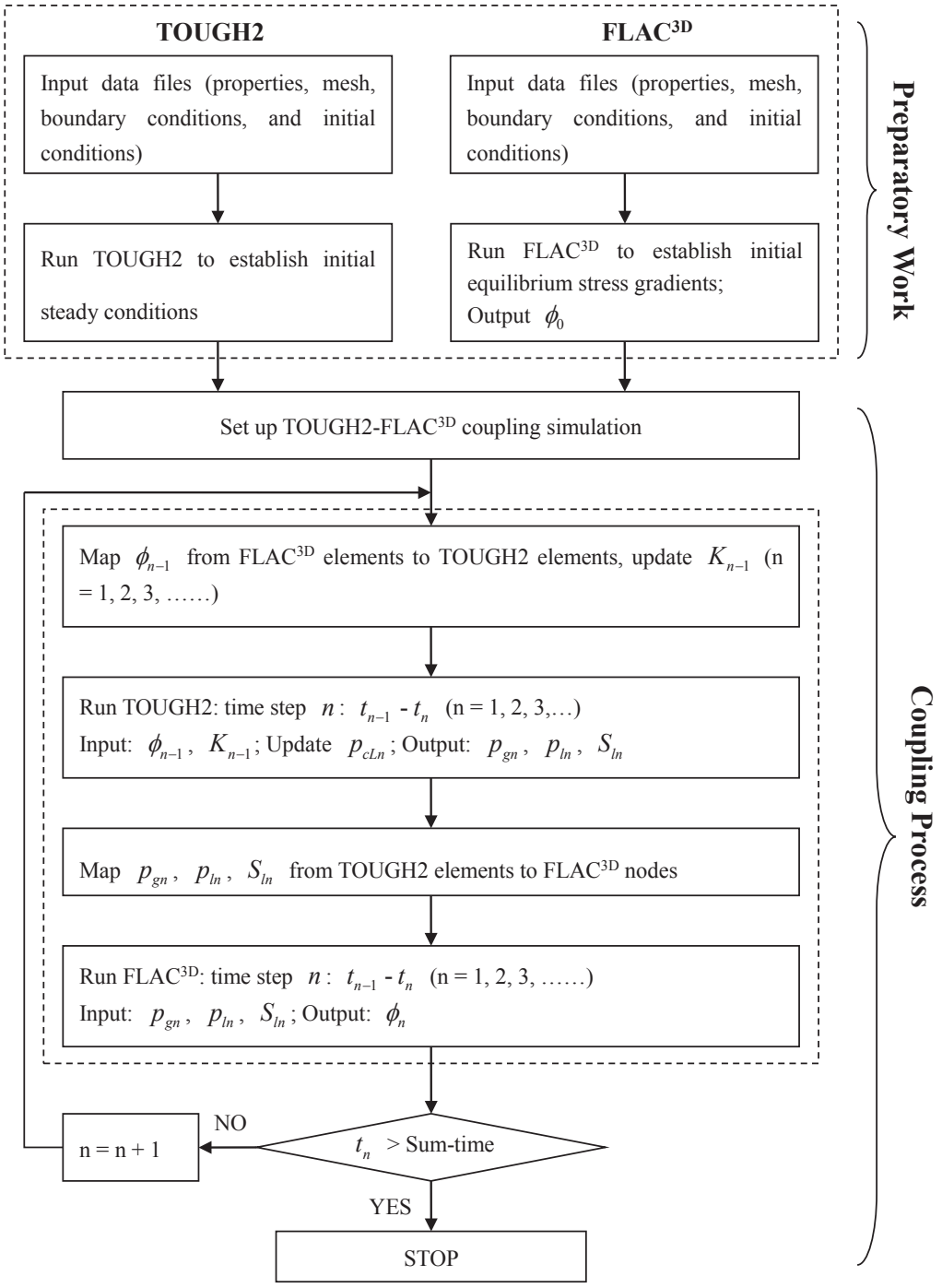

Figure 1. Flow chart for a loosely coupled algorithm.

compressed air was introduced 18.0–21.0 m below the ground surface, and only the first applied pressure level Δp = 160 kPa over 27 h was considered for simplicity. The rate of air injection was monitored by a flow meter during the experiment. Several piezometers were installed near the borehole to measure the variation of the pore pressure at different depths and distances from the borehole. The land uplift was measured by geodetic leveling installed at different distances from the borehole.

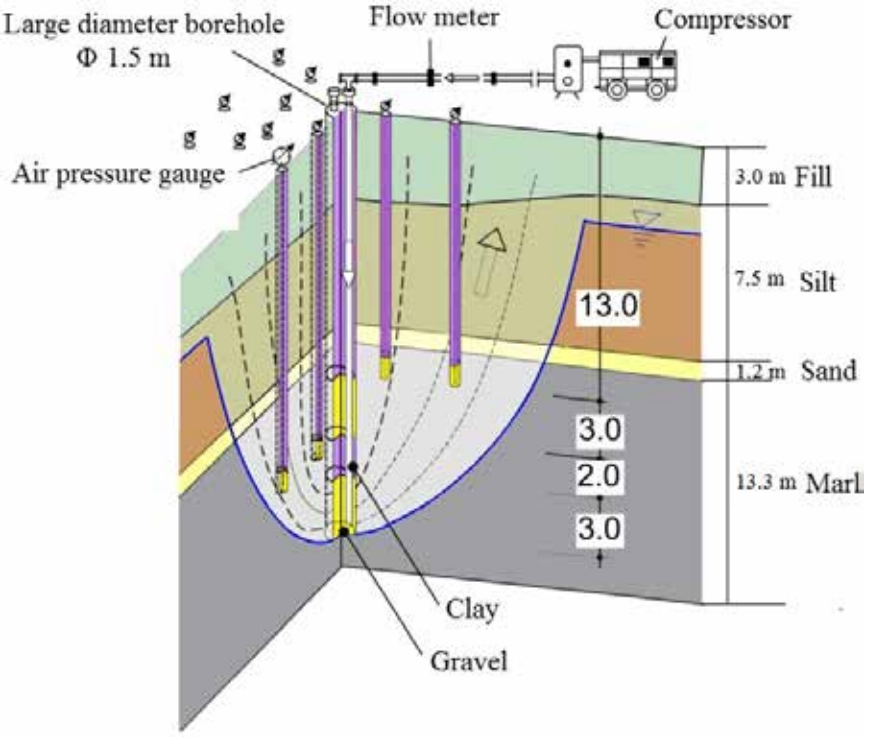

Figure 2. In-situ, air-flow test in Essen (after Kramer and Semprich [1]).

3.2 Setting up of the Numerical Model

3.2.1 Model Domain and Soil Parameters

In this study, the numerical model of the in-situ, air-flow test was established using the above coupling algorithm. Taking advantage of the axial symmetry of this problem, only one-fourth of the domain was simulated. The measured results show that the land uplift reached only 2 mm at approximately 20 m distance from the borehole. The extent of the model was just 40 m in the horizontal direction in the simulation by Öttl [25] and 100 m by Chinkulkijniwat et al. [2]. Therefore, the model domain was 100 m long in both the transverse direction (X) and the longitudinal direction (Y), and was 25 m deep in the vertical direction (Z). The mesh generation in TOUGH2 was the same as in FLAC^{3D}, consisting of 18,259 hexahedron elements and 20,480 nodes, and is shown in Fig. 3. The domain in the vertical direction was discretized to take into account the soil layers, the groundwater table and the air-injection region. The mesh size in the horizontal directions was relatively fine near the borehole and expanded with the distance from the borehole.

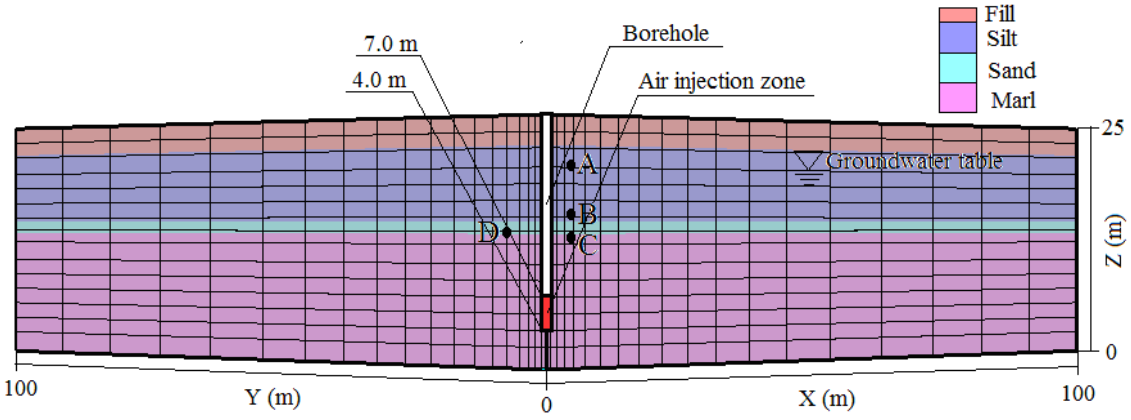

Figure 3. Meshes in the model of TOUGH2 and FLAC^{3D}.

In the numerical simulation, the capillary pressure and the relative liquid and gas permeability dependent on the liquid saturation were described by the van Genuchten model [26] and the van Genuchten-Mualem model [26-27], respectively. The expressions of these two models are described in Eq. (7), Eq. (8) and Eq. (9)

$$p_c = -p_0\left[(S^*)^{-1/\lambda} - 1\right]^{1-\lambda} \qquad (-p_{\max} \le p_c \le 0) \qquad (7)$$

where p_0 is the air entry pressure, λ is a model parameter associated with the degree of soil uniformity, S^* is the effective liquid saturation, $S^* = (S_l - S_{lr}) / (S_{ls} - S_{lr})$, S_l is the liquid saturation, S_{lr} is the residual liquid saturation, and S_{ls} is the saturated liquid saturation.

$$k_{rl} = \begin{cases} S^*\left[1-\left(1-\left(S^*\right)^{1/\lambda}\right)^{\lambda}\right]^2 & (S_l < S_{ls}) \\ 1 & (S_l \ge S_{ls}) \end{cases} \qquad (8)$$

$$k_{rg} = \begin{cases} 1-k_{rl} & (S_{gr} = 0) \\ (1-\hat{S})^2(1-\hat{S}^2) & (S_{gr} > 0) \end{cases} \qquad (9)$$

where $\hat{S} = (S_l - S_{lr}) / (1 - S_{lr} - S_{gr})$ and S_{gr} is the residual gas saturation.

The hydraulic and geo-mechanical parameters for four soil layers in Essen, taken from Ottl [25], are shown in Table 1, including the solid density ρ_s, Young's modulus E, Poisson's ratio v, the initial porosity ϕ_0, the initial intrinsic permeability K_0, p_0, S_{lr}, S_{ls} and λ. Notice that the lower part of the silt layer is characterized by a weaker stiffness. Additionally, due to the rather small deformation occurring in the soil (a maximum value of the measured heave is approximately 4 mm) in the field test, linear elastic behavior was assumed for the whole domain. This assumption of linear elastic behavior has also been used in other simulations of the airflow test in Essen [2, 25]. All the processes involved in the numerical simulation were assumed to occur isothermally at 10°C.

3.2.2 Boundary and Initial Conditions

In TOUGH2, the primary variables are P_β (the pressure of the β phase (the liquid phase (l) or gas phase (g))); X^a_β (the air-mass fraction in the β phase); and T (temperature) for single-phase conditions and P_g, S_g+10 (the gas saturation plus 10) and T for two-phase conditions. The atmospheric boundary conditions, $P_g = p_{atm}$ (where p_{atm} is the atmospheric pressure and was equal to 1.013×10^5 pa), $X^a_\beta = 0.999$, and T = 10°C, were applied at the ground surface. The Dirichlet boundary conditions, $P_l = p_{atm} + \rho_w g(20.25 - Z)$, $X^a_l = 1.0\times10^{-10}$, and T = 10°C, were applied at the bottom of the domain, where the water density ρ_w was 1000 kg/m^3, the gravitational acceleration g was 9.81 m/s^2, and Z was the elevation of the model domain. No flow boundaries were considered at the lateral boundaries. The initial steady condition was obtained by running TOUGH2 with the above boundary conditions and the initial liquid-saturated condition for a sufficient simulation time until reaching a steady state.

In FLAC^{3D}, the domain surface was specified as a free deformed boundary, whereas no deformation at the bottom of the domain was allowed, i.e., $u_h = 0$ and $u_v = 0$, where u_h is the horizontal displacement and u_v is the vertical displacement. The roller displacement boundary ($u_h = 0$) was prescribed at all the lateral boundaries. Under gravitational loads, the initial steady conditions in TOUGH2 were sent to FLAC^{3D} to calculate the equilibrium stress distribution that was used as the initial conditions for the FLAC^{3D} model. This calculation was the first coupling of the TOUGH2 model with the FLAC^{3D} model.

Then, using the steady conditions of the TOUGH2 model and FLAC^{3D} model as the initial conditions, the material properties of the elements within the injection zone were set as freely movable, and the volume and primary variables of these elements were changed to be infinite and $P_g = p_{atm} + \Delta p$, $X^a_\beta = 0.999$, T = 10°C. Because the borehole above the injection zone was impervious in the test, the elements within the borehole were removed in

Table 1. Hydraulic and geo-mechanical parameters for four soil layers in Essen (the values of E and v between parentheses refer to the lower point of the silty layer).

Soil Texture	ρ_s, (g/cm^3)	E (Mpa)	v	ϕ_0	ϕ_0 (kN/m^2)	S_{ls}	S_{lr}	λ	K_0 (10^{-12} m^2)
Fill	2.72	20	0.33	0.36	4.0	0.2	1.0	0.8	4.95
Silt	2.90	12.47	0.35	0.42	30.0	0.2	1.0	0.5	0.495
		(9.24)	(0.37)						
Sand	2.72	21.22	0.32	0.36	4.0	0.05	1.0	0.65	9.90
Marl	2.79	14.33	0.40	0.33	12.0	0.15	1.0	0.6	2.48

the simulations. Then, the coupled hydraulic-mechanical process, considering the interactions between the liquid, gas and solid phases, was repeated until the injection duration of 27 h was reached. Hereafter, the material property and the volume of the elements within the injection zone were reset as the property of the marl and their actual volume, respectively, in order to investigate the variations of multiphase flow and soil deformation after the air injection stopped. The post-injection phase lasted for 100 hours. Notably, the experimental data were not recorded after the air injection stopped in the in-situ, air-flow test.

3.3 Analysis of the Experimental and Simulated Results

3.3.1 Analysis of the Discrepancy between the Simulated and Measured Results

The main objective of this field test is to investigate the magnitude and scope of the land uplift as well as the air loss rate induced by compressed air injection. Fig. 4a shows the distribution of the simulated and measured land uplift at different times. After 27 hours, the simulated land uplift was much higher than the measured value at a distance from the borehole, which might be because the high permeability of the sand layer promoted radial propagation of the overpressure in the numerical simulation. Actually, according to Kramer and Semprich [1] and Ottl [25], the thin sand layer contains a considerable portion of silt in the field, reducing the permeability of the sand layer. Additionally, average values of the permeability for the marl layer were used in the above simulation, although the marl corresponds to silt containing high portions of sand and clay according to Kramer and Semprich [1]. Therefore, the possibility of high anisotropy between the horizontal and vertical soil permeability should be recognized. Fig. 4b compares the behavior over time of the measured and simulated air-injection rates during the test. The mass flux of air (unit: kg/s) injected into the soil interior through the injection zone was calculated using the numerical model and the air density under the normal conditions of atmospheric pressure and 10°C was determined by the ideal gas law, which permitted a calculation of the volume flux of air (m^3/min) injected into the soil. The simulated rate was substantially the same as the measured results during the middle period, whereas there were large differences between them at the initial and final stages. In the field test, the applied air pressure was increased stepwise to 160 kPa by the compressor, as shown in Fig. 5. Before the air pressure reached 160 kPa, the matric suction in the marl layer could not surpass the air entry value of the marl, and no air penetrated into the soil. However, the applied air pressure was set

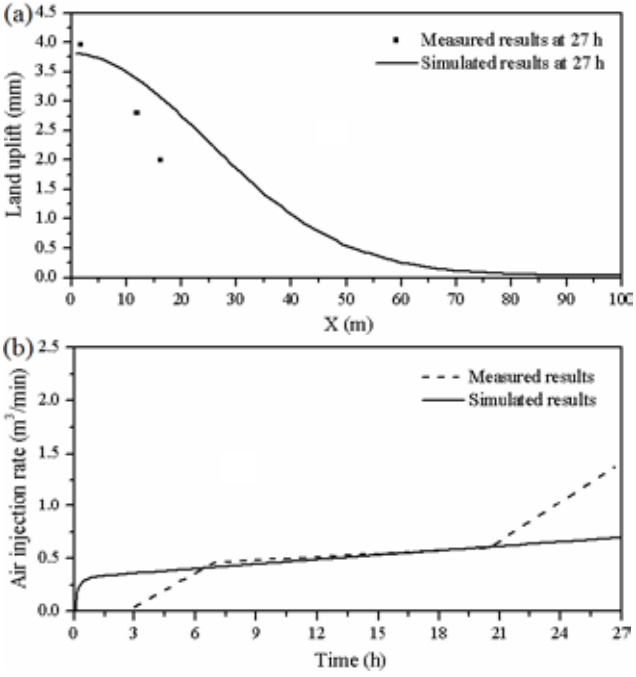

Figure 4. (a) Measured and simulated land uplift at different times and (b) temporal evolution of the simulated and measured air-injection rate during compressed air injection.

to 160 kPa at the beginning of the numerical simulation, so the difference between the measured and simulated results was introduced at the initial stage.

Considering the low permeability of the sand layer, the anisotropy between the horizontal and vertical soil permeability of the marl layer, and the implementation process of the applied air pressure, the values of permeability in the sand and marl layer in the numerical simulations were adjusted as follows: $K_x = K_y = K_z = 0.9\times10^{-12}$ m^2 for the sand layer and $K_x = K_y = 5.58\times10^{-12}$ m^2, $K_z = 3.38\times10^{-12}$ m^2 for the marl layer, and the applied pressure

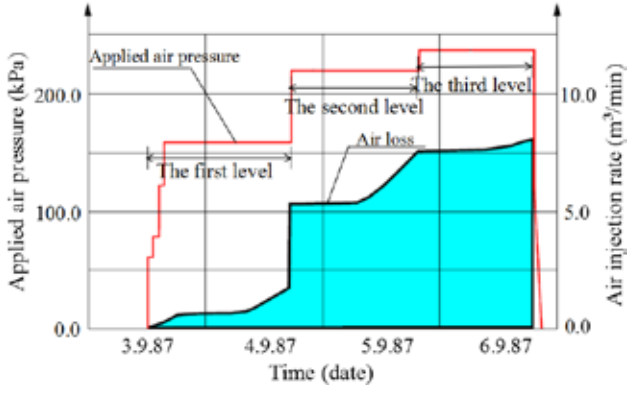

Figure 5. Applied air pressure and air loss versus time for test 1B (after Ottl [25]).

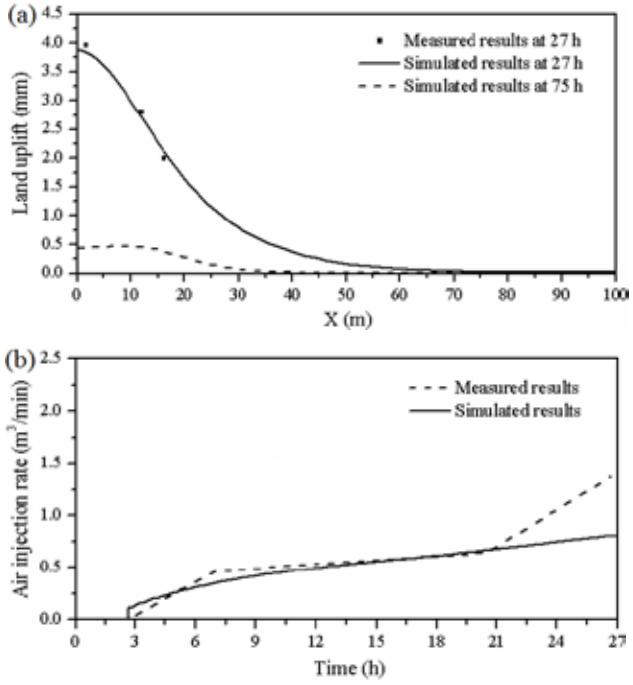

Figure 6. Measured and adjusted simulated land uplift at different times and (b) temporal evolution of the measured and adjusted simulated air-injection rate during compressed air injection.

Δp in the numerical simulations was set as shown in Fig. 5, as follows: Δp = 61 kPa from 0 s to 3360 s, Δp = 78 kPa from 3360 s to 6720 s, Δp = 119 kPa from 6720 s to 10,080 s and Δp = 160 kPa from 10,080 s to 27 hours. The comparison of the adjusted simulated results and the measured results is shown in Fig. 6. There was good agreement between the adjusted simulated and measured land uplift after 27 hours (Fig. 6a). As shown in Fig. 6b, before the air pressure reached 160 kPa (the first 2.8 hours), both the simulated and measured injection rate remained zero. Hereafter, there was a slight discrepancy between the simulated and measured results from 2.8 h to 13 h, whereas they were substantially consistent from 13 h to 21 h. After 21 h, because the air flowed to the location where fractures can be present, the measured rate increased significantly. However, the medium in the numerical model was assumed to be porous media, thereby causing the difference between the simulated and measured rates. In general, the adjusted simulated results agreed well with the measured values, and the adjusted scheme was applied in the following simulation analysis.

3.3.2 Analysis of Seepage and Soil Deformation

Fig. 7a shows the distribution of the simulated gas saturation and airflow after 27 hours. It was expected that the injecting air would permeate into soils due to the pressure gradient and the adjacent regions became unsaturated. Moreover, because the applied air pressure was slightly greater than the maximum groundwater pressure within the air-injection regions, a small area below the injection regions also became unsaturated. The unsaturated zone was concentrated mainly above the air-injection regions. Close to the ground surface, the gas saturation near the borehole decreased because the airflow pushing caused the water to flow upwards. Fig. 7b shows the distribution of gas saturation and air flow after 75 hours (48 hours after compressed air injection stopped). As shown, after the compressed-air injection stopped, the air still flowed upwards and laterally due to the density difference and the pressure gradient, but the magnitude of the air velocity was much smaller at 75 hours than it was at 27 hours. The zone from the bottom to 10 m recovered water saturated because the air in the voids of the injection regions was displaced by the adjacent groundwater, whereas due to the continuous upward airflow, the size of the unsaturated zone from 10 m to 15 m remained substantially unchanged, and from 15 m to the water table, the unsaturated zone expanded into the shallow unsaturated zone.

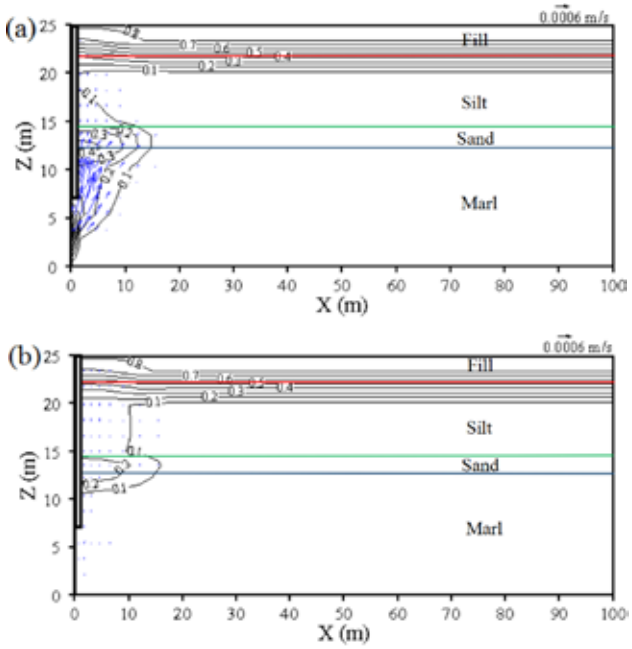

Figure 7. Distribution of simulated gas saturation and airflow at (a) 27 h and (b) 75 h (The blue arrows refer to the magnitude and direction of airflow velocity).

Fig. 8 shows the distribution of the simulated average pore-pressure equivalence at different times. After 27 hours, the average pore pressure near and above the injection zone increased significantly, and the

amplification decreased with the distance from the borehole. The affected zone extended to approximately 70 m horizontally. After 75 hours, due to the airflow dissipation, the average pore pressure near and above the injection zone decreased substantially. From the bottom to approximately 7 m, the average pore pressure recovered to its initial steady value. From 7 m to 16 m, the average pore pressure also decreased to its initial values near the borehole, while it still deviated from the initial values at a distance from the borehole. The reason might be that the gas saturation in this region reached a relatively large value within 10 m horizontally (Fig. 7b), so that it was easy for the airflow to move, but the overpressure and airflow 10 m away dissipated with relative difficulty due to its small gas saturation. Above the elevation of 16 m, the average pore pressure did not decrease to its initial value due to airflow pushing (Fig. 7b). The measured and simulated pore air pressure at the four observed points of A, B, C and D (Fig. 3) are shown in Table 2, and the measured and simulated results were substantially consistent.

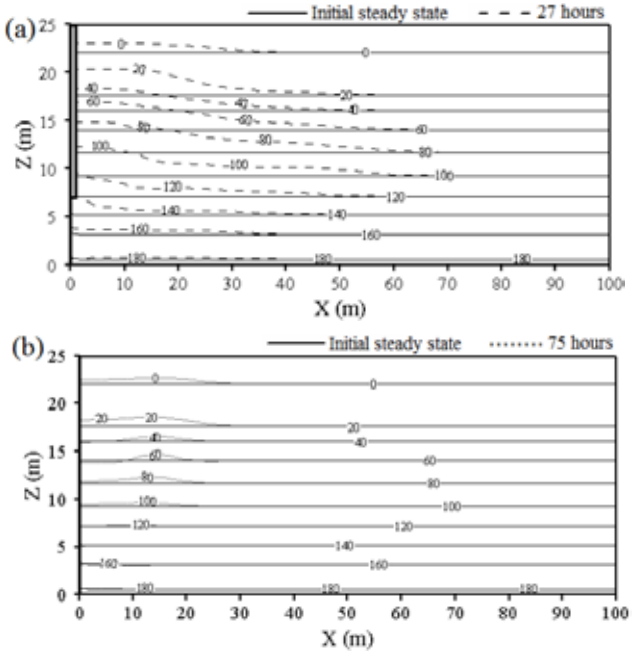

Figure 8. Distribution of simulated average pore pressure at different times at (a) initiation and at 27 h and (b) initiation and at 75 h (unit: kPa).

Table 2. Locations with the measured and simulated pore air pressure for four observation points.

Observation points	A	B	C	D
Horizontal distance from borehole (m)	2	2	2	6
Depth below ground surface (m)	6	10	13	12.5
Measured pore water pressure (kPa)	27	70	95	90
Simulated pore water pressure (kPa)	30.5	76.5	101	95

Fig. 9 shows the distribution of the simulated vertical effective stress at different times. After 27 hours, since the total stress acting on the soil layers remained almost unchanged (the mass of the injected compressed air was very small relative to the weight of the whole soil layers) and the stress overtaken by the fluids in the soil voids increased (Fig. 8), the stress overtaken by the solid skeleton decreased; i.e., the effective stress near and above the injection zones decreased. This release of the vertical effective stress caused an expansion of the soil skeleton in the corresponding zone. The magnitude of the porosity near and above the injection zones therefore increased, and the affected zone of the porosity increment reached approximately 32 m horizontally (Fig. 10a). After 75 hours, the vertical effective stress decreased to its initial values in most areas, while it still appeared to deviate from 12 m to 20 m vertically. Therefore, both the magnitude and scope of the porosity increments also decreased at 75 hours (Fig. 10b), and the maximum value appeared from 10 m to 20 m horizontally due to the distribution of the average pore pressure and vertical effective stress (Figs. 8b and 9).

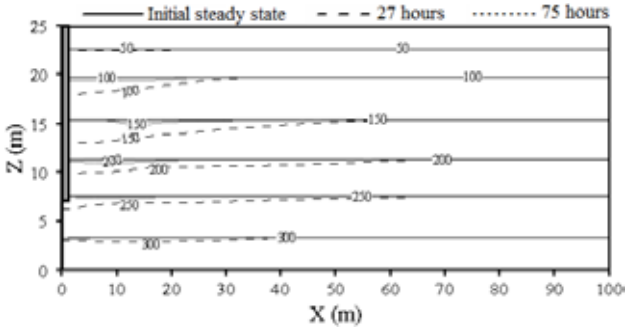

Figure 9. Distribution of simulated vertical effective stress at different times (unit: kPa).

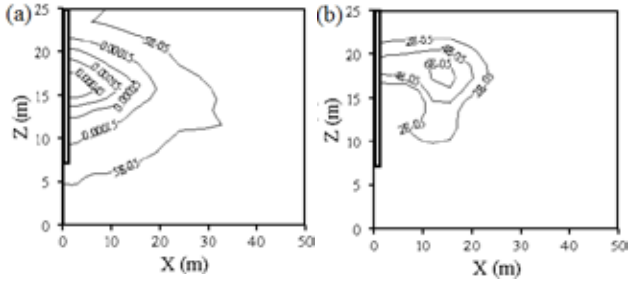

Figure 10. Distribution of the simulated porosity increment at (a) 27 h and (b) 75 h.

Because the porosity near the ground surface changed little, the land uplift was caused primarily by the expansion of deep deformed soils. As shown in Fig. 6a, after 27 hours, the maximum land uplift occurred near the borehole. The land uplift decreased with the distance from the borehole, consistent with the distribution of

the porosity increment within the soil. After 75 hours, the land uplift decreased due to overpressure dissipation and the flat segment within approximately 15 m from the borehole was relevant to the distribution of the porosity increment at 75 h. Fig. 11 shows the behavior over time of the maximum land uplift. During compressed air injection, the land uplift remained zero before 2.8 hours due to no air penetrating into the soil. Later, it increased rapidly and reached a maximum value at 27 hours. After the injection stop, the heave decreased rapidly at first and then gradually went to zero at approximately 110 hours.

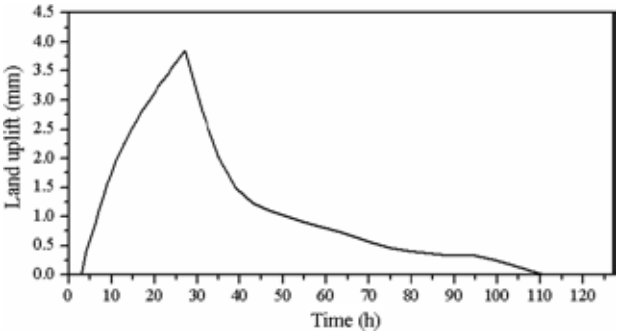

Figure 11. Time behavior of the maximum land uplift.

4. ANALYSIS OF THE IMPACTS OF DIFFERENT FACTORS

4.1 Rain Events

To investigate the effects of a rain event on multiphase flow and land uplift during and after compressed-air injection, rain with intensity equal to 5 mm/h and 20 mm/h was combined with the compressed-air injection. Notably, the duration of rainfall coincided with that of the applied pressure of 160 kPa (i.e., 2.8–27 hours). The model source term in kg/s for rainfall is computed as $m(t) = r_w A_e Q_r(t)$, where t (s) is the time; A_e (m^2) is the effective area for rainwater infiltration and is equal to the area perpendicular to the direction of rainfall; and Q_r (m/s) is the rainfall intensity. The term was applied to the whole soil surface (i.e., the soil elements adjacent to the atmospheric boundary). As the compressed air injection and rainfall stopped, the source term was removed. The whole simulation time, the initial conditions and the other boundary conditions were the same as the base case.

Fig. 12 shows the total stress distribution for different profiles at 27 h for the three cases. The total stress for different profiles after 27 h for the three cases was essentially consistent with that at the initial steady state, indicating that the applied rainwater amount has

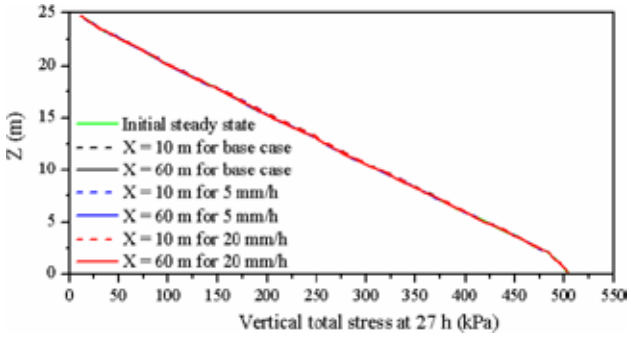

Figure 12. Distribution of total stress for different profiles at 27 h for the base case and rain intensities of 5 mm/h and 20 mm/h.

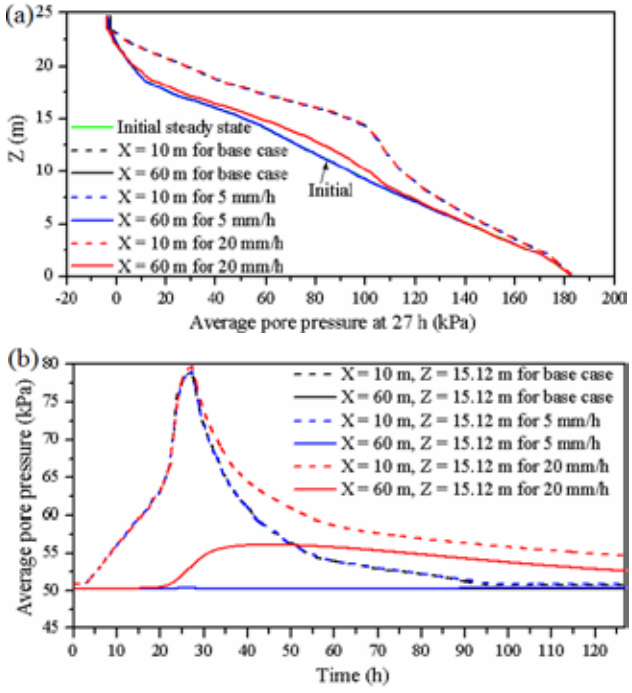

Figure 13. (a) Distribution of the average pore pressure for different profiles at 27 h and (b) the temporal evolution of the average pore pressure at different points for the base case and rain intensities of 5 mm/h and 20 mm/h.

little effect on the total stress. The intensive rainfall produced a continued downward wetting front, which reduced the escape of pore air and compressed pore air between the wetting front and the capillary fringe. As a result, the pore pressure in the unsaturated and saturated zones increased due to airflow pushing by the advancing wetting front. However, a small amount of rainfall cannot completely seal off the ground surface, and pore air could partially escape out of the surface during rainfall and it cannot be compressed and pressurized by the moving wetting front. As shown in Fig. 13a, the average pore pressure distribution for X = 10 m

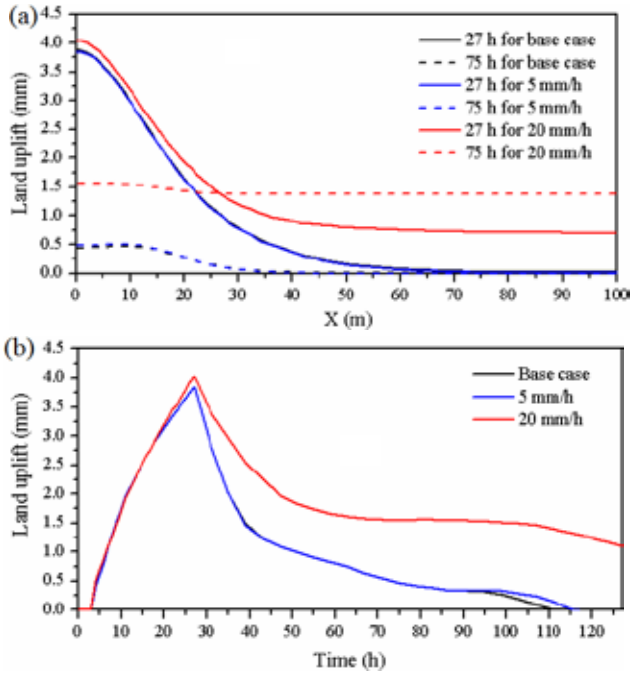

Figure 14. (a) Land uplift at different times and (b) changes in the maximum land uplift with time for the base case and rain intensity of 5 mm/h and 20 mm/h.

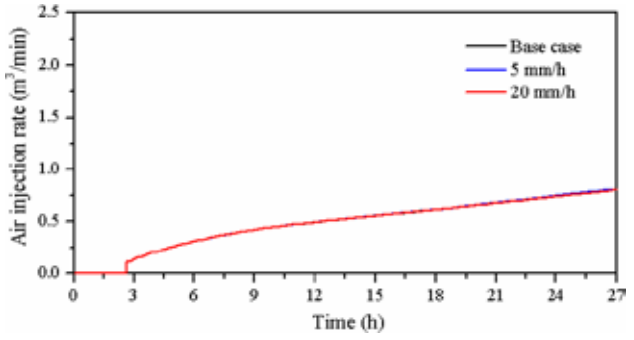

Figure 15. Temporal evolution of the air-injection rate for the base case and rain intensities of 5 mm/h and 20 mm/h during compressed-air injection.

at 27 h seemed to be mostly identical for the three cases, and all deviated from their initial values. The average pore pressure distributions for X = 60 m remained at their initial values for the base case and rain intensity of 5 mm/h, but they deviated from the initial state vertically from approximately 8 m to 20 m for a rain intensity of 20 mm/h. Likewise, as seen in Fig. 13b, the time evolution of the average pore pressure at points ((X = 10 m, Z = 15.12 m) and (X = 60 m, Z = 15.12 m)) was also almost identical for the base case and 5 mm/h, while it began to deviate from the variation of the above two cases at different times for 20 mm/h. Moreover, the magnitude of this deviation was smaller for X = 10 m than for X = 60 m (notably, the seemingly identical pore pressure for X = 10 m at 27 h for three cases in Fig. 13a was limited by the adopted coordinate range). As a result, the distribution of land uplift at 27 h for 5 mm/h was substantially the same as the base case, while the magnitude of the land uplift for 20 mm/h was slightly greater near the borehole, but was much greater at a distance from the borehole than that for the other cases (Fig. 14a). This phenomenon suggested that a low rain intensity (i.e., 5 mm/h in this case) hardly affected the land uplift induced by compressed-air injection, but a high rain intensity (i.e., 20 mm/h in this case) would elevate this land uplift to different levels at different positions. Additionally, as shown in Fig. 14b, it was expected that the maximum land uplift for 5 mm/h was almost consistent with the base case, except that the time required for the 5 mm/h uplift to reach zero was slightly delayed. However, the land uplift for a rain intensity of 20 mm/h began to deviate from the base-case solution at 23 hours, consistent with the variation of the pore pressure (Fig. 13b), probably because the increasing pore pressure induced by intensive rainfall needed some time. Hereafter, the land uplift for 20 mm/h decreased gradually, but its value did not reach zero at the end of the simulation period due to the increasing pore pressure.

Fig. 15 shows the time evolution of the air-injection rate for the base case, rain intensity of 5 mm/h, and 20 mm/h during compressed-air injection. The behavior of the air-injection rate was almost the same for the three cases, probably because the changes in pore pressure near the injection zone were essentially identical for the three cases (Fig. 13a).

4.2 Permeability of Injected Strata

The permeability of the injection zone reflects the ability of soils to conduct water and air, and it plays an important role in the permeation of compressed air into the soil. Different values were considered for the intrinsic permeability of the marl layer (i.e., the injected strata), 0.5 K_{base} , K_{base} and 1.5 K_{base} , to analyze its effects on the multiphase flow and land lift during and after compressed air injection. Notably, K_{base} represented the adjusted intrinsic permeability of the marl layer in three directions (X, Y and Z). All the other simulation conditions were the same as those for the base case.

A large permeability promoted the injected air to flow into the soil voids and affected the seepage and soil deformation in the aquifer. Therefore, as shown in Fig. 16a, with a large permeability, the land uplift increased

at 27 hours. However, at 75 h, the land uplift near the borehole was substantially the same with a different permeability, probably because the unsaturated zone in this region was connected to the shallow unsaturated zones and the dissipation of the overpressure was almost the same. Additionally, the varying rate and the maximum value of the maximum land uplift also increased with increasing permeability during the compressed-air injection. Hereafter, the land uplift with a different permeability decreased gradually to zero, but the time required to reach zero was slightly advanced with a small permeability (Fig. 16b). Similarly, the air-injection rate through the injection section also increased as the permeability of the injected strata increased (Fig. 17).

4.3 Air Entry Pressure of Injected Strata

The air entry pressure denotes the matric suction at which air begins to enter into the maximum pore space of the soils, and it is an important parameter in the soil-water characteristic curve. It is easier for air to permeate soils with a lower air entry pressure (coarse materials). Three different values were considered for the air entry pressure of the injected strata, i.e., 0.5 p_{base} , p_{base} (base case) and 1.5 p_{base} . Notably, p_{base} was the air entry pressure of the marl layer in the base case (Table 1). The other simulation conditions were the same as those for the base case.

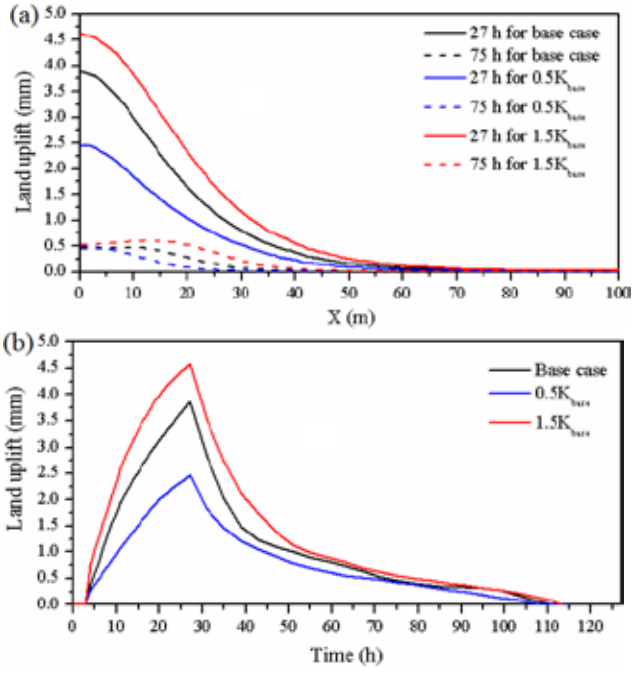

Figure 16. (a) Land uplift at different times and (b) changes in the maximum land uplift with time for different permeabilities.

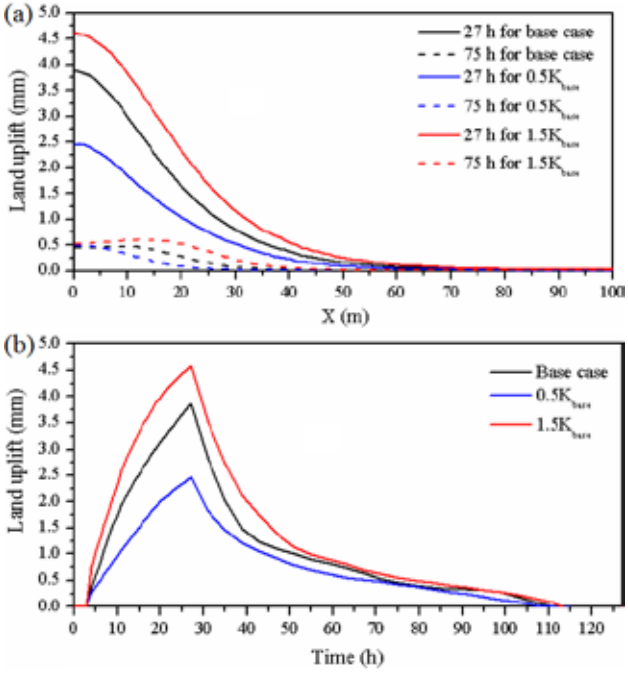

Figure 18. (a) Land uplift at different times and (b) changes in the maximum land uplift with time for different air entry pressures.

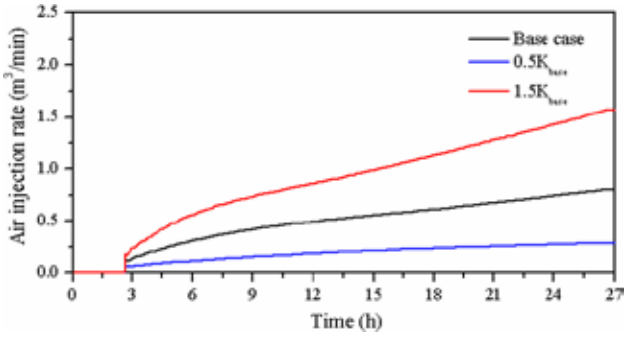

Figure 17. Temporal evolution of the air-injection rate for different permeabilities during compressed air injection.

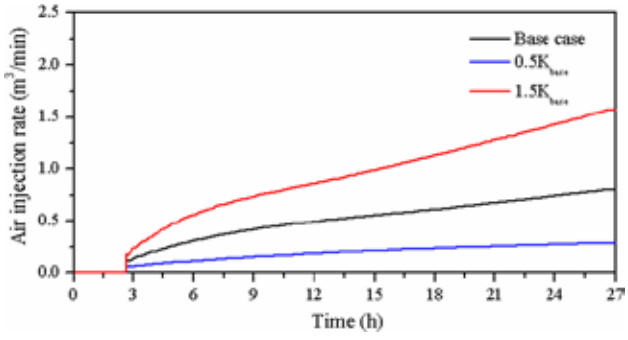

Figure 19. Temporal evolution of the air loss rate for different air entry pressures during compressed-air injection.

As shown in Fig. 18a, with decreasing air entry pressure, the land uplift increased at 27 h, but it varied at different positions at 75 h. Additionally, the varying rate and the maximum value of the maximum land uplift increased with the air entry pressure decreasing during air injection, but the variation of the dissipation of land uplift was similar with different air entry pressures, and the time when the land uplift reached zero was slightly advanced with a high air entry pressure (Fig. 18b). Additionally, the air injection rate increased with decreasing air entry pressure (Fig. 19).

5 SUMMARY AND CONCLUSIONS

In this study, a loosely coupled two-phase flow and geo-mechanical model approach linking two numerical codes, TOUGH2/EOS3 and FLAC^{3D}, was used to investigate the interaction between multiphase flow and soil skeleton deformation underground. Owing the air-flow test in Essen, the effect of different factors on seepage and soil deformation during and after the compressed-air injection was investigated using this coupled model.

As compressed air is injected into the soil layer, the air mainly flows upwards and laterally and the adjacent regions become unsaturated. The average pore pressure and the vertical effective stress near and above the injection zones increases and decreases, respectively, causing the porosity in the corresponding zone to increase. After the termination of the compressed-air injection, both the magnitude and the scope of the porosity increments decrease due to overpressure dissipation. The land uplift, caused primarily by the expansion of the deep layers, reaches the maximum value at the end of the injection phase, and then it decreases to zero after a certain period.

When a rain event, imposed at the ground surface, is combined with air injection underground, the seepage and soil deformation presents a complex response. If the rain intensity is too low to completely seal off the ground surface, the pore air in the unsaturated zones can easily escape out of the ground surface during rainfall, and the land uplift is substantially the same as the base case. However, if the rain intensity is so great that the pore air in unsaturated zones cannot flow easily back to the atmosphere during rainfall and is compressed by the advancing wetting front, the pore pressure in the unsaturated and saturated zones increases, causing the magnitude of the land uplift to increase, but this difference is relatively small near the borehole. Nevertheless, the air-injection rate through the injection section is scarcely affected by a rain event (high or low ran intensity). When the intrinsic permeability increases or the air entry pressure decreases in the injected strata, both the land uplift and the air injection rate through the injection section increase during air injection, but the time required for the land uplift to reach zero is slightly advanced with a small permeability or a high air entry pressure. Therefore, with regard to some scenarios of subsurface fluid injection, a detailed and meticulous strata exploration is required, and the soil properties can significantly affect the multiphase flow and soil deformation during fluid injection. Meanwhile, for different purposes, different strata should be chosen for injecting fluids. Additionally, as a fluid displaces another fluid in porous media, the front is usually perturbed owing to the difference in the physical properties of the fluids, for instance, viscosity, density, surface tension or permeability across the interface of two fluids, thereby causing the development of a fingering phenomenon [28-29]. Therefore, further work needs to be performed to develop a more advanced numerical model to consider the development of fingering during the process of air displacing water.

Acknowledgments

This work was supported by the National Nature Science Foundation of China (Grant NO. 51579170 and 51179118) and the Science Fund for Creative Research Groups of the National Natural Science Foundation of China (Grant No. 51321065).

REFERENCES

[1] Kramer, J., Semprich, S. 1989. E Erfahrungen über Druckluftverbrauch bei der Spritzbetonbauweise (in German). Taschenbuch für den Tunnelbau 13, 91-153.

[2] Chinkulkijniwat, A., Horpibulsuk, S., Semprich, S. 2014. Modeling of Coupled Mechanical–Hydrological Processes in Compressed-Air-Assisted Tunneling in Unconsolidated Sediments. Transport in Porous Media 108, 1, 105-129. DOI: 10.1007/s11242-014-0295-6

[3] Selvadurai, A.P.S. 2006. Gravity-driven advective transport during deep geological disposal of contaminants. Geophysical Research Letters 33, L08408. DOI: 10.1029/2006GL025944

[4] Wong, R.C.K., Lau, J. 2008. Surface heave induced by steam stimulation in oil sand reservoirs. Journal of Canadian Petroleum Technology 47, 01, 13-17. DOI: 10.2118/08-01-13-TN

[5] Teatini, P., Gambolati, G., Ferronato, M., Settari, A.T., Walters, D. 2011. Land uplift due to subsurface fluid injection. Journal of Geodynamics 51, 1, 1-16. DOI: 10.1016/j.jog.2010.06.001

[6] Rutqvist, J. 2012. The geomechanics of CO_2 storage in deep sedimentary formations. Geotechnical and Geological Engineering 30, 3, 525-551. DOI: 10.1007/s10706-011-9491-0

[7] Selvadurai, A.P.S. 2009. Heave of a surficial rock layer due to pressures generated by injected fluids. Geophysical Research Letters 36, 14. DOI: 10.1029/2009GL038187

[8] Rutqvist, J., Vasco, D.W., Myer, L. 2010. Coupled reservoir-geomechanical analysis of CO_2 injection and ground deformations at In Salah, Algeria. International Journal of Greenhouse Gas Control 4, 2, 225-230. DOI: 10.1016/j.ijggc.2009.10.017

[9] Kim, J., Selvadurai, A.P.S. 2015. Ground heave due to line injection sources. Geomechanics for Energy and the Environment 2, 1-14. DOI: 10.1016/j.gete.2015.03.001

[10] Selvadurai, A.P.S., Kim, J. 2015. Ground subsidence due to uniform fluid extraction over a circular region within an aquifer. Advances in Water Resources 78, 50-59. DOI: 10.1016/j.advwatres.2015.01.015

[11] Selvadurai, A.P.S., Kim, J. 2016. Poromechanical behaviour of a surficial geological barrier during fluid injection into an underlying poroelastic storage formation. Proc. R. Soc. A. The Royal Society 472, 2187: 20150418. DOI: 10.1098/rspa.2015.0418

[12] Pruess, K., Oldenburg, C., Moridis, G. 1999. TOUGH2 User's Guide Version 2.0. University of California, Berkeley, USA.

[13] ITASCA Consulting Group Inc. 2002. Fast Lagrangian Analysis of Continua in 3 Dimensions Version 2.10, User's Manual. ITASCA Consulting Group Inc, Minnesota.

[14] Rutqvist, J., Wu, Y.S., Tsang, C.F., Bodvarsson, G. 2002. A modeling approach for analysis of coupled multiphase fluid flow, heat transfer, and deformation in fractured porous rock. International Journal of Rock Mechanics and Mining Sciences 39, 429-442. DOI: 10.1016/S1365-1609(02)00022-9

[15] Rutqvist, J., Tsang, C.F. 2003. TOUGH-FLAC: a numerical simulator for analysis of coupled thermal-hydrologic-mechanical processes in fractured and porous geological media under multi-phase flow conditions. In Proceedings of the TOUGH Symposium 12-14.

[16] Rutqvist, J., Bäckström, A., Chijimatsu, M., Feng, X.T., Pan, P.Z., Hudson, J., Jing, L., Kobayashi, A., Koyama, T., Lee, H.-S., Huang, X.-H., Rinne, M., Shen, B. 2009. A multiple-code simulation study of the long-term EDZ evolution of geological nuclear waste repositories. Environmental geology 57, 6, 1313-1324. DOI: 10.1007/s00254-008-1536-1

[17] Rutqvist, J. 2008. Analysis of injection-induced micro-earthquakes in a geothermal steam reservoir, the Geysers Geothermal Field, California. Lawrence Berkeley National Laboratory.

[18] Rutqvist, J., Moridis, G. J. 2007. Numerical studies on the geomechanical stability of hydrate-bearing sediments. In Offshore Technology Conference. Offshore Technology Conference.

[19] Tsang, C. F., Birkholzer, J., Rutqvist, J. 2008. A comparative review of hydrologic issues involved in geologic storage of CO_2 and injection disposal of liquid waste. Environmental Geology 54, 8, 1723-1737. DOI: 10.1007/s00254-007-0949-6

[20] Cappa, F., Rutqvist, J., Yamamoto, K. 2009. Modeling crustal deformation and rupture processes related to upwelling of deep CO_2-rich fluids during the 1965-1967 Matsushiro earthquake swarm in Japan. Journal of Geophysical Research: Solid Earth 114, B10. DOI: 10.1029/2009JB006398

[21] Bear, J., Bachmat, Y. 1990. Introduction to Modeling of Transport Phenomena in Porous Media (Vol. 4). Springer Science & Business Media.

[22] Chapuis, R.P., Aubertin, M. 2003. On the use of the Kozeny Carman equation to predict the hydraulic conductivity of soils. Canadian Geotechnical Journal 40, 3, 616-628. DOI: 10.1139/T03-013

[23] Taylor, D.W. 1948. Fundamentals of soil mechanics. John Wiley & Sons, New York.

[24] Leverett, M.C. 1941. Capillary behavior in porous solids. Transactions of the AIME 142, 152-168. DOI: 10.2118/941152-G

[25] Öttl, G. 2003. A Three-phase FE-model for Dewatering of Soils by Means of Compressed Air. Universität Innsbruck AI: Publik.-Bereich.

[26] Van Genuchten, M.T. 1980. A closed-form equation for predicting the hydraulic conductivity of unsaturated soils, Soil science society of America journal 44, 892-898. DOI: 10.2136/sssaj1980.03615995004400050002x

[27] Mualem, Y. 1976. A new model for predicting the hydraulic conductivity of unsaturated porous media. Water resources research 12, 513-522. DOI: 10.1029/WR012i003p00513

[28] Homsy, G. M. 1987. Viscous fingering in porous media. Annual review of fluid mechanics 19, 1, 271-311. DOI: 10.1146/annurev.fl.19.010187.001415

[29] Moortgat, J. 2016. Viscous and gravitational fingering in multiphase compositional and compressible flow. Advances in Water Resources 89, 53-66. DOI: 10.1016/j.advwatres.2016.01.002

KRITIČNI ODMIK PLITVEGA TEMELJA NA POBOČJU

Rajesh Prasad Shukla
IIT Roorkee,
Department of Earthquake Engineering
Roorkee, Indija
E-pošta: rpshukla.2013@iitkalumni.org

Ravi Sankar Jakka *(vodilni avtor)*
IIT Roorkee,
Department of Earthquake Engineering
Roorkee, Indija
E-pošta: rsjakka@iitr.ac.in

Ključne besede

nosilnost temeljnih tal, nekoherentna zemljina, temeljenje, razdalja odmika, pobočja

Izvleček

Konstrukcije so pogosto zgrajene na pobočjih v hribovitih območjih, kar ima za posledico pomanjkanje podpore tal zaradi nagnjene podlage na pobočni strani temeljenja. To povzroči zmanjšanje nosilnosti temeljenja. Čeprav obstajajo številne študije o temeljenjih na pobočjih, je večina teh študij omejena zgolj na površinsko temeljenje (to je brez upoštevanja globine temeljenja). Poleg tega v literaturi ni soglasja o vplivu razdalje odmika temelja od pobočja na nosilnost temeljnih tal. V prispevku so predstavljeni rezultati analiz s končnimi elementi za pasovne temelje, ki ležijo na stabilnih pobočjih. Analizirano je veliko število možnih nagibov pobočij z različnimi globinami temeljenja. Iz rezultatov je razvidno, da se kritična razdalja odmika poveča s povečanjem notranjega kota trenja zemljine, globine temeljenja in nagiba pobočja. Kritična razdalja odmika je med 2 do 4-kratno širino pasovnega temelja za zemljine z nizkim notranjim kotom trenja, medtem ko je več kot 10-kratna širina pasovnega temelja za zemljine z višjim notranjim kotom trenja. Na podlagi rezultatov študije je razvita tudi regresijska enačba. Predlagana enačba lahko predvidi vpliv različnih parametrov, ki vplivajo na nosilnost temeljev, ki ležijo na pobočjih. Rezultati so primerjani s prejšnjimi eksperimentalnimi in numeričnimi študijami.

CRITICAL SETBACK DISTANCE FOR A FOOTING RESTING ON SLOPES

Rajesh Prasad Shukla
IIT Roorkee,
Department of Earthquake Engineering
Roorkee, India
E-mail: rpshukla.2013@iitkalumni.org

Ravi Sankar Jakka *(corresponding author)*
IIT Roorkee,
Department of Earthquake Engineering
Roorkee, India
E-mail: rsjakka@iitr.ac.in

Keywords

bearing capacity ratio, cohesionless soil, footing, setback distance, slopes

Abstract

Structures are often constructed on slopes in hilly regions, which results in a lack of soil support on the sloping side of the footings. This causes a reduction in the bearing capacity of the footings. Though there are number of studies about foundations on slopes, most of these studies are confined to surface footings only (i.e., without the depth of embedment). Furthermore, there is no consensus in the literature over the influence of the setback distance on bearing capacity. This paper presents the results of finite-element analyses on a strip footing resting on stable slopes. A very large number of possible soil slopes with different footing depths were analysed. From the results it is found that the critical setback distance increases with an increase in the internal friction angle of soil, the depth of the footing and the slope gradient. The critical setback distance is varying between 2 to 4 times the footing width for soils with a low internal friction angle, while it is more than 10 times the footing width for soils with a higher internal friction angle. A regression equation is also developed based on the outcomes of the study. The developed equation is able to predict the influence of various parameters affecting the bearing capacity of a footing resting over the slopes. The results are compared with earlier experimental and numerical studies.

1 INTRODUCTION

Structures are often built on or near a slope for several reasons, such as the unavailability of level ground, to make the structure more appealing, to construct a foundation for bridges, etc. The presence of a slope significantly affects the load-carrying capacity of a footing [1]. A footing constructed on slopes, lacks soil support on one side, which results in the failure of the foundation at a lower load compared to the identical foundations on level ground. This means that the ability of soil to support structures (i.e., bearing capacity) reduces. An estimation of the bearing capacity after accounting for the slope and foundation geometry is difficult. In these cases, the determination of the bearing capacity is different from general cases, as various additional factors influence the bearing capacity.

For foundations located on a slope, the plastic zone on the side of the slope is relatively smaller than those of similar foundations on level ground [2]. Thus, the ultimate bearing capacity of the foundation is correspondingly reducing in almost all cases. The soil strength on the slope side is fully mobilised before the complete mobilization of the soil strength on the side of the level ground, and consequently the footing fails without reaching its ultimate collapse load. The geometry of the

slopes and the soil characteristics are important factors influencing the mobilization of soil strength on either side of the slope. The geometry of the slope includes the setback distance (B'), the slope gradient (horizontal: vertical) and its height. The soil characteristics include the type of soil and the strength parameters of the soil (c and φ).

A number of studies considered the effect of the slope on bearing capacity of the footings. Some of the studies considered the effect of the setback distance on bearing capacity of the footing. Meyerhof [2] proposed bearing-capacity factors for a footing resting near slopes. Hansen [3] presented slope-correction factors for a footing resting precisely on the slope crest. However, the presented solution cannot be used for a footing resting with some distance from the slope crest. Shields et al. [4] experimentally evaluated the resultant bearing-capacity factor, $N_{\gamma q}$, (the combined effect of overburden resistance and soil self-weight), for a footing resting over a slope gradient of 2 Horizontal: 1Vertical (2H:1V) and 1.5H:1V in cohesionless soil. It was reported that Meyerhof [2] overestimates the bearing capacity factors for a footing resting near the slope. This is due to fact that Meyerhof [2]considered equal mobilization of the soil strength on both sides of the slope. Kusakabe et al. [5] used the upper bound to estimate the bearing capacity. Model tests were also conducted, but the maximum setback distance was restricted to the footing width (B). Graham et al. [6] used method of stress characteristics to determine the bearing capacity, but the study was limited to a setback of 2B. Tatsuoka et al. [7] found the study results of Graham et al. [6] to be on the unsafe side. Bowles [8] considered a graphical approach to incorporate the effect of slopes, but the variation in the failure geometry with the slope angles and setback distance are not considered in the analysis. Saran et al. [9] used upper bound analysis and the limit-equilibrium method to determine the ultimate load. The critical setback was evaluated separately for bearing-capacity factors (N_c, N_q, and N_γ). The critical setback distance was found to range from 1.88B to 4.88B. The mechanism adopted in the upper-bound analysis is inconsistent with the assumed soil model as an inadmissible failure mechanism was adopted in the study [10]. Narita and Yamaguchi [11] extended the study of Kusakabe et al. [5] to the clay slope, but both studies neglected the mobilization of the shear strength of the soil on the level side of the footing. De Buhan and Garnier [12] evaluated the bearing capacity of a rectangular shallow foundation located near a slope or an excavation by using yield design theory.

Lee and Manjunath [13] constrained the maximum setback distance to 5B. However, the test results clearly showed that the bearing capacity is increasing continuously, even at 5B. Huang and Kang [14] used the limit-equilibrium method and found that the critical setback distance is varying from 2.1 to 7.1B for the soil of internal friction 30 to 45°, respectively. Castelli and Motta [15] used the limit equilibrium and found that the critical setback is varying from 1.5B to 5.5B. El Sawwaf and Nazir [16] conducted tests on loose sand and found that the enhancement in bearing capacity becomes constant for a setback of 3B. Naeini et al. [17] conducted a study on a slope of 1H: 1V and found that the bearing capacity reaches the level ground at a setback of 10B. Gill et al. [18] observed in the experimental studies that the effect of the slope is significant up to a setback of 3B in coal ash slopes. Nouri [19] found the critical setback distance to be equal to 8B for soil of internal friction 35° and it can be even more than 8B for the soil of higher values of internal friction. Rostami and Ghazavi [20] used the limit-equilibrium method and found that the critical setback distance is varying between 3.1 and 5.4B.

There is no consensus over the critical value of the setback distance in the literature. A few studies concluded that the setback distance does not affect the bearing capacity beyond a B'/B of 2 and 3 [6, 8, 16, 18, 21-24]. However, other studies found this value to vary up to 5 and 6 [2, 4, 9, 13, 14, 25-27]. Some studies found the B'/B values to be even more than 7–8 [14, 17, 19]. The strength contribution from the soil on the level side of a footing, the effect of the slope angle on the failure surface, the effect of driving forces acting on the sloping side and the effect of embedment depth of footing have been neglected in most of the studies. Furthermore, these studies do not incorporate the non-uniformity of the surcharge loading, especially on the slope side of the footing. Another common limitation in most of the studies is that these were restricted up to a setback distance of 5B in the analyses, even though there is a significant improvement in the bearing capacity from a setback of 4B to 5B. This means that the true value of the critical setback distance remains undetermined in the earlier studies.

In the present study extensive finite-element analyses have been carried out to study the effect of the setback distance on the bearing capacity of a footing resting near the slope crest for various possible slopes and footing geometries, including the depth of the embedment. Based on the study, bearing-capacity-reduction factor (BCR) is proposed for a combination of parameters. The BCR factor is defined as the ratio of the bearing capacity of a footing resting on a slope to the bearing capacity of an identical footing resting over level ground. A regression equation is also developed to directly estimate the reduction in the bearing capacity of footings resting over the slope.

2 PARAMETERS CONSIDERED IN THE ANALYSIS

All the different parameters affecting the performance of a strip footing resting near the slopes, such as the soil friction angle, the slope inclination, the depth of the footing and the setback distance were considered in the analysis. The ranges of the parameters used in the study are summarized in Table 1. It is commonly accepted that the angle of internal friction of soil can vary between 27° and 42° [28]. But to maintain the uniformity in the results, the present study considered a range of friction angles varying from 25^0 to 45^0. The slope angle considered in the analysis depends on the friction angle of the soil. To ensure the stability of the soil slope, the slope angle is assumed to be always less than the angle of internal friction of the soil. Additionally, slope-stability analyses were carried out to avoid unstable slopes. Two unit weights, 16 and 17 kN/m^3, are considered in the analysis. The stiffness and the Poisson's ratio of the soil are assumed to be 12500 kN/m^2 and 0.3, respectively. The normalized parameters, depth ratio and setback ratio are defined and used for the interpretation of the results. The depth ratio is defined as the depth of the foundation normalized with respect to the width of the footing, while the setback ratio is the setback distance for a footing normalized with respect to the width of the footing. After considering the variation in the different parameters, a total of 528 cases have been analysed.

3 METHOD OF ANALYSIS

The finite-element analysis was performed using a two-dimensional finite-element program. A plain-strain analysis was used to simulate the strip footing resting near the slope. A software programmeOptumG2 was used for the FEM analysis. Fig. 1 shows a typical finite-element model used in the study. It was assumed that the slope gradient is uniform along the length of the footing.

The model domain was kept large enough to minimize the boundary effects. The area of the domain was selected based on the slope geometry and the setback distance. For a larger slope gradient and setback distance, a larger area of domain was selected to minimize the effect of the boundaries on the results of analysis.

The number of elements in the analysis and the area of the model domain were varied with the slope gradient and the setback distance. Fifteen nodded gauss elements were used in the analysis. The elements use a cubic interpolation of the stresses and the quartic interpolation of the displacements. A small number of elements are sufficient for steep slopes with a smaller setback distance, whereas a larger number of elements are required for gentle slopes with a larger setback distance. The optimum number of elements were worked out by

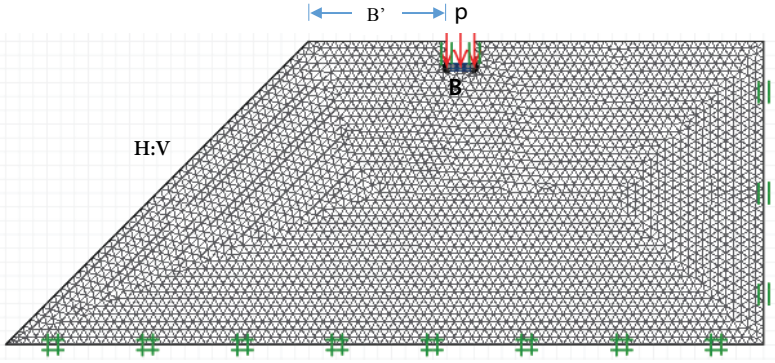

Figure 1. A typical finite-element model used in the study.

Table 1. Ranges of different parameters considered in the analysis.

Friction angle (φ^0)	Slope gradient, G (V/H)	Depth ratio (D/B)	Setback ratio (B'/B)	No. of tests
25	1/10, 1/7, 1/5, 1/4, 1/3	0, 0.5 and 1	0, 1, 3, 5 and 7	75
30	1/10, 1/7, 1/5, 1/4, 1/3 and 1/2	0, 0.5 and 1	0, 1, 3, 5 and 7	90
35	1/10, 1/7, 1/4, 1/3, 1/2 and 1/1.5	0, 0.5 and 1	0, 1, 3, 5,7 and 9	108
40	1/10, 1/7,1/4, 1/3, 1/2, 1/1.5 and 1/1.4	0, 0.5 and 1	0, 1, 3, 5, 7 and 9	108
45	1/10, 1/7, 1/4, 1/3, 1/2, 1/1.5 and 1/1.2	0, 0.5 and 1	0, 1, 3, 5, 7, 9 and 11	147

considering a critical case using the mesh adaptively option of Optum. The mesh adaptivity was earlier used by several studies to refine the mesh to obtain accurate results [30-32]. It was found that 3–4 iterations are enough to obtain consist results. Conservatively, a total of 6 adoptive iterations were considered in the analyses. In the first iteration, the number of elements was fixed to 5000. Finally, a total of 7000 elements were found to be adequate for the analysis. The same number of elements are used for all the cases in the final adoptive iteration. The six-nodded interface is idealized as an element of zero thickness between the soil and the footing. Details of the analysis can be found in Krabbenhoft et al. [29]. Sand was modelled as a drained material, and a Mohr–Coulomb model was used to represent the shear strength. The soil friction angle (φ) was assumed to be constant throughout the soil strata, i.e., the relative density of soil is not varying with the depth. The foundation was considered as a weightless rigid material. The load was applied to the footing in terms of a load multiplier, and was increased to the point of foundation failure.

4 RESULTS AND DISCUSSIONS

The effects of the setback distance on BCR were analysed for various slope inclinations, the depth of footing and the internal friction angles of the soil. The critical setback distance was estimated for various different combinations of these parameters. The effects of these parameters are discussed separately in the following four sections, i.e., the effect of setback distance, the effect of the slope gradient, the effect of the depth ratio and the effect of the friction angle of the soil. The critical setback distance is defined as a minimum distance, where the setback distance does not influence the BCR significantly. Some of the typical results are presented for soil of internal friction 35° only.

4.1 Effect of the setback distance

Though the effect of the setback distance on the BCR is determined for all the cases presented in Table 1, the results here are presented for a soil of internal friction 35°. The typical variation in BCR with the setback distance for a soil of friction angle of 35° is presented in Fig 2. The variation in BCR with the setback distance for depth ratios of 0, 0.5 and 1 are presented in Figs 2 a, b and c, respectively. In all the cases, the BCR is found to be improving with an increase in the setback distance due to an increase in the soil confinement on the slope side of the footing.

The BCR increases with a relatively higher rate up to a setback ratio (B'/B) of 3, and this rate of increase in the BCR reduces for the higher value of the setback distance. It is evident from Fig 2 (a, b and c) that for a particular slope gradient and setback distance, the BCR is reducing with an increase in the foundation depth. The BCR is higher in the case of a gentle slope and the BCR is becoming constant for a small setback distance. The rate of increase in the BCR is higher in the case of a slope with a steep gradient. Increasing the B'/B value more than 5 does not improve the BCR significantly. The curves are relatively steeper in the case of the footing with a higher depth ratio, and it indicates that the rate of increase in the BCR is higher in the case of a footing with a higher depth ratio. The increase in the setback distance reduces the instability caused by the slope. Thus, the improvement in BCR and the confinement of the

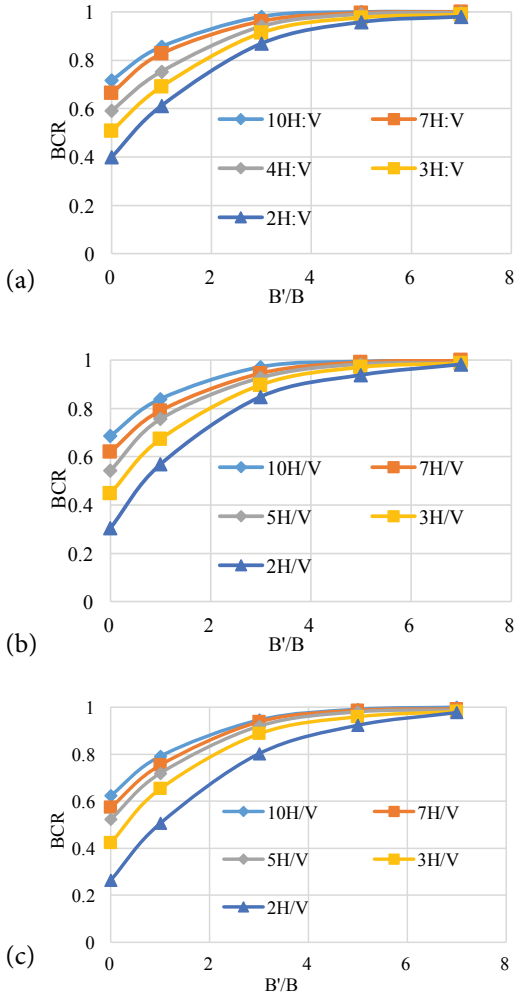

Figure 2. Effect of setback distance on BCR for a footing resting on soil of internal friction 35° for different depth of embedment: (a) D/B=0.0, (b) D/B=0.5 and (c)D/B=1.

soil is observed with larger setback distances for a given slope gradient and an embedment depth of footing.

The BCR improves with the increase in the setback distance due to the lesser effect of the instability caused by the slope. Passive resistance also increases with an increase in the setback distance due to an increase in the amount of surcharge loading and the effective soil weight contributing to the bearing capacity. Mobilization of the soil strength on the level side of the footing is also increasing with an increase in the setback distance, which is the main reason for the higher rate of improvement in the BCR at lower setback distances. The stiffness of the foundation increases with the setback. The increase in the stiffness of the soil foundation system also improves the bearing capacity of soil [33]. The results presented here for a depth of embedment of zero are comparable with earlier studies by Rostami and Ghazavi [20] and Keskin and Laman [26]. However, both studies were confined to surface footings. The testing was limited to a few relative densities, three slope angles and a maximum setback of 5B, which further restricted the authors to determine the true critical setback distance. A detailed comparison of the results with Keskin and Laman [26] is presented later in the section 'Validation of the equation with experimental data and analytical analysis'.

The effect of the setback distance on soil deformation is shown in Fig. 3. Though the analysis is carried out for a large range of soil, the results are presented for the soil of internal friction angle 35°, and slope gradient of 2H: V. The setback distance was varied from 0 to 7B. Fig. 3 (a and b) clearly shows that at a higher setback distance, the strength of the soil on the sloping side contributes to the strength of footing, while no or a partial mobilization of the soil strength is observed for smaller setback distance. This means that the behaviour of the footing at a low setback distance is entirely governed by the soil on the sloping side. Increasing the setback distance more than a certain value enables the contribution of the soil strength from both sides of the footing. The effect of the slope becomes insignificant at a setback distance of 5B. Ausilio [27] also observed that for soil with an internal friction of 35°, the effect of the slope diminished at the setback of 5B for the footing resting on the ground surface. Fig. 3 (f) shows that for a setback distance of more than the critical setback, the behaviour of the footing becomes independent of the slope geometry. At this stage the mobilization of soil strength on both sides of the footing becomes almost equal to each other, as depicted by the symmetrical failure surface on either side of the footing. So the effect of the slope on the footing's performance can be minimized by maintaining a proper distance between the slope edge and the footing. The setback distance at which the behaviour of the foundation becomes independent of the slope depends on the slope angle as well as the soil's internal friction.

4.2 The effect of the slope gradient

The effect of the slope inclination on the BCR is studied for a large range of slope gradients for stable soil slopes. The typical variations of the BCR with the slope gradient for different foundation depths on a soil with an internal friction of 35° are shown in Fig. 4. The graphs are plotted for different amounts of setback distance. The BCR decreases with an increase in the slope gradient, and this decrease in the BCR is depending on the depth of the foundation embedment and the relative location of the footing from the slope crest. The reduction in the BCR with an increase in the slope gradient is very significant when the footing is resting near the slope crest. The effect of the setback distance is becoming more evident with an increase in the slope gradient. Comparing Figs 4 (a, b and c), it is observed that the reduction in the bearing capacity with an increase in the slope gradient is marginally higher for a footing resting at a relatively higher depth.

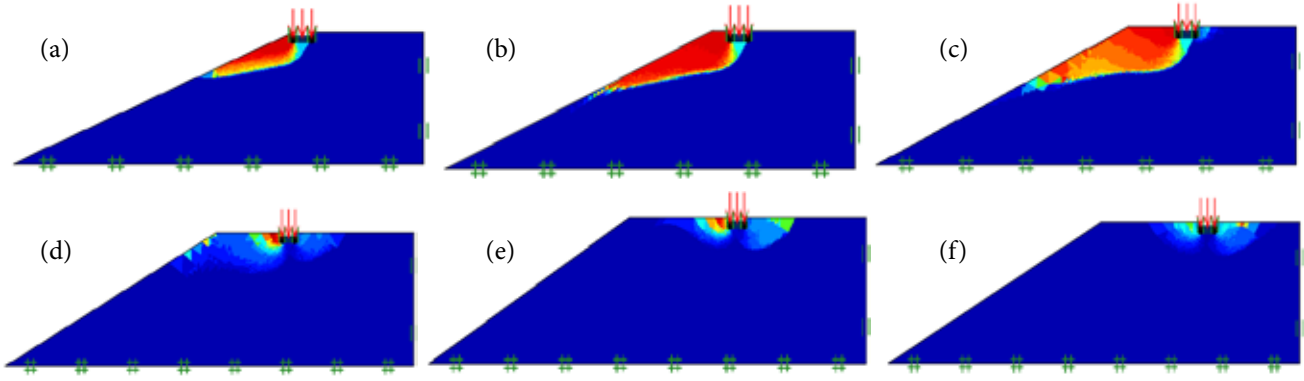

Figure 3. Effect of setback distance on the deformation profile of the soil with internal friction 35°: (a) B'/B=0, (b) B'/B=1, (c) B'/B=3, (d) B'/B=5, (e) B'/B=6, and (f) B'/B=7.

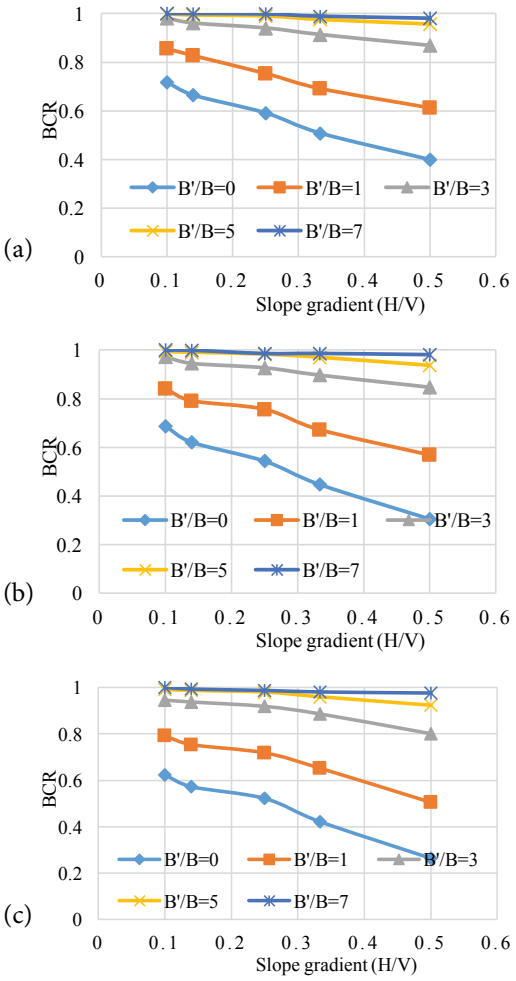

Figure 4. Effect of slope gradient on BCR for a soil of internal friction 35°. (a) D/B=0, (b) D/B=0.5 and (c) D/B=1.0.

In the case of large setback distances, the BCR remains relatively unaffected by a change in the slope gradient.

The effect of the slope gradient on the soil deformation is shown in Fig. 5. The results are presented for a soil of internal friction 35°. The setback distance and the depth ratio of the footing were maintained equal to 3B and 0.5, respectively, and only slope gradient was varied for analysis. The soil deformation further increases with an increase of the slope gradient and the maximum deformation is observed at a steep slope gradient. Figs. 5 (a-d) show that the orientation of the soil movement and failure surface is similar to a normal footing when the slope gradient is relatively very small. It also shows that the soil failure surface and the soil deformation are oriented towards the ground surface at a smaller slope gradient, and both are leaning gradually downward, i.e., towards the slopping surface with an increase in the slope gradient. Similar observations were made in the experimental studies conducted by Chang et al. [34].

4.3 The effect of embedment depth of footing

Fig. 6 shows the effect of the footing embedment depth on the BCR for various slope gradients. The BCR decreases with an increase in the embedment depth of footing, in spite of the increase in bearing capacity. The effect of the footing embedment depth is significant when the footing is resting near the slope crest, and gradually becomes negligible with an increase in the setback distance. This is due to the fact that for a setback distance, more than or equal to the critical setback, the BCR

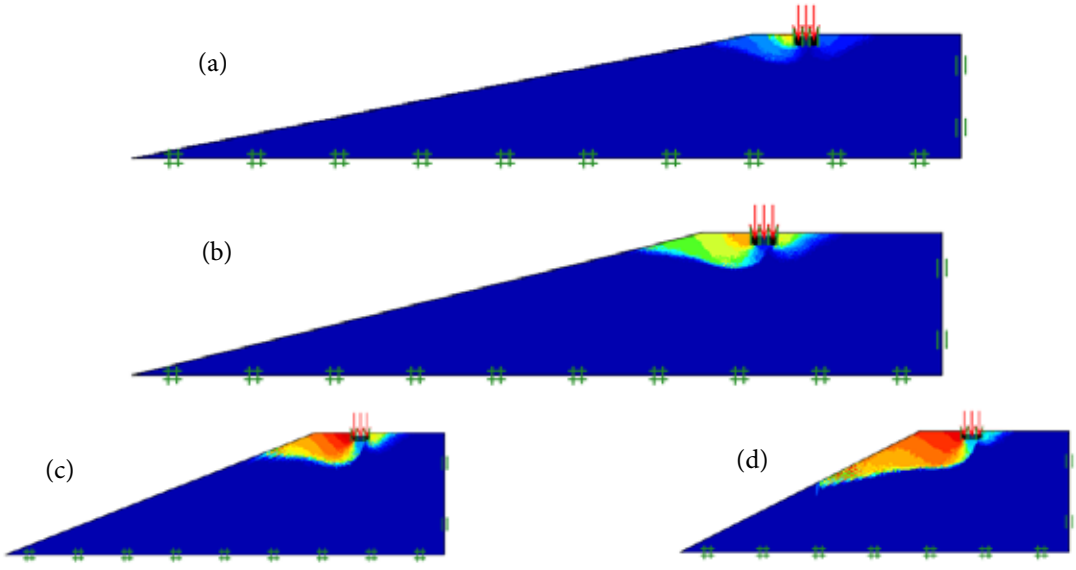

Figure 5. The deformation profile of soil slope for various slope gradients for soil of internal friction 35°: (a) 5H: V (b) 4H: 1V, (c) 3H: V and (d) 2H: V.

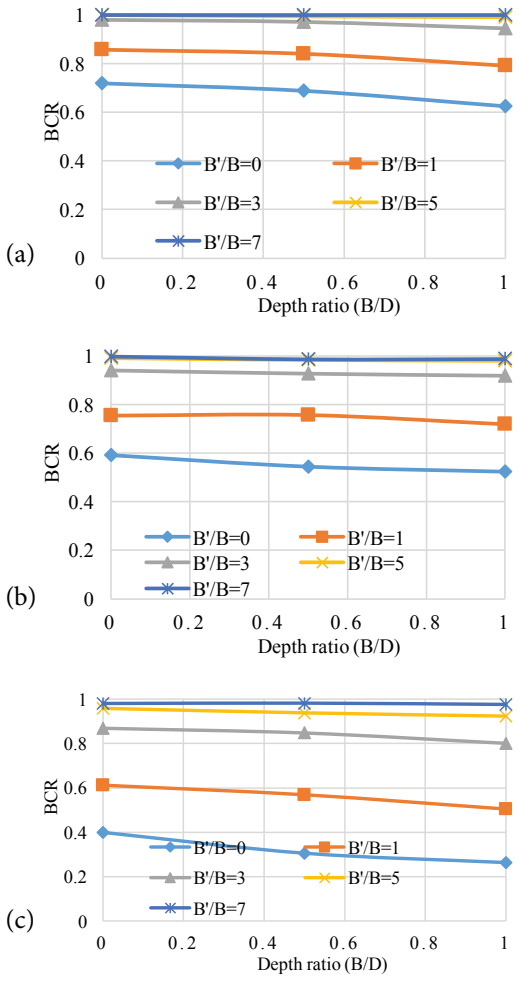

Figure 6. Effect of depth ratio of the footing on the BCR of soil with angle of internal friction 35°. (a) 10H: V, (b) 4H: V, and (c) 2H:1.

remains almost constant, irrespective of the slope inclination. Similar to the present study, Narita and Yamaguchi [11] also found that the effect of the embedment depth of the footing is significant at a low setback distance.

Two observations can be made from Figs. 6 (a, b and c). First, the BCR decreases with an increase in the depth ratio of the footing, especially in the case of a steep slope, and second, for a particular setback distance, the difference in the BCR is becoming more evident with an increase in the depth ratio of the footing. In the case of level ground, the effect of the depth ratio of the footing is relatively more significant for a soil with a low friction angle or loose soil, and a similar observation is also made in the present study for a footing resting over the slope. Castelli and Motta [15] also found that the effect of the depth of the embedment on BCR is not significant; however, the critical setback distance increases with the embedment depth.

Garnier et al. [22] found the coefficient of reduction for a surface footing is always greater than 0.2 in soil with an angle of internal friction 40.5°, even when the slope is steep (3V:2H). A similar observation is also made in the present study for the footings resting over the ground surface. In addition to the surface footing, studies are also extended to a depth ratio of 0.5 and 1. For a soil with an angle of internal friction 40.5°, the coefficient of reduction (BCR) is found to be 0.15 and 0.1, respectively, for depth ratios of 0.5 and 1.0.

4.4 Effect of the angle of internal friction of soil

The effect of the angle of internal friction of soil on the BCR of a footing resting on a different slope gradient is presented in Fig. 7. The results are presented for the surface footing only. For a particular setback distance, the angle of the slope, and the depth of footing, the BCR is decreasing with an increase in the friction of the soil (or relative density). Furthermore, the reduction in the BCR is varying with the angles of shearing resistance of soil, and this variation is depending significantly on the magnitude of the setback distance and slope gradient. The reduction in the BCR with an increase in the friction angle of soil is higher for a small setback distance and a steep slope gradient. The relationship between the BCR and the friction angle of soil is linear for gentle slopes, and it is becoming non-linear with an increase in the slope gradient. In comparison to the soil with a low internal friction angle, the pressure is distributed over a relatively large area in the case of soils with higher friction angle. To mobilize the strength of the soil completely, the footing resting on the dense sand requires a relatively large setback distance. In the loose sands, the failure is either a local shear failure or a punching shear failure, and in both cases the footing sinks without affecting the surrounding area, so these soils need a relatively small setback distance to compensate for the effect of the slope inclination. This reduction in the BCR with an increase in the internal friction angle of soil is increasing with an increase in the slope angle and a decrease in the setback distance. Rostami and Ghazavi [20] observed a similar behaviour in the case of a footing resting over the ground surface.

Based on the numerical results, the critical setback distance is identified for different slope angles, depth of foundation and soil friction angles. The normalised setback distance is represented in a tabular form in Table 2. A detailed table is included in the annexure (Table 3). Though Meyerhof [2] considered only a limited range of setback distances (0 to 6B) and depth of footing, the presented critical setback distances are compared with the Meyerhof [2].

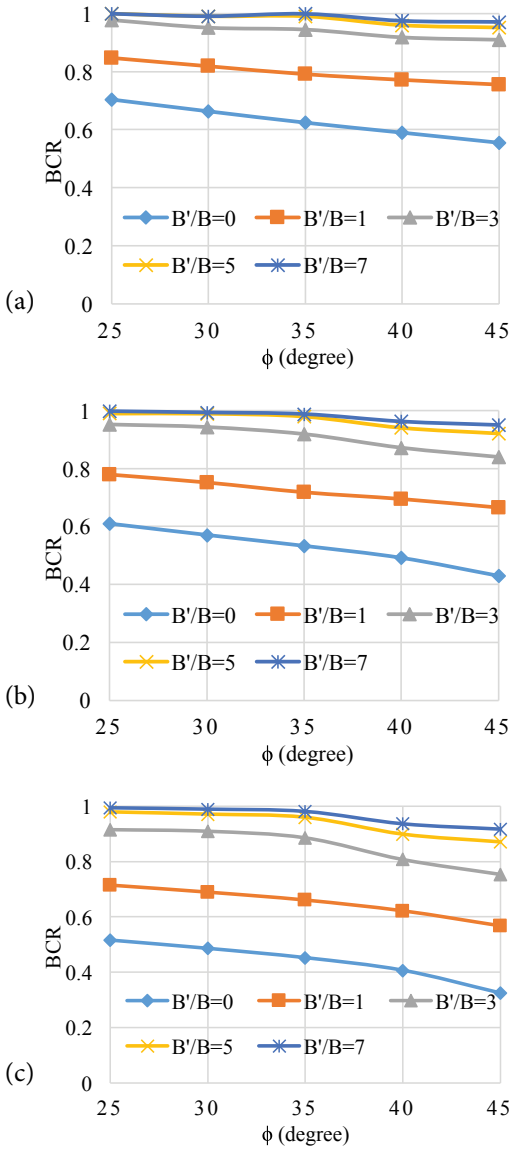

Figure 7. Effect of friction angle on BCR for a footing of zero embedment resting over soil of internal friction 35º. (a) 10H: V, (b) 4H: 1V and (c) 3H: 1V.

Table 2. Normalised critical setback distance for cohesionless soils.

Friction angle (φ^0)	Slope gradient, G (V/H)	Critical Setback distance (B'/B) from present study	Meyerhof [6]
25	1/10–1/3	2–3	-
30	1/10–1/4	3	-
	1/3–1/2	4–5	3
35	1/10–1/4	4–5	-
	1/2 –1/1.5	6–7	5
40	1/10–1/5	5–6	>6
	1/4 –1/3	6–7	>6
	1/2–1/1.3	8–9	-
45	1/10–1/4	8–9	-
	1/3–1/2	9–10	-
	1/1.5–1/1.2	>10	-

A steep slope of low relative density soil (low angle of internal friction) loses its stability with the application of a small magnitude load. In this condition, the slope sometimes fails itself and sometimes the foundation soil fails by means of local or punching shear failure (small area of shear zone). In both conditions a very small volume of soil is involved in the strength mobilization, without affecting the large mass of soil. In contrast, in the dense sand, failure is normally a general shear failure (a large area of shear zone). The larger area of soil contributes to the resistance against failure, and a large setback distance requires to mobilize the full strength of the soil. Chang et al. [34] and Raftari et al. [35] also found that the depth and the area of the shear zones increase with an increase in the setback distance in the reinforced slope. Similar to the present study, almost all previous studies also found that the critical distance increases with the increase in the angle of shearing resistance or the relative density of the soil.

5 STATISTICAL ANALYSES

Statistical analyses were also performed to determine the factors affecting the BCR using the results of numerical analyses. A simple multiple regression and correlation analysis along with other statistical tests were performed to derive an equation to determine the BCR of a footing resting over cohesionless soil.

As it can be seen from the numerical analysis, a total of four independent parameters (i.e., setback distance, slope gradient, soil friction angle and depth ratio of footing.) are influencing the bearing capacity of a footing resting near the slope. The results of the numerical study show that the relationship between the independent parameters and the bearing capacity ratio is not linear, and hence it is necessary to consider the nonlinearity in order to develop an equation for the BCR calculation. As an exact nonlinearity in the relationship is not known initially, it was assumed that the BCR is not only depending on these four parameters, but also upon various derivatives as well.

Initially, a total of 96 parameters, which are the function of these 4 independent variables, are considered in the regression analysis. T-Tests were performed to determine the dependency of the BCR on these parameters. Along with the probability level, the R^2 value was used to determine the critical factor affecting the BCR. The degree of multicollinearity was used to remove the insignificant parameters. It was found from these studies that only 12 parameters, including the four basic parameters, critically affect the bearing-capacity ratio. Later these 12 variables were used to develop the equation for the bearing capacity ratio.

Figs. 8 (a) and (b) respectively show the residues of the BCR (observed BCR-predicted BCR) versus the percentage of the value for 96 and 12 variables. The equation was developed as a consequence of a comparative study carried out to develop an equation that can predict the effect of the slope inclination and the foundation geometry very effectively. Based on a regression analysis and a comparative analysis, an equation is proposed to estimate the BCR. For this, various type of functions, such as logarithmic, linear, polynomial and exponential functions, were assumed and the best relationship is used to develop the equation. It was found that R^2 is reduced from 0.9947 to 0.987, when the number of insignificant variable were removed from the analysis. It ensures that the other assumed dependents parameters are not affecting the bearing capacity, as assumed in the initial phase of the regression analysis. Based on the T Test, the probability level and the degree of multicollinearity, the following order can be assigned to the factors, critically affecting the bearing capacity: Slope > Setback distance

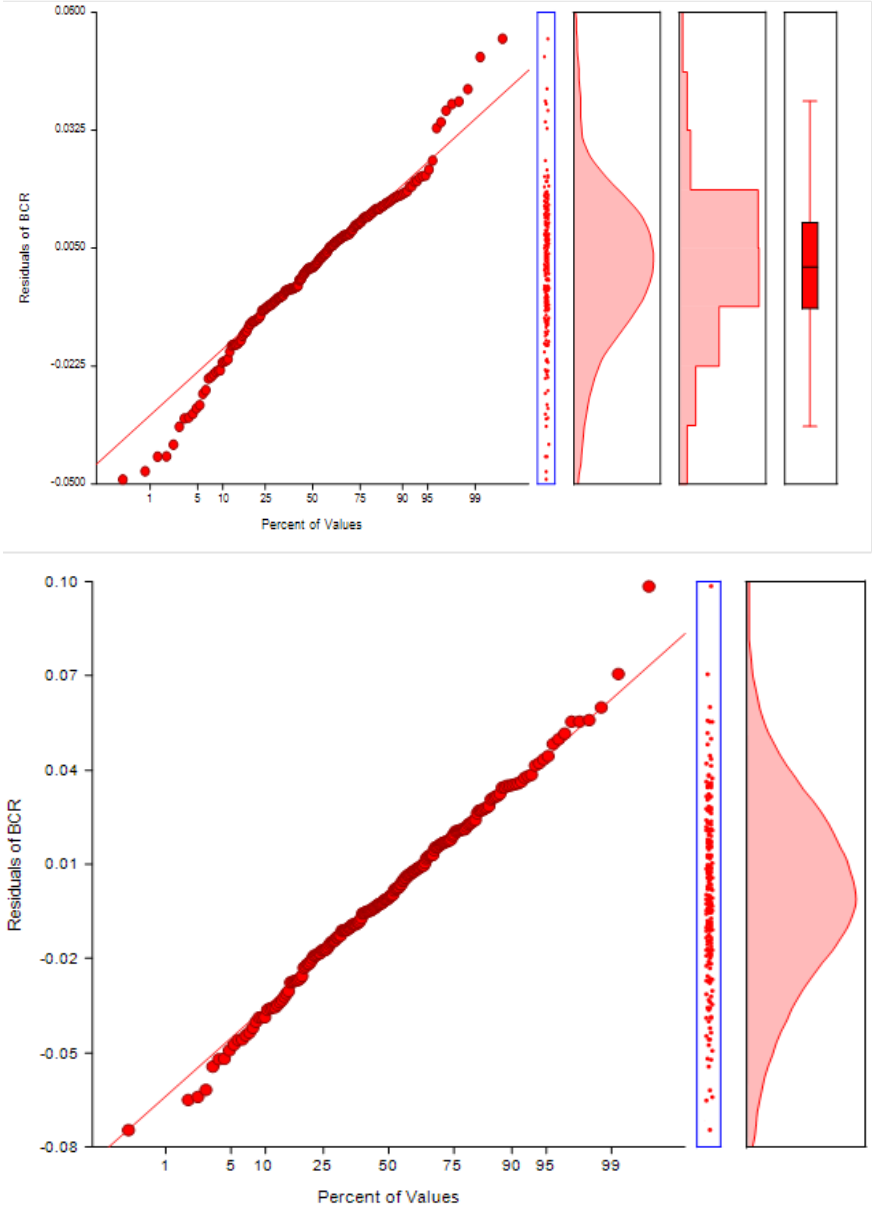

Figure 8. Residuals versus percentage of values (a) for 156 independent variables (b) for 12 independent variables.

> Friction angle > Depth ratio of footing. The effect of the depth ratio of the footing on the bearing capacity is very nominal, as compared to the other three factors. Equation 1 shows the BCR equation developed to determine the influence of the slope geometry and the angle of internal friction of the soil. Annexure shows an equation that is relatively complex, but it can predict a change in the bearing capacity with a higher accuracy.

$$BCR = 1 + 0.044B'/B(1 - 0.14B'/B + 0.09D/B + 3.4\beta) + 0.06D/B(D/B - 1) - 0.4\beta(1 + 0.35\beta + 0.8D/B + 2.1\tan\varphi) + \tan\varphi(1 - 1.2\tan\varphi - 0.15D/B + 0.15B'/B) \quad (1)$$

where BCR = Bearing capacity ratio, B' = setback distance, B = width of footing, D = depth of footing, β = soil slope in radian and φ = angle of internal friction of the soil.

5.1 Validation of the equation with experimental and analytical analysis

The proposed Eq. 1 is validated with the experimental results of Keskin and Laman [26]. Fig. 9 shows a reasonably good agreement between the BCR predicted from the proposed equation and the experimentally measured BCR values of Keskin and Laman [26]. The predicted BCR values up to the setback distance of 4B are a little higher than Keskin and Laman [26], but these differences are within the acceptable ranges (0–15%). This variation might be attributed to the scaling effect as the numerical modelling was carried out on a prototype model, while Keskin and Laman [16] performed small-scale model testing in the laboratory. Keskin and Laman [26] used the relative density of the sand in the analysis, and it has been converted to the friction angle of the soil using a relationship given by Schmertmann [36] for comparing the results. This might be another reason responsible for the minor differences observed between the experimental values and the values predicted from the developed regression equation.

The results are also compared with the analytical analysis results of Huang and Kang [14]. To make this comparison, the results were reproduced in a different form. Here, BCR represents the ratio of the bearing capacity of the footing resting some distance from the slope crest to the bearing capacity of the footing resting precisely on the slope crest. Fig. 10 shows the comparison of the results with Huang and Kang [14]. Graphs with dotted lines show the results of Huang and Kang [14], and the solid lines show the results of the present study. The results of the former study show that the BCR become constant precisely after a certain value of the setback distance. Whereas in the present case, though BCR is not becoming constant, but the rate of increase in the BCR becomes insignificant after a certain value of setback distance. In comparison to the results of Huang and Kang [14], the BCR measured in the present study is higher for the small slope. Whereas

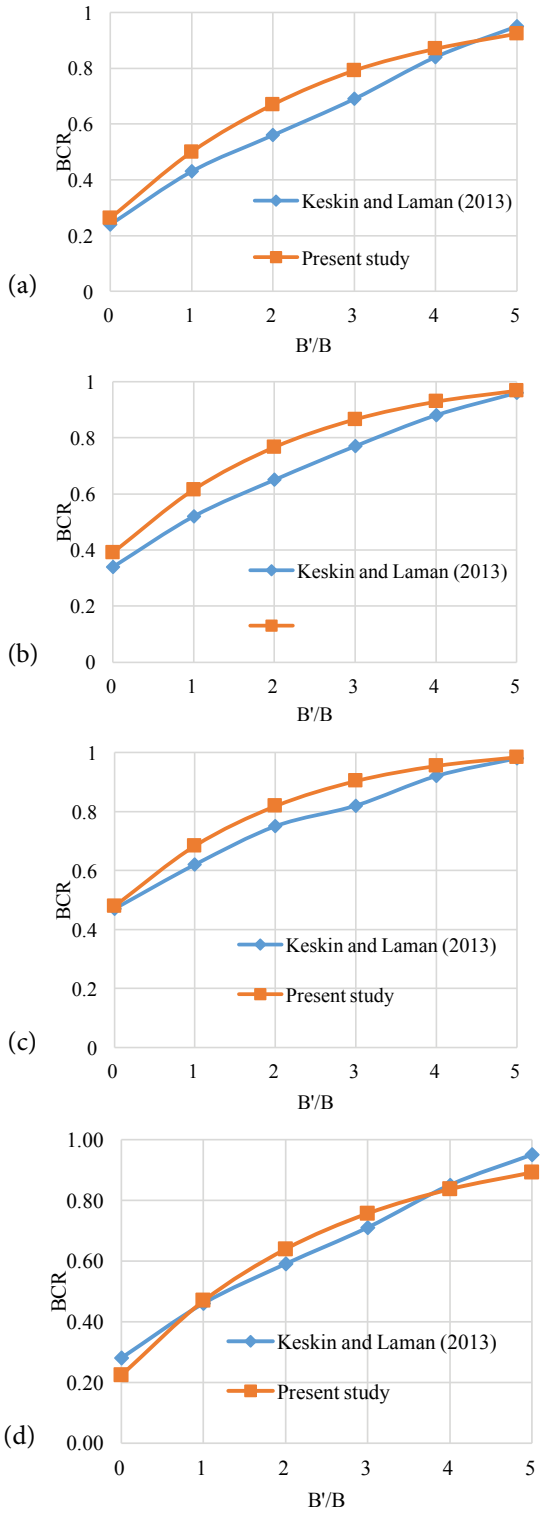

Figure 9. Variation of BCR with setback distance. (a) for soil slope 30°, φ=32°, (b) for soil slope 25°, φ=32°, (c) for soil slope 20°, φ=32° and (d) for soil slope 30°, φ=40°.

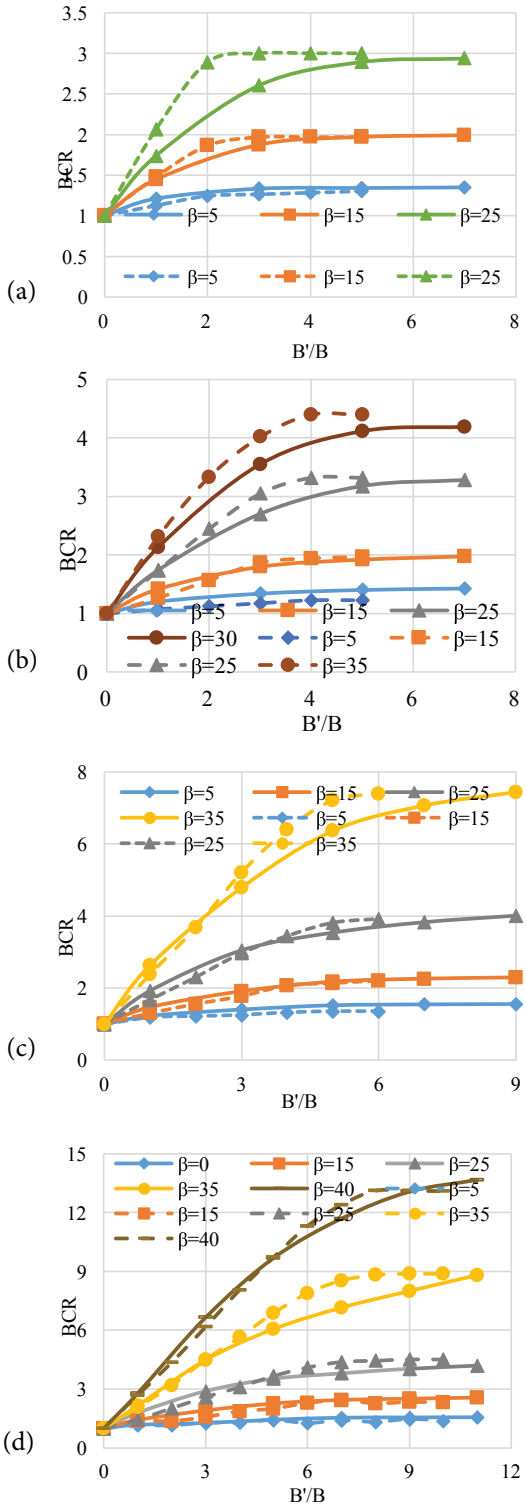

Figure 10. Comparison of results with analytical results of Huang and Kang [14] shown by dashed lines for surface footing resting on slope. (a) φ=30°, (b) φ=35°, (c) φ=40° and (d) φ=45°.

in the case of a higher slope angle, the BCR evaluated from the present study is smaller than the BCR of the former studies.

6 CONCLUSION

The slopes have an adverse effect on the bearing capacity of a footing. The slope gradient, setback distance, angle of internal friction of the soil and the depth ratio of footing affects the bearing capacity of a footing resting over the slope. The bearing capacity decreases with an increase in the slope gradient. The reduction in the bearing capacity with the slope gradient is relatively higher for a footing of large embedment depth and when the footing is resting near the slope crest. Particularly for dense sand, the effect of the slope gradient on the reduction in the bearing capacity is observed, even up to very large setback distances of 11B. Soil deformation also increases with an increase in the slope gradient. At a low slope gradient, the orientation of the failure surface and the soil deformation are very much similar to the footing resting on the level ground. Both the failure surface and the direction of propagation of soil deformation oriented downwards and towards the slope surface with an increase in the slope gradient.

The soil confinement and strength mobilization on the level side of the footing increase with an increase in the setback distance; therefore, the bearing capacity increases. The critical setback distance is increasing with an increase in the friction angle of the soil, the slope gradient and the depth of footing. The reduction in the bearing capacity with slope inclination increases with an increase in the internal friction of the soil and the depth of footing. The effect of the depth of foundation on the reduction in the BCR is relatively higher when the footing is resting near the slope crest. The predicted BCR is well matching with the BCR determined in the previous analytical and experimental studies.

REFERENCES

[1] Sarma, S. K., Chen, Y. C. 1995. Seismic bearing capacity of shallow strip footings near sloping ground. The 5th SECED conference on European seismic design practice, Balkema, Rotterdam, 505-512.

[2] Meyerhof, G. G. 1957. The ultimate bearing capacity of foundation on slopes. 4th Int. Conf. on Soil Mech. and Foundation Eng., 3, 384-386.

[3] Hansen, J.B. 1970. A revised and extended formula for bearing capacity. Dan. Geotech. Ins., Bulletin 28.

[4] Shields, D., Chandler, N., Garnier, J. 1990. Bearing capacity of foundations in slopes. Journal of geotechnical engineering 116, 3, 528-537.

[5] Kusakabe, O., Kimura, T., Yamaguchi, H. 1981. Bearing capacity of slopes under strip loads on the top surfaces. Soils and Foundation, JGS 21, 4, 29-40. DOI: http://doi.org/10.3208/sandf1972.21.4_29.

[6] Graham, J., Andrews, M., Shields, D. H. 1988. Stress characteristics for shallow footings in cohesionless slopes. Canadian Geotechnical Journal 25, 2, 238-249. DOI: http://dx.doi.org/10.1139/t88-028

[7] Tatsuoka, F., Huang, C.C., Morimoto, T., Okahara, M. 1989. Stress characteristics for shallow footings in cohesionless slopes. Discussion. Canadian Geotechnical Journal 26, 4, 748-755. DOI: http://dx.doi.org/10.1139/t89-088

[8] Bowles, J.E. 1988. Foundation engineering and design. 5th Edition, McGraw-Hill, Inc.

[9] Saran, S., Sud, V., Handa, S. 1989. Bearing capacity of footings adjacent to slopes. Journal of geotechnical engineering 115, 4, 553 – 573. DOI: http://dx.doi.org/10.1061/(ASCE)0733-9410(1989)115:4(553)

[10] Michalowski, R. L. 1991. Discussion of bearing capacity of footings adjacent to slopes by Swami Saran, VK Sud and SC Handa. Journal of Geotechnical Engineering 117, 7, 1125-1127. DOI: http://dx.doi.org/10.1061/(ASCE)0733-9410(1991)117:7(1125.2)

[11] Narita, K., Yamaguchi, H. 1990. Bearing capacity analysis of foundations on slopes by use of log-spiral sliding surfaces. Soils and Foundation, JGS 30, 3, 144-152. DOI: http://doi.org/10.3208/sandf1972.30.3_144

[12] De Buhan, P., Garnier, D. 1998. Three dimensional bearing capacity analysis of a foundation near a slope. Soils and Foundations, JGS 38, 3, 153-163. DOI: http://doi.org/10.3208/sandf.38.3_153.

[13] Lee, K. M., Manjunath, V. R. 2000. Experimental and numerical studies of geosynthetic-reinforced sand slopes loaded with a footing. Canadian Geotechnical Journal 37, 828–842. DOI: http://doi.org/10.1139/t00-016

[14] Huang, C.C., Kang, W.W. 2008. The effects of a setback on the bearing capacity of A surface footing near a slope. Journal of GeoEngineering 3, 1, 25-32. DOI: http://doi.org/10.6310/jog.2008.3(1).3

[15] Castelli, F., Motta, E. 2010. Bearing capacity of strip footings near slopes. Geotechnical and Geological Engineering 28, 2, 187-198. DOI: http://doi.org/10.1007/s10706-009-9277-9

[16] El Sawwaf, M. 2010. Experimental and numerical study of strip footing supported on stabilized sand slope. Geotechnical and Geological Engineering 28, 4, 311-323. DOI: http://doi.org/10.1007/s10706-009-9293-9

[17] Naeini, S. A., Rabe, B. K., Mahmoodi, E. 2012. Bearing capacity and settlement of strip footing on geosynthetic reinforced clayey slopes. Journal of Central South University 19, 4, 1116-1124. DOI: http://doi.org/10.1007/s11771-012-1117-z

[18] Gill, K. S., Choudhary, A. K., Jha, J.N., Shukla, S. K. 2013. Large model footing load test on reinforced coal ash slope. International Journal of Geotechnical Engineering 7, 3, 257-265. DOI: http://doi.org/10.1179/1938636213Z.00000000040

[19] Nouri, M. 2014. Interaction domain of shallow foundations on the top of a slope. Master Dissertation, Department of Civil, Environmental and Land Management Engineering, Polytechnic University of Milan. Itly.

[20] Rostami, V., Ghazavi, M. 2015. Analytical solution for calculation of bearing capacity of shallow foundations on geogrid-reinforced sand slope. IJST, Transactions of Civil Engineering 39, C1, 167-182.

[21] Andrew, M. 1986. Computation of bearing capacity coefficients for shallow footing on cohesionless slopes using stress characteristics. M.Sc. thesis, University of Manitoba, Winnipeg, Manitoba.

[22] Gamier, J., Canepa, Y., Corte, J.F., Bakir, N.E. 1994. Etude delaPortance de Foundations enBorddeTalus. 13th Int. Conf. on Soil Mechanics and Foundation Engineering 2, 705-708.

[23] Georgiadis, K. 2010. Undrained bearing capacity of strip footings on slopes. Journal of Geotechnical and Geoenvironmental Eng. 136, 5, 677-685. DOI: http://doi.org/10.1061/(ASCE)GT.1943-5606.0000269

[24] Altalhea, E. B., Taha, M.R., Abdrabbob Fathi, M. 2015. Behavior of strip footing on reinforced sand slope. Journal of Civil Engineering and Management 21, 3, 376-383. DOI: http://doi.org/10.3846/13923730.2014.890646

[25] Jao, M., Ahmed, F., Muninarayana, G., Wang, M. C. 2008. Stability of eccentrically loaded footings on slopes. Geomechanics and Geoengineering 3, 2, 107-111. DOI: http://doi.org/10.1080/17486020802010772

[26] Keskin, M.S., Laman, M. 2013. Model studies of bearing capacity of strip footing on sand slope. KSCE Journal of Civil Engineering 17, 4, 699-711. DOI: http://doi.org/10.1007/s12205-013-0406-x

[27] Ausilio, E. 2014. Seismic bearing capacity of strip footings located close to the crest of geosynthetic reinforced soil structures. Geotechnical and Geological Engineering 32, 4, 885-899. DOI: http://doi.org/10.1007/s10706-014-9765-4

[28] Peck, R. B., Hanson, W. E., Thornburn, T. H. 1974. Foundation engineering. (Second edition), Wiley, New York.

[29] Krabbenhoft, K., Lyamin, A., Krabbenhoft, J. 2015. Optum computational engineering, (www.optumce.com).
[30] Keawsawasvong, S., Ukritchon, B. 2016. Finite element limit analysis of pullout capacity of planar caissons in clay. Computers and Geotechnics 75, 12-17. DOI: http://dx.doi.org/10.1016/j.compgeo.2016.01.015
[31] Lyamin, A. V., Sloan, S. W., Krabbenhøft, K., Hjiaj, M. 2005. Lower bound limit analysis with adaptive remeshing. International Journal for Numerical Methods in Engineering 63, 14, 1961-1974. DOI: http://doi.org/10.1002/nme.1352
[32] Martin, C. M. 2011. The use of adaptive finite-element limit analysis to reveal slip-line fields. Géotechnique Letters 1, 2, 23-29. DOI: http://dx.doi.org/10.1680/geolett.11.00018
[33] Varzaghani, I. M., Ghanbari, A. 2014. A new analytical model for determination of seismic settlement of foundations adjacent to slope. Geomechanics and Engineering 6, 561-575. DOI: http://dx.doi.org/10.12989/gae.2014.6.6.561
[34] Chang, J. C., Liao, J. J., Pan, Y.W. 2008. Bearing behavior and failure mechanism of a shallow foundation located on/behind the crest of a poorly cemented artificial sandstone. International Journal of Rock Mechanics and Mining Sciences 45, 8, 1508-1518. DOI: http://doi.org/10.1016/j.ijrmms.2008.01.013
[35] Raftari, M., Kassim, K.A., Rashid, A.S.A., Moayedi, H. 2013. Settlement of shallow foundations near reinforced slopes. EJGE 18, Bund. D, 797-808.
[36] Schmertmann, J. H. 1978. Guidelines for cone penetration test: Performance and Design, FHWA-TS-78-209 (report), U.S. Dept. of Transportation.

Table 3. Normalised critical setback distance for cohesionless soil.

Friction angle (φ^0)	Slope gradient, G (V/H)	Depth of Embedment (B/D)	Critical Set-back distance (S/B)	Meyerhof et al. [5]
25	1/10–1/5	0.5	2	-
	1/5–1/3	1	3	-
30	1/10–1/4	0	2	2
		0.5	3	
		1	3–4	
	1/4–1/2	0	3	3
		0.5	3–4	
		1	4–5	
35	1/10–1/5	0	4–5	
		0.5	5	
		1	5–6	
	1/4–1/2	0	5–6	
		0.5	6	
		1	6–7	
	1/2–1/1.5	0	5–6	
		0.5	6–7	
		1	7–8	
40	1/10–1/5	0	5–6	
		1	6–7	
	1/5 –1/2	0	6–7	>6
		1	7–8	
	1/2–1/1.3	0	7–8	>5
		1	8–9	>7
45	1/10–1/4	0	7–8	
		1	8–9	
	1/4–1/2	0	8–9	
		1	10–11	
	1/2–1/1.2	0	>12	
		1	>12	

Annexures:

The equation to calculate the bearing-capacity ratio more accurately

$$BCR = 0.047B'/B + 0.32D/B + 4.46\tan\varphi - 0.02(B'/B)^2(1 - 0.34D/B - 0.75\tan\varphi + 0.15\beta) - \beta^2(1 + 0.2\beta - 1.9\tan\varphi - 0.36D/B + 0.19b/B) - 6.45\tan\varphi^2(1 + 0.45\tan\varphi + 0.16\beta - 0.04D/B + 0.01b/B) - D/B^2(1 - 0.7D/B + 0.017b/B - 0.22\beta - 0.04\tan\varphi) + 0.034(b/B)D/B(1 - 2.35\tan\varphi) + 0.42(b/B)\beta(1 - 0.07D/B) + 0.1(b/B)\tan\varphi(1 - 1.23\beta) - 0.2(D/B)\tan\varphi(1 + 0.5\beta) - \beta(1 - 0.24\tan\varphi + 0.55D/B)$$

STRIŽNI MODUL ZASIČENE GRANULIRANE ZEMLJINE IZ PREIZKUSA RESONANČNE KOLONE

H. Patiño
Universidad Politécnica de Madrid (UPM)
Madrid, Španija

E. Martínez
Universidad Politécnica de Madrid (UPM)
Madrid, Španija

Jesús González
Universidad Politécnica de Madrid (UPM)
Madrid, Španija
E-pošta: jesus.gonzalezg@upm.es

A. Soriano
Universidad Politécnica de Madrid (UPM)
Madrid, Španija

Ključne besede

resonančna kolona; resonančna frekvenca; strižni modul; relativna gostota; efektivni konsolidacijski tlak; dinamični strižni modul

Izvleček

V prispevku so predstavljeni rezultati 120 preizkusov določitve strižnega modula (G) zasičenih granuliranih zemljin (20–40 odstotni Ottawa pesek) v različnih pogojih relativne gostote (D_r), efektivnega konsolidacijskega tlaka (σ'_c) in nivoja torzijske indukcije (T_e). Uporabljena je bila resonančna kolona, ki jo je izdelal Wykeham Farrance. Preizkusi so bili izvedeni z relativnimi gostotami 20, 40, 60 in 80 %, efektivnimi konsolidacijskimi tlaki 50, 100, 150, 200, 250 in 300 kPa ter nivoji torzijskih indukcij 0.025, 0.05, 0.1, 0.2 in 0.4 voltov (V), da smo dobili strižne specifične deformacije (γ) med 0.002 % in 0.023 %. Rezultati so privedli do zelo preprostih empiričnih izrazov za strižni modul kot funkcijo strižne specifične deformacije za različne vrednosti efektivnih konsolidacijskih tlakov in količnikov por.

SHEAR MODULUS OF A SATURATED GRANULAR SOIL DERIVED FROM RESONANT-COLUMN TESTS

H. Patiño
Universidad Politécnica de Madrid (UPM)
Madrid, Spain

E. Martínez
Universidad Politécnica de Madrid (UPM)
Madrid, Spain

Jesús González
Universidad Politécnica de Madrid (UPM)
Madrid, Spain
E-mail: jesus.gonzalezg@upm.es

A. Soriano
Universidad Politécnica de Madrid (UPM)
Madrid, Spain

Keywords

resonant column; resonant frequency; shear modulus; relative density; effective consolidation pressure; dynamic shear modulus

Abstract

This paper presents the results of 120 determinations of the shear modulus (G) of a saturated granular soil (20–40 Ottawa sand) in different conditions of relative density (D_r), effective consolidation pressure (σ'_c) and level of torsional excitation (T_e). The equipment used was a resonant-column apparatus manufactured by Wykeham Farrance and the tests were performed with relative density values of 20, 40, 60 and 80%, effective consolidation pressures of 50, 100, 150, 200, 250 and 300 kPa, and torsional excitations of 0.025, 0.05, 0.1, 0.2 and 0.4 volts (V), leading to shear strains (γ) between 0.002% and 0.023%. The results led to very simple empirical expressions for the shear modulus as a function of the angular strain for different effective consolidation pressures and void-ratio values.

1 INTRODUCTION

The dynamic behaviour of granular soils has been intensively studied around the world for several decades now and the results obtained from various research programs are disseminated through the proceedings of international conferences and indexed journals related to geotechnical engineering. Since there is abundant information on the dynamic behaviour of granular soils and many of the topics dealt with are commonplace; this paper will only focus on references directly related to resonant-column tests, either from the point of view of the development of the test itself or from their utilization to obtain shear-wave velocities, shear-stiffness moduli and damping ratios.

The resonant column was first used by Ishimato and Iida (1937) [1] and Iida (1938, 1940) [2, 3] to test Japanese soils, and then nearly two decades later by Bishop (1959) [4]. Since the 1960s, this technique has been widely used in many countries and has been subjected to countless modifications in the restraints applied to the specimen ends. Some of the many works on this matter are described below. For the sake of clarity, the references have been grouped by the main objective of the research rather than following a chronological order. Appearing first are the most relevant analyses of the test apparatus itself and of how to use the resonant column. Wilson and Dietrich (1960) [5] used one of the most novel – at that time – resonant columns in the USA to test clay samples. Hall and Richard (1963) [6] designed and developed a "fixed–free" resonant-column apparatus, i.e., the specimen is fixed at the base and free at the upper end, therefore allowing the soil samples to be subjected to torsional and longitudinal vibrations. Drnevich *et al.* (1966, 1967) [7, 8] developed equipment for hollow

cylindrical soil specimens, to determine the shear modulus and the damping ratio under large deformations; the reason for using hollow specimens being related to the difficulty in obtaining a representative value of the angular strain in solid samples. In addition, they developed the theory in which the interpretation of the results obtained from the resonant column test is based. The operational principle of resonant-column equipment, the calibration recommendations, the processing of the data and the interpretation of the results were clearly described by Drnevich *et al.* (1978) [9]. Menq (2003) [10] developed a resonant-column apparatus that allows testing of specimens up to 15 cm in diameter that was used to study the dynamic properties of sand and gravel. Clayton *et al.* (2009) [11] used aluminium rods of various diameters to evaluate the polar moment of inertia of the excitation system (I_o) and found that this value depended on the stiffness of the rod employed in calibrating their apparatus. However, calibrating the resonant column employed for our research led to a constant I_o value. Clayton (2011) [12] refers to some in-situ and laboratory methods to estimate the stiffness and analysed in detail factors influencing the stiffness value obtained from very-small-strain tests, like the range of strains, anisotropy and velocity of loading.

Recently, some manufacturers of equipment for obtaining dynamic parameters have marketed relatively sophisticated models for resonant column tests that allow better control and better simulation during execution of the tests; among others Wykeham Farrance in the UK, which made the device used for this investigation. A detailed description of the equipment is presented later on.

In general, the resonant column test is the most commonly used laboratory technique to measure the dynamic properties of soils subjected to a low level of deformation. The various designs developed so far imply the application of axial or torsional harmonic loads to solid or hollow specimens by means of electro-magnetic systems capable of accurately controlling the frequency and amplitude of the different types of waves that can be generated. On the other hand, Al-Sanad and Aggour (1984) [13] applied random loads and Tawfig *et al.* (1988) [14], impulsive loads.

Resonant-column tests also make it possible to determine the velocity of shear waves and to analyse their influence on other test parameters. Some researches on this point are presented below. Hardin and Richart (1963) [15] measured the shear-wave propagation velocity in samples prepared with Ottawa sand, with crushed quartz sand and with crushed quartz silts, subjected to small strains, and they proposed empirical correlations to calculate the shear modulus as a function of the void ratio and the effective consolidation pressure. Hardin (1965) [16], based on the theory of linear vibrations of a cylindrical rod, presents an expression to calculate the shear wave propagation velocity (V_s) as a function of the resonant frequency, the polar moment of inertia, the height of the specimen and the polar moment of inertia of the system. Richart *et al.* (1970) [17] proved mathematically that proportionality exists between the resonant frequency of the specimen and the corresponding shear-wave propagation velocity. Santamarina and Cascante (1996) [18] used a resonant column apparatus capable of applying both compressive and tensile deviatoric stresses to measure the velocity of shear and damping waves under small strains. These velocities turned out to depend mainly on the isotropic stress, while the deviatoric stress played a lesser role.

Probably, the factor most often analysed with this equipment has been the shear modulus, obtained in cyclic shear tests.

Kuribayashi *et al.* (1975) [19] found that the shear modulus of several materials is not a function of the relative density, but rather of the void ratio. Iwasaki *et al.* (1978) [20] present the average variation trend of the shear modulus in eight different types of sand as a function of the angular strain. In addition, they found that in the case of Toyura sand, within a wide range of deformations, a linear relationship exists between the shear modulus and the effective consolidation pressure. Tatsuoka *et al.* (1979) [21] determined that the shear modulus, within a wide range of deformations, is not affected by the initial structure of the tested specimens. Alarcón-Guzmán *et al.* (1989) [22] investigated the effect of the principal stress ratio on the shear modulus, concluding that this factor has a less important effect on the determination of the maximum shear modulus, but drastically affects the secant shear modulus. Saxena *et al.* (1989) [23] extensively reviewed empirical relations for obtaining G_{max} and the damping (D) under small strain and conducted resonant-column tests on Monterey No. 0 Sand and showed that published relations overestimated G_{max} and underestimated D for this sand. Lo Presti *et al.* (1997) [24] evaluated the influence of the strain rate in the determination of the shear modulus of granular soils, and found that this factor has a very small effect on the maximum shear modulus. Díaz-Rodríguez and López-Flores (1999) [25] proposed an empirical function (a potential expression) between the shear modulus and the isotropic consolidation stresses (σ'_c). Wichtmann and Triantafyllidis (2004) [26] analysed the influence of the history of dynamic loading on the properties of dry sands; the results thus obtained indicated that a dynamic pre-stressing moderately affects the shear modulus under small deformations. Gu *et al.* (2013) [27] used bender

elements to test three different sands subjected to small strains and found that both G_o (shear modulus) and M_0 (constraint modulus) increase with the density and the confining pressure. They found G_o to be more sensitive to E_0 (Young's modulus) and proposed empirical relations between the Poisson ratio and G_o and M_0.

Finally, some works are presented that analyse how the soil identification properties (grading, particle shape, etc.) influence results.

Chang and Ko (1982) [28] tested 23 samples of Denver sand and found that the maximum shear modulus is – to a large extent – a function of the coefficient of uniformity, whereas the effect of the mean size of the particles is minimal. Koono *et al.* (1993) [29] executed what can be regarded as a field resonant-column test in a gravel deposit. Wichtmann and Triantafyllidis (2009, 2013 and 2014) [30, 31, 32] evaluated the influence of the coefficient of uniformity and of the grain size distribution for 27 types of clean sand in the determination of the maximum shear modulus: the results obtained indicate that for equal values of the void ratio and of the effective consolidation pressure, the maximum shear modulus decreases as the coefficient of uniformity increases, whereas it does not change with the mean particle size. Martínez (2012) [33] studied the influence of the soil index properties on the determination of the dynamic parameters of a saturated granular soil. Senetakis *et al.* (2012) [34] tested sands with different grading curves, particle origin and shape under very small strains. Volcanic sands showed significantly lower G_o values than those of quartz sands, whereas their D_0 were only slightly lower compared to quartz sands.

Yang and Gu (2013) [35] found that, in the range of small strains, the shear modulus varies very little in terms of particle size.

Senetakis and Madhusudhan (2015) [36] tested quartz sands and angular-grained gravels and they proposed potential functions to relate G_o with p'. The exponent n_G was shown to be dependent on the specimen preparation procedure. Finally, Payan *et al.* (2016) [37, 38] observed that the published formulae cannot accurately relate the shear modulus under small strain with the void ratio and confining pressure, probably because the particle shape was not taken into account. Based on critical-state theories, they propose a new expression, including the effect of grading curves and particle shapes.

Taking into account the background information presented above, the objective of this investigation is an in-depth study of the influence of the relative density, effective consolidation pressure and torsional excitation values on the shear modulus of a saturated granular sand and to develop simple empirical functions to correlate these parameters.

2 MATERIAL USED

The tests were performed on 20–40 Ottawa sand (maximum, minimum and average particle sizes are 0.85, 0.43 and 0.64 mm, respectively). It is a standard material employed in many other investigations into the behaviour of granular soil. Its main characteristics are: very hard, uniform particles (the coefficient of uniformity turned out to be Cu = 1.35), fine and rounded grains and nearly pure quartz in composition.

The index properties of particles passing mesh 20 and retained in mesh 40 are as follows: specific gravity $G_s = 2.669$, maximum void ratio $e_{max} = 0.754$, and minimum void ratio $e_{min} = 0.554$. The initial properties of the specimens tested are presented in Table 1.

Table 1. Properties of specimens tested.

Relative density, D_r, %	Height, H, mm	Diameter, D, mm	Mass, g	Dry density ρ_d, g/cm^3	Void ratio, e
20	105	49.5	314.59	1.557	0.714
40	105	49.5	322.13	1.594	0.674
60	105	49.5	330.05	1.633	0.634
80	105	49.5	338.36	1.675	0.594

2.2 Description of the equipment used

The resonant-column apparatus consists of a forced oscillation system with a single torsional degree of freedom that makes the specimen vibrate within a range of frequencies in which its first natural mode can be found. In this particular investigation, the specimen remained fixed at its base and was free to vibrate at its upper end.

Testing was performed with the resonant-column device manufactured by Wykeham Farrance, Fig. 1. The frequency of the resonant-column tests is higher than 10 Hz, while in cyclic torsional shear mode the equipment typically operates at frequencies below 2 Hz. In this research, the frequency range was between 74 Hz and 140 Hz.

This instrumented and automated equipment provides a series of advantages, among which mention can be made of the following. It combines resonant-column and simple torsional shear functions. It determines automatically the resonant frequency, the shear-wave velocity, the shear modulus, the angular strain and the damping ratio, this latter parameter by using the Half-Power

Figure 1. Resonant-column apparatus manufactured by Wykeham Farrance.

method or the Free Vibration Decay method. There is no need to externally use either an oscilloscope or a function generator. The internal floating structure for the excitation system allows the execution of tests in which the specimens can experience large axial deformations during consolidation. It makes it possible to visualize, in real time, the response of the sensors during the test.

The equipment is basically constituted by two polycarbonate hollow cylindrical cells allowing, by means of the internal cell, the application of the consolidation pressure to the specimen through a fluid, without the electronic components being submerged, and – through the external cell – the application to the fluid of a confining pressure provided by a pneumatically operated system; a lower base through which the back pressure is applied and drainage of the specimen is allowed during the consolidation stage; a corrugated head piece with no possibility of drainage, to transmit the torsional forces to the specimen; a driving mechanism constituted by eight coils and four magnets to apply the torsional load to the specimen; an accelerometer attached to the mechanism to generate the torsional action and to provide the information necessary to calculate the shear-wave propagation velocity (V_s); an LVDT to measure axial deformations (with a stroke of +/- 12.5 mm and an accuracy of 0.2%), two proximity transducers to measure angular deformations in case the data supplied by the accelerometer is not used to calculate them; three pressure transducers to measure the chamber pressure (σ_c), the back pressure (B_p) and the pore water pressure (u); a transducer to register volume changes during the consolidation stage; a compact unit fitted with a power source, a manual pressure regulator, two electric pressure regulators, eight electronic components for signal conditioning and a control and data-acquisition module; and a computer for equipment control and data acquisition.

3 THEORETICAL BACKGROUND

According to the theory of torsional vibrations in a cylindrical rod, expression (1) relates the shear-wave propagation velocity (v_s) to the shear modulus (G) and to the unit mass density (ρ).

$$v_s = \sqrt{\frac{G}{\rho}} \qquad (1)$$

Expression (2), obtained by Hardin (1965) [13], calculates the shear-wave propagation velocity (v_s) as a function of the resonant frequency (F_r), the polar moment of inertia of the excitation mechanism about its symmetry axis (I_o), the polar moment of inertia of the specimen about its symmetry axis (I) and the height of the sample (h).

$$\beta \cdot \tan\beta = \frac{I}{I_0}; \text{ where } \beta = \frac{2\pi \cdot F_r \ h}{v_s} \qquad (2)$$

Implicit equation (2) can be represented graphically as a function of β, as depicted in Fig. 2.

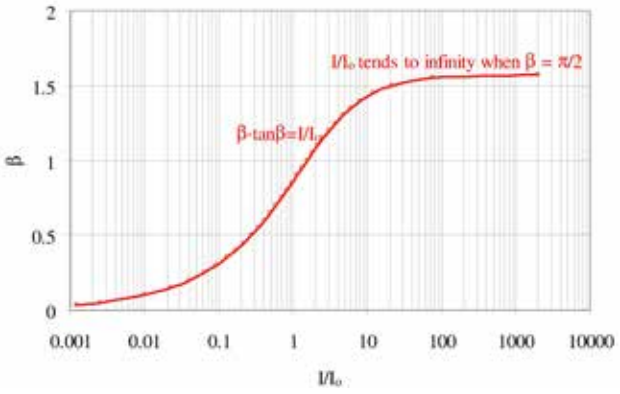

Figure 2. Graphical representation of the implicit equation (2).

Equation (3) is obtained from (1) and (2).

$$G = \frac{4\pi^2 h^2 \rho}{\beta^2} F_r^2 \qquad (3)$$

For this particular equipment the height of the specimen and the polar moment of the excitation mechanism are fixed constants. Their values are: h = 10.5 cm $I_o = 13.1 kg \cdot cm^2$.

I_o was obtained by calibration with two rods of the same dimensions and made up of different materials and turned out to be independent of the rod's stiffness. However, Clayton *et al.* (2009) [11] found that, in their equipment, I_o was dependent on the rod's stiffness. Our I_o value lies outside the range reported by them (2.99 to 4.32 $kg \cdot cm^2$) and it seems as though low values of I_o will depend on the rod's stiffness, while high I_o values will not.

The specimen diameter is D = 4.95 cm.

The densities of the samples used for this experiment range from

ρ_{sat}(min)=1.974 gr/cm^3 to ρ_{sat}(max)=2.048 gr/cm^3 or ρ_{sat} = 2.011 ± 0.037 gr/cm^3

For the central value, ρ_{sat} = 2 gr/cm^3, the value of the polar moment of inertia of the specimen is:

$$I = \frac{1}{32}\pi D^4 h\,\rho = 1.24 \text{ kg} \cdot \text{cm}^2 \qquad (4)$$

The corresponding value of β; obtained from equation (2)

$$\beta \cdot \text{tg}\,\beta = \frac{1.24}{13.1} = 0.0946 \text{ is} \quad \beta = 0.303 \text{ rd} \quad (\beta = 17.4^{\circ})$$

The shear-wave velocity can be obtained from the resonant frequency, F_r, measured during the test

$$v_s = \frac{2\pi F_r \cdot h}{\beta} = 2.18\, F_r \,\frac{m}{s} \quad (F_r \text{ en } H_z) \qquad (5)$$

and the corresponding value of the shear modulus $G = v_s^2 \cdot \rho = 9.51\, F_r^2$ kN/m^2 (F_r en H_z).

3.1 Experimental program

This investigation was aimed at determining the effect of the relative density, the effective consolidation pressure and the magnitude of the torsional excitation on the shear modulus.

A total of 120 determinations of the resonant frequency for saturated specimens were made in specimens measuring 49.5 millimetres in diameter and 105 millimetres in height. They all had a height-to-diameter ratio equal to 2.12, thus eliminating the uncertainty related to the slenderness of the specimens; the ratio specimen diameter to particle diameter was of about 120, therefore eliminating the scale effect.

The total number of tests is a result of the combination of relative densities equal to 20, 40, 60 and 80%, effective consolidation pressures equal to 50, 100, 150, 200, 250 and 300 kPa and amplitudes of sinusoidal waves equal to 0.025, 0.05, 0.1, 0.2 and 0.4 volts. The frequency varied between 74 Hz and 140 Hz, which corresponds to angular deformations between 0.002% and 0.023%. The backpressure was equal to 400 kPa for all the tests.

3.2 Preparation and setting of specimens

The accessories depicted in Fig. 3 that are necessary for making specimens with the sedimentation method were used to carry out the tests reported herein.

Figure 3. Basic elements for the specimen preparation: 1) lifting device of the three-part mould; 2) fixed lower base; 3) porous stone; 4) three-part split mould; 5) latex membrane; 6) O-Ring; 7) O-Ring stretcher; 8) extension of three-part mould; 9) 500-cm^3 beaker with de-aired water; and 10) loading head.

The sample-preparation procedure was similar to other laboratory tests using sand. The need to reproduce specimens complying with a certain relative density led to a setting process that was very careful and repetitive.

3.3 Effect of the sample density on the ratio $\frac{G}{F_r^2}$

The value of the ratio between the shear modulus and the square of the resonant frequency, G/F_r^2, turns out to be only slightly affected by the sample density.

In fact, the theoretical value of that ratio is:

$$R = \frac{G_r}{F_r^2} = \frac{4\pi^2 h^2}{\beta^2}\rho \qquad (6)$$

When the density, ρ, increases, the value of β also increases and the result is that the value of R is almost unchanged.

In fact, taking the derivative of R with respect to ρ, we obtain:

$$\frac{dR}{d\rho} = \frac{R}{\rho} - \frac{2R}{\beta}\cdot\frac{d\beta}{d\rho} \qquad (7)$$

From equation (2), and taking the previously indicated value of I, we obtain:

$$\beta \cdot \text{tg}\,\beta = \frac{1}{32}\frac{\pi D^4 h}{I_o}\cdot \rho \qquad (8)$$

Differentiating with respect to ρ gives:

$$\frac{d\beta}{d\rho}\left(\text{tg}\,\beta + \frac{\beta}{\cos^2\beta}\right) = \frac{\beta\,\text{tg}\beta}{\rho} \qquad (9)$$

to obtain:

$$\frac{d\beta}{d\rho} = \frac{\beta}{\rho} \cdot \frac{1}{1+\alpha}; \text{ being } \alpha = \frac{2\beta}{\text{sen } 2\beta} \qquad (10)$$

and, with the help of equation (7)

$$\frac{dR}{R} = \frac{d\rho}{\rho}\left(\frac{\alpha-1}{\alpha+1}\right) \qquad (11)$$

With $\alpha > 1$, any increase in the density always produces an increase in the value of R.

For the particular case of $\rho_{sat} = 2$ gr/cm^3 equations (10) and (11) are: $\alpha = \frac{2\beta}{\text{sen } 2\beta} = 1.064$ and $\frac{dR}{R} = 0.032\ \frac{d\rho}{\rho}$. The amplitude of the range of densities for this experimental program is $\frac{\Delta\rho}{\rho} = \frac{0.037}{2} = 0.019$ and, as a consequence, the relative variation of R is: $\frac{\Delta R}{R} \cong 0.00061$.

Thus, the rationale for normalizing G with respect to F_r^2 is that, for practical purposes and for the density range of the samples tested in this investigation, the ratio G/F_r^2 can be considered to be a constant that depends on the equipment characteristics, but it does not depend on the density of the sample being tested.

4 RESULTS

The results of the 120 determinations of the resonant frequency, the angular strains measured and the values of the shear modulus G thus obtained are presented in tables 2 and 3.

Table 2. Results corresponding to relative densities equal to 20 and 40%.

σ'_c	T_e	D_r = 20%			D_r = 40%		
		F_r	G	γ	F_r	G	γ
kPa	V	Hz	MPa	%	Hz	MPa	%
50	0.025	85.5	69.2	0.004	86.6	72.2	0.005
50	0.05	84.4	67.5	0.006	85.7	70.6	0.007
50	0.1	82.6	64.6	0.009	84.1	68.1	0.011
50	0.2	80.1	60.8	0.014	82.0	64.7	0.017
50	0.4	74.7	52.8	0.019	77.2	57.4	0.023
100	0.025	105.0	104.0	0.002	107.0	110.0	0.005
100	0.05	104.0	102.0	0.004	106.0	107.0	0.007
100	0.1	102.0	98.1	0.008	106.0	107.0	0.011
100	0.2	99.7	94.1	0.014	103.0	101.0	0.016
100	0.4	95.0	85.5	0.022	99.0	94.0	0.023
150	0.025	116.0	128.0	0.003	119.0	135.0	0.004
150	0.05	115.0	126.0	0.005	118.0	132.0	0.007
150	0.1	113.0	122.0	0.009	117.0	131.0	0.010
150	0.2	111.0	117.0	0.014	115.0	126.0	0.015
150	0.4	107.0	108.0	0.022	111.0	117.0	0.022
200	0.025	125.0	147.0	0.003	128.0	155.0	0.004
200	0.05	123.0	144.0	0.005	126.0	152.0	0.006
200	0.1	122.0	142.0	0.009	126.0	151.0	0.010
200	0.2	120.0	137.0	0.014	123.0	145.0	0.015
200	0.4	117.0	129.0	0.020	120.0	137.0	0.020
250	0.025	131.0	163.0	0.003	135.0	172.0	0.004
250	0.05	130.0	160.0	0.005	134.0	170.0	0.006
250	0.1	128.0	156.0	0.009	133.0	168.0	0.009
250	0.2	127.0	153.0	0.014	131.0	162.0	0.014
250	0.4	123.0	143.0	0.019	127.0	154.0	0.017
300	0.025	137.0	178.0	0.003	141.0	188.0	0.003
300	0.05	136.0	175.0	0.005	140.0	185.0	0.005
300	0.1	135.0	174.0	0.009	139.0	183.0	0.009
300	0.2	133.0	167.0	0.014	137.0	178.0	0.014
300	0.4	129.0	158.0	0.017	134.0	171.0	0.016

Table 3. Results corresponding to relative densities equal to 60 and 80%.

σ'_c	T_e	D_r = 60%			D_r = 80%		
		F_r	G	γ	F_r	G	γ
kPa	V	Hz	MPa	%	Hz	MPa	%
50	0.025	87.4	73.4	0.005	88.8	74.7	0.003
50	0.05	84.9	69.3	0.007	87.7	72.8	0.006
50	0.1	84.1	68.1	0.010	86.6	71.1	0.009
50	0.2	80.9	63.0	0.015	83.4	66.0	0.014
50	0.4	77.7	58.0	0.022	79.0	59.2	0.020
100	0.025	104.0	104.0	0.004	109.0	113.0	0.004
100	0.05	104.0	103.0	0.007	108.0	111.0	0.006
100	0.1	103.0	101.0	0.011	107.0	108.0	0.009
100	0.2	100.0	96.3	0.016	104.0	103.0	0.014
100	0.4	96.4	88.8	0.023	100.0	94.9	0.021
150	0.025	117.0	131.0	0.004	121.0	140.0	0.004
150	0.05	117.0	129.0	0.007	120.0	136.0	0.006
150	0.1	116.0	127.0	0.010	118.0	132.0	0.009
150	0.2	114.0	123.0	0.015	117.0	130.0	0.014
150	0.4	110.0	115.0	0.022	113.0	120.0	0.021
200	0.025	126.0	152.0	0.004	131.0	163.0	0.003
200	0.05	126.0	150.0	0.006	130.0	159.0	0.006
200	0.1	125.0	148.0	0.010	128.0	155.0	0.009
200	0.2	123.0	144.0	0.015	127.0	153.0	0.013
200	0.4	120.0	136.0	0.020	123.0	144.0	0.019
250	0.025	134.0	170.0	0.004	138.0	181.0	0.003
250	0.05	133.0	168.0	0.006	137.0	179.0	0.005
250	0.1	131.0	163.0	0.009	136.0	174.0	0.009
250	0.2	130.0	161.0	0.014	134.0	171.0	0.013
250	0.4	126.0	151.0	0.018	131.0	163.0	0.017
300	0.025	140.0	187.0	0.003	145.0	198.0	0.003
300	0.05	139.0	184.0	0.006	143.0	195.0	0.005
300	0.1	138.0	180.0	0.009	142.0	191.0	0.008
300	0.2	137.0	177.0	0.014	141.0	188.0	0.013
300	0.4	133.0	167.0	0.016	136.0	175.0	0.015

Although the void ratio or the sample density is little modified under the static conditions of consolidation, at low pressures, this effect was taken into account in this research. In fact, the software implemented in the equipment evaluates the G-module from the conditions of the specimens at the end of the consolidation phase and obviously using equation (3).

The results obtained make it possible to evaluate the effect of factors such as angular strain, effective consolidation pressure and relative density in the determination of the shear modulus through the execution of the resonant-column test.

4.1 Shear modulus versus angular strain

In general, the angular strain experienced by the material increases as the level of torsional excitation increases. Fig. 4 shows this fact; however, only the results corresponding to D_r = 20% are included herein. The shear strain in Fig. 4 and 5 is the average shear strain (γ_m), obtained as $2^*\gamma_{max}/3$, where γ_{max} is the maximum shear strain measured by the accelerometer.

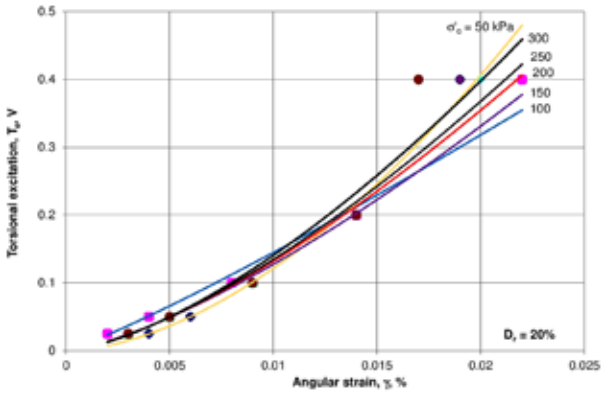

Figure 4. Typical variation trend of the angular strain as a function of the torsional excitation level, for D_r = 20%.

Fig. 6 shows the variation trends of the shear modulus as a function of the angular strains for effective consolidation pressures varying from 50 to 300 kPa and a relative density of 20%. It can be observed that in the range of small deformations (0.002–0.023%) the degradation of the shear modulus (or an increase of the inverse value of G) can be approximated as a linear function of the angular strain. This linear-type degradation recurs within the range of relative densities and effective consolidation pressures studied herein.

As these variation trends are similar, only the graphics corresponding to the relative densities equal to 20% have been included.

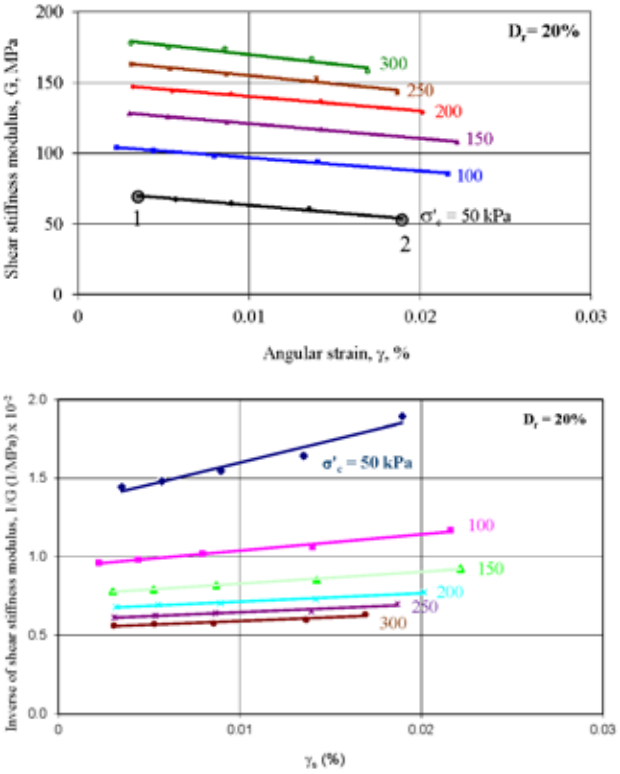

Figure 5. Typical variation trends of the shear modulus G, and its inverse 1/G as a function of the angular strain for different effective consolidation pressures and relative densities of 20%.

The degradation of the shear modulus (or the inverse of G) as a function of the angular strain has low values and reaches a maximum of 24% when the relative density is equal to 20%, the effective consolidation pressure amounts to 50 kPa and the angular strain increases from 0.0035% to 0.019% (large dots 1 and 2, Fig. 5).

The simplest mathematical model used to simulate the degradation of the shear modulus G as the strain, γ, increases is the one suggested by Hardin and Drnevich (1972) [39].

$$\frac{1}{G} = \frac{1}{G_o}\left(1 + \frac{\gamma}{\gamma_{ref}}\right) \qquad (12)$$

where G_o and γ_{ref} are the two parameters of the model.

In order to find values of G_o and γ_{ref} of the Hardin and Drnevich model that can contribute to better analyse the results of the investigation, a diagram of 1/G versus γ has been plotted and the best fit for straight lines was obtained. The resulting G_o and γ_{ref} values are given in Table 4.

Fig. 6 represents the relationship between shear modulus (G_o) and the void ratio ($\underline{e}$); in this case the void ratio is denoted by $\underline{e}$ to distinguish it from number e, the base of natural logarithms.

Table 4. Values of G_o and γ_{ref} that best fit the test results.

Value of G_o (MPa)						
D_r	Consolidation pressure σ'_c (kPa)					
	50	100	150	200	250	300
20	75.8	107.5	133.3	151.5	166.7	185.2
40	78.1	116.3	140.9	161.3	178.6	192.3
60	78.7	109.9	137.0	158.7	175.4	192.3
80	80.0	119.1	144.9	166.7	185.2	204.1

Value of γ_{ref} (%)						
D_r	Consolidation pressure σ'_c (kPa)					
	50	100	150	200	250	300
20	0.045	0.092	0.100	0.124	0.122	0.118
40	0.068	0.103	0.114	0.124	0.114	0.147
60	0.062	0.104	0.124	0.141	0.118	0.122
80	0.060	0.085	0.106	0.124	0.130	0.107

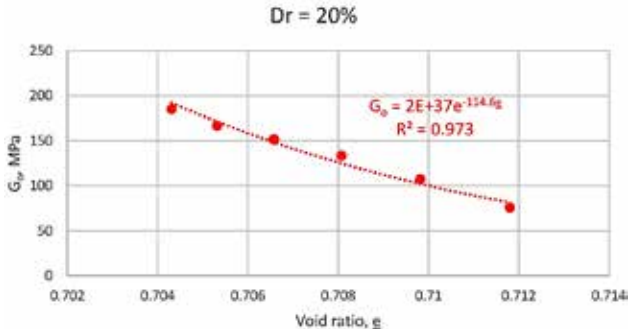

Figure 6. Value of shear modulus G_o vs void ratio (e).

As we can see in Table 4, the fact that G_o is sometimes even larger in samples with D_r = 40% than in samples with D_r = 60% is due to the narrow range of variation coupled with the unavoidable experimental scatter of results. The low sensitivity of G_o can be attributed to the nature of the sand, made of hard quartz grains (rounded and very uniform in size), which implies only little variation between the maximum and minimum void ratios.

4.2 Increase of G_o with σ'_c

The values of the shear modulus for small strains, G_o, obtained as indicated in the previous paragraph, are given in Table 4. It is clear that for each value of the relative density, the value of G_o increases as the consolidation pressure increases. See Fig. 7. Usually, the relation among these values (G_o and σ'_c) is thought to be of the type.

$$G_o = K\left(\frac{\sigma'_c}{p_o}\right)^N \cdot p_o \qquad (13)$$

where K is a "modulus number", N is an "exponent number" and p_o is the value of a standard reference pressure. For this particular investigation a value of p_o = 98.1 kPa is used.

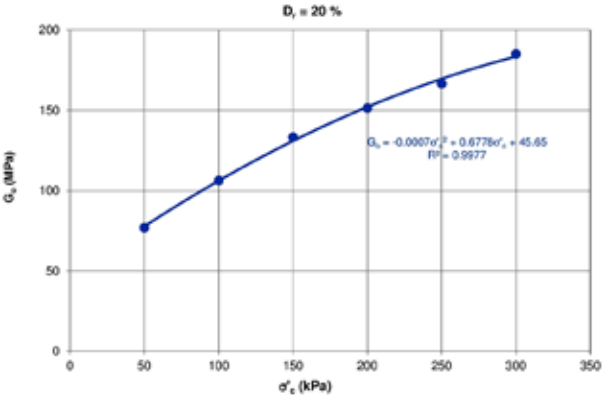

Figure 7. Values of G_o and σ'_c for D_r = 20%.

In order to investigate whether the expression (13) is applicable to this particular case, values of G were plotted versus the corresponding values of σ'_c on a log-log diagram. Fig. 8 is the plot that corresponds to D_r = 20%.

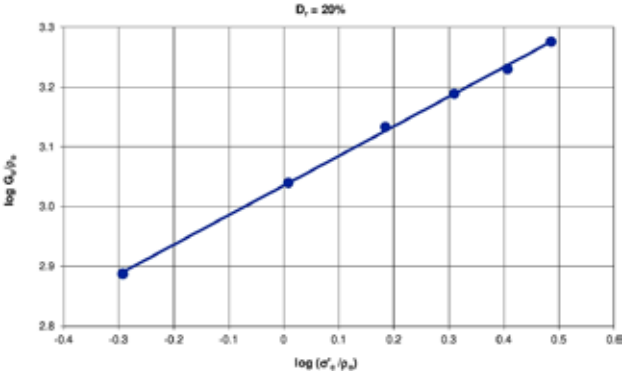

Figure 8. Double log plot of G_o and σ'_c data for D_r = 20%.

From this type of plot the model parameters can be automatically obtained from the data fit, made by minimizing the sum of the squares of the deviations of the test results that correspond to each relative density.

If the results of this research are compared to those recently obtained by Senetakis and Madhusudhan (2015) [36], Fig. 9 shows that even though the particle

Table 5. Automatically adjusted values of the dimensionless model parameters K and N.

Relative density	K	N
20 %	1084	0.495
40 %	1143	0.501
60 %	1122	0.502
80 %	1175	0.517

size differs roughly over an order of magnitude, the trend of the variation of G_o with σ'_c for the Ottawa sand coincides with that of specimen 6-2 tested by Senetakis.

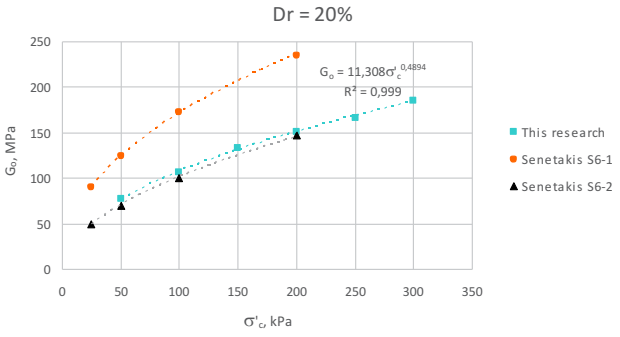

Figure 9. Values of G_o and σ'_c for D_r = 20%.

N tends to decrease slightly when the void ratio increases; it could even be suggested that N remains at a constant value of 0.50. This behaviour is different to the results obtained by Gu *et al* (2013) [27] using Toyoura sand, for which N tends to increase slightly with the void ratio. In reality, when the variation range is very narrow, some sands will show a tendency to increase N with an increase of the void ratio and in some others N will decrease slightly, as in Ottawa Sand.

4.3 Increase of γ_{ref} with σ'_c

From the values of γ_{ref} in Table 4 it seems that this parameter could be considered to be a constant but only for consolidation pressures above 200 kPa; for lower values of the consolidation pressure, the value of γ_{ref} decreases and it can no longer be considered as a constant in an hypothetical mathematical model.

A better option, which would account for the effect of large G degradation rates for lower values of the consolidation pressure, could be based on considering γ_{ref} as a variable that depends on the consolidation pressure.

It seems appropriate to assume that the degradation of the modulus G, when the angular deformation increases, should be mainly conditioned by the ratio

$$S = \frac{\tau_{\gamma\,max}}{\tau_f} \qquad (14)$$

Being $\tau_{\gamma\,max}$ the 'maximum shear stress applied' and τ_f the shear strength of the sand.

The value of $\tau_{\gamma\,max}$ can be approximated by

$$\tau_{\gamma\,max} = G\,\gamma_{max}$$

and τ_f can be estimated by

$$\tau_f \cong \sigma'_c \cdot \mathrm{tg}\,\phi$$

With these considerations, the following degradation equation can be proposed:

$$G = G_o\ (1 - A\,\frac{G\,\gamma}{\sigma_c'}) \qquad (15)$$

where A = dimensionless constant that would mainly depend on the shear strength of the tested sand, τ_f.

The value of γ_{ref} would then be given by the following expression:

$$\gamma_{ref} = \frac{\sigma_c'}{G_o \cdot A} \qquad (16)$$

Furthermore, it is known that G_o increases with the square root of σ'_c and, as a consequence, a value of γ_{ref} increasing with the square root of σ'_c should be expected.

For this reason, a value of γ_{ref} can be found to reasonably fit the data with an expression involving $(\sigma'_c/p_0)^{0.5}$. The best fit is given in Fig. 10. As we can see, the relative density also has an effect on γ_{ref}, but it is not easy to draw a clear figure showing the effect of the relative density at present.

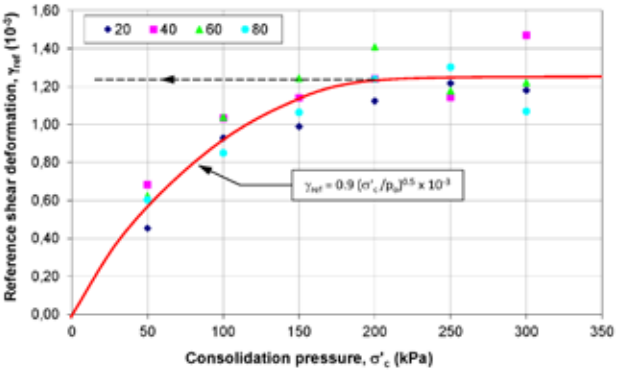

Figure 10. Reference values of the shear deformation.

This should be valid for values of γ with the interval

$$2 \times 10^{-5} < \gamma < 23 \times 10^{-5}$$

and for the range of densities of this particular investigation and for consolidation pressures lower than 200 kPa.

4.4 Influence of void ratio on the shear modulus

Four nominal values of the relative densities are used to prepare the samples for testing. These are relatively precise data, since the volume of the sample and the associated mass are known with a margin of error of about 0.1%.

During the process of consolidation some reduction in the volume takes place that increases the relative density. This change of relative density has been investigated by running an oedometer test on a sample prepared with an initial relative density of 20%. The results are given in Fig. 11.

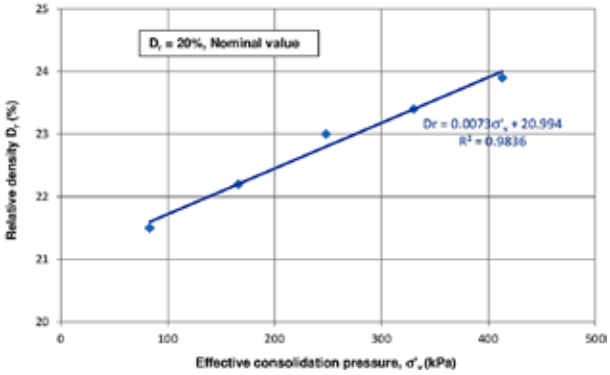

Figure 11. Increase of relative density. Oedometer test.

In resonant-column tests the consolidation pressure is applied in three directions and, as a consequence, changes in the relative density should be expected to be higher than the ones taking place in the oedometer tests, where the consolidation pressure σ'_c is only applied directly in the vertical direction. The theoretical relation of the volume changes between one-dimensional and three-dimensional consolidation is $R = 3/(1+2\,k_o)$. For this particular case and assuming an approximate value of $k_o = 0.5$, a factor $R = 1.5$ is obtained.

The real relative densities of the samples after consolidation are greater than the nominal values used in this investigation. Now, in order to better approach the effect of specimen densities, somewhat larger values of the relative densities are used.

It is known that the void ratio is a better parameter to analyze the dynamic moduli of sands than the relative density. Two different sands that have similar void ratios could have quite similar shear moduli even if their relative densities were quite different. In the same manner, two sands with equal relative densities could have quite different shear moduli.

Since the void ratio is a better parameter, the values of the relative density have been translated into void-ratio values. For this particular sand, with values of $e_{max} = 0.754$ and $e_{min.} = 0.554$, the following relation exists between the relative densities and the void ratios:

$$D_r = \frac{e_{max} - e}{e_{max} - e_{min}} = \frac{0.754 - e}{0.754 - 0.554} = \frac{0.754 - e}{0.20} \qquad (17)$$

Based on this expression and taking into consideration the small increase of the relative densities during the consolidation process of the samples, the values of the void ratios to represent the expected value of each test are given in Table 6.

Table 6. Values of the void ratio for each test series.

Relative density D_r Normal value	Relative density D_r^* Expected after consolidation	Void ratio e during the test
20%	22%	0.71
40%	42%	0.67
60%	62%	0.63
80%	82%	0.59

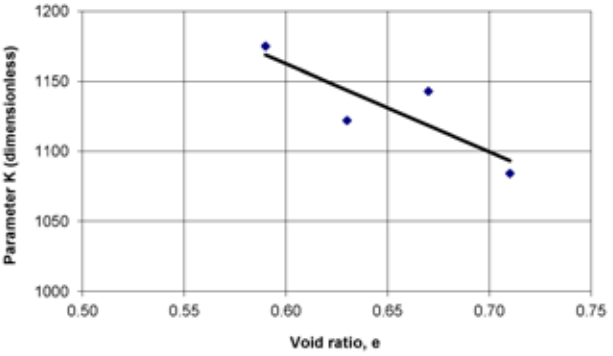

Figure 12. Value of the model modulus number K vs. void ratio, e.

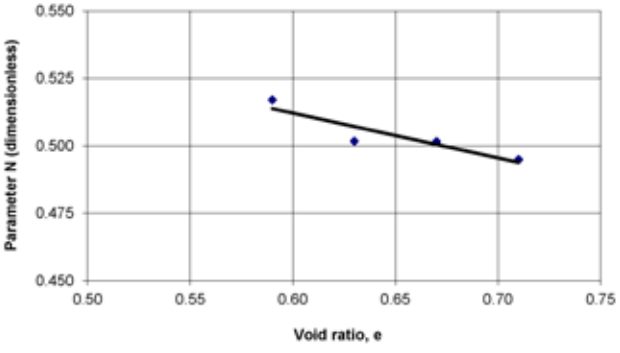

Figure 13. Value of the model modulus exponent, N, vs. void ratio, e.

Variations of the parameters K and N obtained in previous paragraphs are now plotted in Fig. 12 and Fig. 13 as a function of the void ratio.

5 DISCUSSION

The interpretation of the data obtained by testing the 120 samples of 20–40 Ottawa sand leads to proposing the following value for the shear modulus:

$$G = \left(1+\frac{\gamma}{\gamma_{ref}}\right)^{-1} \cdot k \left(\frac{\sigma'_c}{p_o}\right)^{N} \cdot p_o \qquad (18)$$

where the main variables are:

γ = angular deformation.
σ'_c = consolidation pressure

In this expression, p_o is a reference pressure with the value, p_o = 98.1 kPa = 1 kp/cm^2.

The values of the dimensionless parameters are:

$$\gamma_{ref} = 0.9 \left(\frac{\sigma'_c}{p_o}\right)^{0,5} | \times 10^{-3} \leq 1.26 \times 10^{-3} \qquad (19)$$

k = 1000 (1.54 - 0.63e)
N = 0.5 (1.22 - 0.33e)

where e = void ratio.

Senetakis and Madhusudhan (2015) [36] remarked that when relating G_o with p' through a potential function, the exponent n_G decreases slightly as the relative density increases. This research has also found that G_o can be related to σ'_c through potential functions with an exponent N that increases slightly with relative density. As mentioned, the trend in the variation of N would not necessarily be the same, as many factors are different in the various research tests. Moreover, the ranges of variation for the exponent N are very narrow. This model is considered to be valid for the range of consolidation pressures, the angular deformation and the void ratio covered for this investigation.

Those ranges are:

σ'_c : 50 to 300 kPa
γ_{max} : 2 × 10^{-5} to 23 × 10^{-5}
e: 0.59 to 0.71

Most authors, among them Richart *et al.* (1970) [11], Prakash (1981) [40], Das (1983) [41], accept that round grained sands, tested in the resonant column device in dry conditions, have a shear modulus that can be estimated using the following expression:

$$G = 697 \frac{(2.17-e)^2}{1+e} \cdot p_o \cdot \left(\frac{\sigma'_c}{p_o}\right)^{0.5} \qquad (20)$$

where e = void ratio; p_o = reference pressure (0.1 MPa) and σ'_c = consolidation pressure.

This quite famous correlation was first established by Hardin and Richart (1963) [12] and does apply to dry sands tested under resonant-column conditions with shear deformations of the order of $\gamma_{max} = 10^{-3}$ rd.

For the central value of the void ratio of this investigation, e = 0.65 and σ'_c = 150 kPa, the above expression yields the following results:

$$G = 1.207 \cdot p_o = 118 \text{ MPa}$$

From the results of this investigation it can be obtained, for the same conditions (σ'_c = 150 kPa, e = 0.65).

$$G = \left(1+\frac{\gamma}{\gamma_{ref}}\right)^{-1} \times 137 \text{ MPa} \qquad (21)$$

$$\gamma_{ref} = 1.11 \times 10^{-3}$$

It can be seen that both results would coincide if the value of γ is:

$$\gamma = 1.8 \times 10^{-4}$$

It can be concluded that the approach given in this paper agrees quite closely, at least for the central value of G, with the established practice.

This investigation deals with saturated sands, whereas the one used to make the comparison, Hardin and Richart (1963) [15], deals with dry soil. This may lead us to conclude that the effect of saturation on the value of the shear modulus could be quite small, practically negligible.

But there is one difference in respect to the influence of the void ratio on the value of the shear modulus. According to the old reference considered in this discussion [7], changing the void ratio from e = 0.71 to e = 0.59 (extreme values in this research) increases the shear modulus by 26%, irrespective of the other test variables. However, according to this investigation, the change in the modulus depends on the consolidation pressure, but it is, in any case, less than 16%.

This discrepancy could be considered as an artifact of the unavoidable imprecision of laboratory tests or it could be a real difference in behavior due to the effect of the sample saturation.

6 CONCLUSIONS

A total of 120 saturated specimens of Ottawa sand were tested in a resonant-column apparatus under angular strains (γ) of 0.002 to 0.023%, relative densities ranging from 20 to 80% and effective consolidation pressures (σ'_c) between 50 and 300 kPa. The obtained shear modulus (*G*) was related to the other intervening parameters. The main conclusions derived are as follows:

1. Relative density is the factor with the least influence on the obtained shear modulus. Following in importance are the angular strains.
2. The greatest influence in the value of the shear modulus is the effective consolidation pressure.
3. A simple empirical expression is proposed for G as a function of γ and σ'_c, for the range of γ tested.
4. For the same γ and Dr, the variation trend of G, as a function of σ'_c, can be fit to a potential function with a correlation coefficient practically equal to unity.
5. A simple expression (18) is proposed for *G*, also taking into account the void ratio (*e*) values. This research has explored a somewhat narrow range of *e* and therefore this proposal could be less precise than those made to consider other effects.
6. Although the material used was saturated Ottawa sand, the model defined in this paper might be valid in the case of other uniform granular soils with fine to medium rounded grains and quartz origin.

REFERENCES

[1] Ishimato, M., Iida, K. 1937. Determination of elastic constants of soils by means of vibration methods. Part 2. Modulus of rigidity and Poisson's ratio. Bulletin of the Earthquake Research Institute, Tokyo Imperial University, 15, 67-85.

[2] Iida, K. 1938. The Velocity of Elastic Waves in Sand. Bulletin of the Earthquake Research Institute, Tokyo Imperial University, 16, 131-144.

[3] Iida, K. 1940. On the Elastic Properties of Soil Particularly in Relation to its Water Contents. Bulletin of the Earthquake Research Institute, Tokyo Imperial University, 18, 675-690.

[4] Bishop, K.E. 1959. Forced torsional vibration of system with distributed mass and internal and external damping. Transactions of the ASME, 8-12.

[5] Wilson, S.D., Dietrich, R.J. 1960. Effect of consolidation pressure on elastic and strength properties of clay. Proceedings of the Research Conference on Shear Strength of Cohesive Soils, ASCE, Boulder, Colorado, pp. 419-435.

[6] Hall, J.R., Richard, F.E. 1963. Discussion of elastic wave energy in granular soils. ASCE, Journal of the Soil Mechanics and Foundations Division 89, 6, 27-56.

[7] Drnevich, V.P., Hall, J.R., Richart, F.E., University of Michigan, U.S. Army Engineer, Waterways Experiment Station. 1966. Large Amplitude Vibration Effects on the Shear Modulus of Sand. Vicksburg, Miss: Waterways Experiment Station. USA.

[8] Drnevich, V.P., Hall, J.R., Richart, F.E. 1967. Effect of amplitude of vibration on the shear modulus of sand. Proceedings of the International Symposium on Wave Propagation and Dynamic Properties of Earth Materials, Albuquerque, USA, pp 189-199.

[9] Drnevich, V.P., Hardin, B.O., Shippy, D.J. 1978. Modulus and damping of soils by the resonant-column method. Dynamic Geotechnical Testing, American Society for Testing and Materials 91-125.DOI: http://dx.doi.org/10.1520/STP35673S

[10] Menq, F. 2003. Dynamic properties of sandy and gravelly soils. Doctor of Philosophy Dissertation, University of Texas, Austin.

[11] Clayton, C.R.I., Priest, J.A., Bui, M., Zervos, A., Kim, S. G. 2009. The Stokoe resonant column apparatus: effects of stiffness, mass and specimen fixity. Geotechnique 59, 5, 429-437. DOI: http://dx.doi.org/10.1680/geot.2007.00096

[12] Clayton, C.R.I. 2011. Stiffness at small strain: research and practice. Geotechnique 61, 1, 5-37. DOI: http://dx.doi.org/10.1680/geot.2011.61.1.5

[13] Al-Sanad, H., Aggour, M.S. 1984. Dynamic soil properties from sinusoidal and random vibrations. Proceeding, 8th World Conference on Earthquake Engineering 3, San Francisco, pp. 15-22.

[14] Tawfiq, K.S., Aggour, M.S., Al-Samad, H.A. 1988. Dynamic properties of cohesive soils from impulse testing. Proceedings, 9th World Conference on Earthquake Engineering 3, Tokyo, pp. 11-16.

[15] Hardin, B.O., Richart, F.E. 1963. Elastic wave velocities in granular soils. ASCE, Journal of the Soil Mechanics and Foundations Division 98, 1, 33-65.

[16] Hardin, B.O. 1965. The nature of damping in sands. ASCE, Journal of the Soil Mechanics and Foundations Division 91, 1, 63-97.

[17] Richart, F.E., Hall, J.R., Woods, R.D. 1970. Vibration of Soils and Foundations. Prentice Hall, Englewood Cliffs, New Jersey.

[18] Santamarina, J. C., Cascante, G. 1996. Stress anisotropy and wave propagation: a micromechanical view. Canadian geotechnical Journal 33, 770-782. DOI: 10.1139/t96-102-323

[19] Kuribayashi, E., Iwasaki, T., Tatsuoka, F. 1975. Effects of stress-strain conditions on dynamic properties of sands. Proceedings of the Japan Society of Civil Engineers 242, 105-114. DOI: http://

dx.doi.org/10.2208/jscej1969.1975.242_105
[20] Iwasaki, T., Tatsuoka, F., Takagi, Y. 1978. Shear moduli of sands under cyclic torsional shear loading. Soils and Foundations 18, 1, 39-56. DOI: http://dx.doi.org/10.3208/sandf1972.18.39
[21] Tatsuoka, F., Iwasaki, T., Yoshida, S., Fukushima, S., Sudo, H. 1979. Shear modulus and damping by drained tests on clean sand specimen reconstituted by various methods. Soils and Foundations 19, 1, 39-54. DOI: http://dx.doi.org/10.3208/sandf1972.19.39
[22] Alarcón-Guzmán, A., Chameau, J.L., Leonards, G.A., Frost, J.D. 1989. Shear modulus and cyclic undrained behavior of sands. Soils and Foundations 29, 4, 105-119.
[23] Saxena, S., Reddy, K. 1989. Dynamic moduli and Damping ratios for Monterrey No. 0 sand by resonant column test. Soils and Foundations 29, 2, 37-51. DOI: http://doi.org/10.3208/sandf1972.29.2_37
[24] Lo Presti, D.C.F., Jamiolkowski, M., Pallara, O., Cavallaro, A., Pedroni, S. 1997. Shear modulus and damping of soils. Géotechnique 37, 3, 603-617. DOI: http://dx.doi.org/10.1680/geot.1997.47.3.603
[25] Díaz-Rodríguez, J.A., López-Flores, L. 1999. A study of microstructure using resonant-column tests. Proceeding of the Second International Conference on Earthquake Geotechnical Engineering, Lisbon, Portugal, pp. 89-94.
[26] Wichtmann, T., Triantafyllidis, T. 2004. Influence of a cyclic and dynamic loading history on dynamic properties of dry sand, part I: Cyclic and dynamic torsional prestraining. Soil Dynamics and Earthquake Engineering 24, 127-147. DOI: http://dx.doi.org/10.1016/j.soildyn.2003.10.004
[27] Gu, X.Q., Yang, J., Huang, M.S. 2013. Laboratory measurements of small strain properties of dry sands by bender element. Soils and Foundations, 53, 5, 735-745. DOI: http://dx.doi.org/10.1016/j.sandf.2013.08.011
[28] Chang, N.Y., Ko, H.Y., University of Colorado at Denver. Geotechnical Engineering Division. 1982. Effect of Grain Size Distribution on Dynamic Properties and Liquefaction Potential of Granular Soils. University of Colorado, Department of Civil and Urban Engineering, Geotechnical Engineering Division. USA.
[29] Koono, T., Suzuki, Y., Tateishi, A., Ishihara, K., Akino, K., Satsuki, I. 1993. Gravelly soil properties by field and laboratory tests. Proceedings of the 3rd International Conference on Case Histories in Geotechnical Engineering, St Louis, Missouri, 1, pp. 575-594.
[30] Wichtmann, T., Triantafyllidis, T. 2009. Influence of the Grain-Size Distribution Curve of Quartz Sand on the Small Strain Shear Modulus Gmax. ASCE, Journal of Geotechnical and Geoenvironmental Engineering 135, 10, 1404-1418. DOI: http://dx.doi.org/10.1061/(ASCE)GT.1943-5606.0000096
[31] Wichtmann, T., Triantafyllidis, T. 2013. Effect of Uniformity Coefficient on G/Gmax and Damping Ratio of Uniform to Well-Graded Quartz Sands. Journal of Geotechnical and ASCE, Geoenvironmental Engineering 139, 1, 59-72. DOI: http://dx.doi.org/10.1061/(ASCE)GT.1943-5606.0000735
[32] Wichtmann, T., Triantafyllidis, T. 2014. Stiffness and Damping of Clean Quartz Sand with Various Grain-Size Distribution Curves. ASCE, Journal of Geotechnical and Geoenvironmental Engineering, Technical Note 140, 1-4. DOI: http://dx.doi.org/10.1061/(ASCE)GT.1943-5606.0000977
[33] Martínez, E. 2012. Influencia de la densidad relativa, índice de poros, presión de consolidación y amplitud de excitación en los parámetros dinámicos de una arena saturada (Máster tesis). Universidad Complutense de Madrid.
[34] Senetakis, K., Anastasiadis, A., Pitilakis, K. 2012. The Small-Strain Shear Modulus and Damping Ratio of Quartz and Volcanic Sands. Geotechnical Testing Journal 35, 6, 964-980. DOI: http://dx.doi.org/10.1520/GTJ20120073
[35] Yang, J., Gu, X.Q. 2013. Shear stiffness of granular material at small strains: Does it depend on grain size. Géotechnique 63, 2, 165-179. DOI: http://dx.doi.org/10.1680/geot.11.P.083
[36] Senetakis, K., Madhusudhan, B. N. 2015. Dynamics of potential fill–backfill material at very small strains. Soils and Foundations 55, 5, 1196-1210. DOI: http://dx.doi.org/10.1016/j.sandf.2015.09.019
[37] Payan, M., Khoshghalb, A., Senetakis, K., Khalili, N. 2016. Effect of particle shape and validity of Gmax models for sand: A critical review and a new expression. Computers and Geotechnics 72, 28-41. Dynamics of potential fill–backfill material at very small strains. DOI: http://dx.doi.org/10.1016/j.compgeo.2015.11.003
[38] Payan, M., Denetakis, K., Khoshghalb, A., Khalili, N. 2016. Influence of particle shape on small-strain damping ratio of dry sands. Géotechnique 66, 7, 610-616. DOI: http://dx.doi.org/10.1680/jgeot.15.T.035
[39] Hardin, B.O., Drnevich, V.P. 1972. Shear Modulus and Damping in Soils: Design Equations and Curves. ASCE, Journal of the Soil Mechanics and Foundations Division 98, 7, 667-692.
[40] Prakash, S. 1981. Soil Dynamics. McGraw-Hill Book Company. USA
[41] Das, B M. 1983. Fundamentals of Soil Dynamics. Elsevier Science Publishers. USA.

INŽENIRSKE LASTNOSTI TROPSKE GLINE IN BENTONITA MODIFICIRANIH Z ŽAGOVINO

Isaac I. Akinwumi *(vodilni avtor)*
Covenant University,
Department of Civil Engineering
Ota, Nigerija
E-pošta: isaac.akinwumi@covenantuniversity.edu.ng

University of the West of England,
Department of Architecture and the Built Environment
Bristol, Velika Britanija
E-pošta: isaac.akinwumi@uwe.ac.uk

Oluwapelumi O. Ojuri
Federal University of Technology Akure,
Department of Civil and Environmental Engineering
Nigerija
E-pošta: ooojuri@futa.edu.ng

Adebanji S. Ogbiye
Covenant University,
Department of Civil Engineering
Ota, Nigerija
E-pošta: ade.ogbiye@covenantuniversity.edu.ng

Colin A. Booth
University of the West of England,
Department of Architecture and the Built Environment
Bristol, Velika Britanija
E-pošta: colin.booth@uwe.ac.uk

Ključne besede

geotehnične lastnosti, hidravlične pregrade, odlagališča, konstrukcija, izboljšanje tal, trajnost.

Izvleček

Inženirji gradbeništva se običajno izogibajo uporabi ekspanzivnih zemljin kot gradbenih materialov, ker se z njimi običajno težko dela in lahko povzročijo porušitve konstrukcije. V predstavljenem delu je raziskovan vpliv uporabe žagovine v tropskih glinah in bentonitu na njihove geotehnične lastnosti, da bi ugotovili njihovo primernost za uporabo na odlagališčih odpadkov za učinkovito zadrževanje strupenih snovi. Z rentgensko difraktometrijo, rentgensko fluorescenčno spektroskopijo in skeniranjem z vrstičnim elektronskim mikroskopom smo določili mineraloško in kemično sestavo, ter mikrostrukturo gline in bentonita. Za določitev specifične gravitacije, Atterbergovih meja, zbitosti, enoosne tlačne trdnosti in prepustnosti gline in bentonita za različne dele žagovine so bile izvedene številne laboratorijske preiskave. Na splošno je povečanje vsebnosti žagovine povzročilo zmanjšanje njegove specifične gravitacije, največje suhe prostorninske teže in enoosne tlačne trdnosti, medtem ko je povečalo optimalno vlažnost in prepustnost tako modificirane gline in bentonita. Glina in bentonit imata dovolj nizko prepustnost, ki ustreza zahtevam hidravlične prevodnosti za uporabo kot glinene pregrade. Za ekonomski način modificiranja gline - s potencialom izboljšanja njene adsorbcijske lastnosti – je priporočen dodatek osmih odstotkov žagovine k glini s podobnimi lastnostmi kot v tej študiji. S tem se prepreči iztekanje strupenih snovi iz odlagališča in tako varovanje okolja in javnega zdravja.

ENGINEERING PROPERTIES OF TROPICAL CLAY AND BENTONITE MODIFIED WITH SAWDUST

Isaac I. Akinwumi *(corresponding author)*
Covenant University,
Department of Civil Engineering
Ota, Nigeria
E-mail: isaac.akinwumi@covenantuniversity.edu.ng

University of the West of England,
Department of Architecture and the Built Environment
Bristol, United Kingdom
E-mail: isaac.akinwumi@uwe.ac.uk

Oluwapelumi O. Ojuri
Federal University of Technology Akure,
Department of Civil and Environmental Engineering
Nigeria
E-mail: ooojuri@futa.edu.ng

Adebanji S. Ogbiye
Covenant University,
Department of Civil Engineering
Ota, Nigeria
E-mail: ade.ogbiye@covenantuniversity.edu.ng

Colin A. Booth
University of the West of England,
Department of Architecture and the Built Environment
Bristol, United Kingdom
E-mail: colin.booth@uwe.ac.uk

Keywords

geotechnical properties, hydraulic barrier, landfill, construction, soil improvement, sustainability

Abstract

Construction engineers typically avoid the use of expansive soils as construction materials because they are usually difficult to work on and can cause structural failure. This research work investigates how the application of sawdust to tropical clay and bentonite influences their geotechnical properties in order to determine their suitability for use as landfill-liner materials for the effective containment of toxic substances from landfills. X-ray diffractometry, X-ray fluorescence spectroscopy and scanning electron microscopy were used to determine the mineralogical composition, oxide composition and microstructure, respectively, of the clay and the bentonite. A series of laboratory tests were conducted to determine the specific gravity, Atterberg limits, compaction, unconfined compressive strength and permeability characteristics of the clay and the bentonite for varying proportions of sawdust application. Generally, increasing the percentage of sawdust caused a reduction in its specific gravity, maximum dry unit weight and unconfined compressive strength, while it caused an increase in the optimum moisture content and permeability of the modified clay and bentonite. The clay and bentonite both have a sufficiently low permeability that satisfies the hydraulic conductivity requirement for use as clay liners. Eight percent sawdust application to a clay having similar properties as that in this study is recommended as an economic way of modifying it – with the potential of improving its adsorbent property – for use in landfill-liner systems in order to prevent the toxic substances leaching from the landfills, thereby protecting the environment and public health.

1 INTRODUCTION

Globally, expansive soils have been identified as a cause of failure for many structures and the infrastructures built on them [1]. According to the Wyoming Office of Homeland Security [2], damage to infrastructure in the United States (US) caused by expansive soils is more than twice the sum of the damage that resulted from floods, earthquakes, tornadoes and hurricanes. The annual damage to structures (such as buildings, roads, bridges and pipelines) in the US alone is estimated at $2.3 billion [2].

Due to moisture-content changes, expansive soils swell or shrink [3] and, consequently, make the structures built on them unstable and susceptible to damage [4, 5]. Aside from being characterized by a large volume change, they also usually have a high moisture-holding capacity, low bearing capacity, low strength and low permeability [6]. Cracks develop when these soils are subjected to repeated dry-wet cycles [7]. Clay minerals, especially

the smectite group, are responsible for the expansive nature of this category of soils. Many constructors and geotechnical engineers try to avoid the use of expansive soils as construction materials or constructing on them. However, the depletion of suitable natural soils and land areas has made it sometimes unavoidable.

The stabilization or modification of expansive soils in order to make them suitable for construction purposes has attracted the attention of many researchers in recent decades. Some of the stabilizers or modifiers that have been investigated include: lime [8], fly ash [9], steel slag [10], coconut fibres [11], marble dust [12], polypropylene fibre [13], blast-furnace slag [14] and bio-enzymes [15]. However, some of these stabilizers are expensive, not locally available in some places and do not suit some engineering applications.

Clays are commonly used to contain the wastes that are disposed in landfills, because of their hydraulic property [16]. They are normally used for lining the base, sides and engineered capping of a landfill [17]. Clay liners function to prevent the migration of leachates from landfills and to prevent groundwater from gaining access to these landfills [17]. The lining and capping can be provided using either natural or artificial materials, or a combination of these.

In this study a series of laboratory experiments was used to investigate the effect of modifying a tropical clay and bentonite using sawdust on their geotechnical properties in order to determine their suitability for use as landfill-liner materials. Bulut and Tez [18] found that sawdust is a good adsorbent for heavy metals. Therefore, its use along with clays in a landfill-liner system has the potential to provide a better retention of toxic substances (such as lead and cadmium) by landfills in order to protect public health via the prevention or minimization of groundwater pollution. Sawdust, a waste from wood processing, has the potential to provide a cheap and locally available choice of material for modifying the clay for use as a landfill-lining system by introducing an organic substance that can provide a better retention of the toxic leachates from landfills. In this way, protecting public health and the environment, while minimizing the environmental nuisance associated with the improper disposal of sawdust.

2 MATERIALS AND METHODS

2.1 Materials

The clay soil used was collected, as a large mass clog of clay, from a borrow pit behind Covenant University, Ota, Nigeria. It was then air-dried in the laboratory and pulverized, with all its particles passing through a sieve with 75-μm openings (Fig. 1). The bentonite used was procured from the market in powdered form. Before use, it was oven-dried for 3 hours to ensure that there is no moisture within it. All its particles were found to be clay-size. Sawdust of *Combretodendron Macrocarpum* was obtained from a wood sawmill at Ota, Ogun State, Nigeria and used to modify the clay and bentonite samples. This species of sawdust was so selected because it is reportedly found throughout tropical West Africa [19, 20] and can consequently be cheaply sourced. The sawdust was washed with distilled (de-ionized) water to remove the dust and soluble impurities, and then dried at room temperature. Only the fraction passing through 425-μm sieve openings was used in order to meet the requirement for the liquid and plastic limits tests. This procedure for preparing the sawdust is in accordance with that used by Bulut and Tez [18] and Gupta and Babu [21]. The sawdust was applied to the samples in the following proportions: 0, 2, 4, 6 and 8%, by dry weight of the clay or bentonite. The maximum percentage of sawdust used to modify the clay and bentonite was selected such that the permeability of the modified materials satisfies the permeability requirement ($\leq 1 \times 10^{-7}$ cm/s), which is the most generally acceptable criterion that materials to be used as landfill liners should satisfy [17].

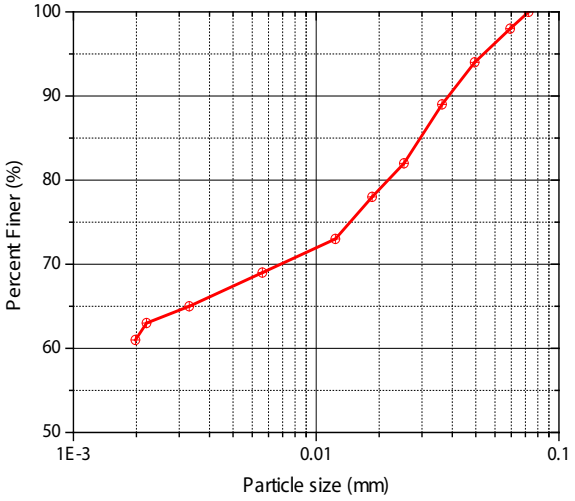

Figure 1. Particle size distribution of the clay.

Representative samples of the clay and bentonite were collected randomly from the thoroughly mixed bentonite and pulverised soil samples, in order to ensure homogeneity of the sample for the chemical and mineralogical composition and microstructural analysis. The

microstructures of the clay and bentonite were obtained using a scanning electron microscope (SEM), while their chemical and mineralogical compositions were determined using an X-ray fluorescence spectrometer and an X-ray diffractometer, respectively.

2.2. Methods

Geotechnical characterization tests were performed in accordance with British Standard Institution (BSI) procedures. The natural or in-situ moisture content of the clay soil was determined using a laboratory oven-drying method [22] (Clause 3.2). The particle size distribution of the soil was determined by carrying out sieve and hydrometer analyses. The sieve analysis was conducted on the clay soil using the wet-sieving method [22] (Clause 9.2). The hydrometer analysis was conducted on the fine-grained fraction of the soil in accordance with BSI [22] (Clause 9.5). The plasticity of the clay and bentonite were determined from laboratory tests for the determination of the liquid and plastic limits. The liquid limit of the samples was determined using the Casagrande apparatus method, in accordance with BSI [22] (Clause 4.5). The procedure for the determination of the plastic limits of the samples was in accordance with BSI [20] (Clause 5.3), while the plasticity indices were derived in accordance with BSI [22] (Clause 5.4). The specific gravities of the samples were determined using the pycnometer method, in accordance with the procedures outlined by BSI [22] (Clause 8.3). The compaction characteristics of the samples were determined using the procedures outlined in BSI [23] (Clause 3.3). The procedure followed for the determination of the unconfined compressive strength was that for the load-frame method and is in accordance with the procedure outlined in BSI [24] (Clause 7.2). A falling-head permeameter was used to determine the permeability of the clay and bentonite in accordance with Head [25]. The geotechnical properties were determined (at least) in triplicate in order to ensure the scientific robustness of the results, which are presented as the mean and standard deviation.

3 RESULTS AND DISCUSSION

3.1. Chemical and mineralogical composition

The chemical properties of soils are important and can provide an insight to their behavior or reaction with other materials. Fig. 2 presents the oxide composition of the clay and bentonite samples. Fig. 2 shows that silica, alumina and iron (III) oxide are the predominant oxides

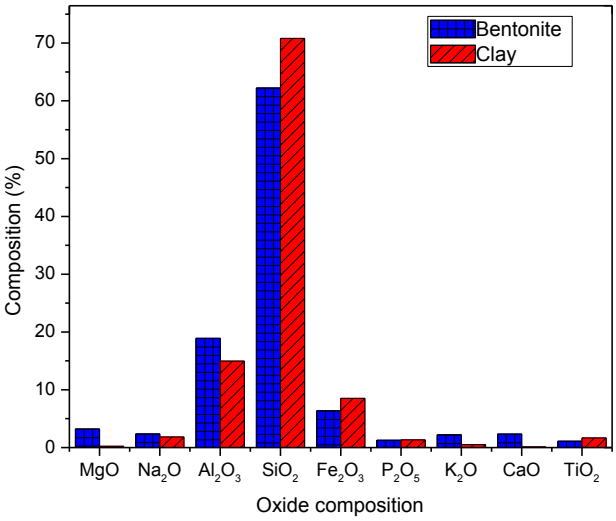

Figure 2. Oxides of the clay and bentonite.

of the clay and bentonite. Silica is the main constituent oxide – having more than 50% of the oxides. The clay was obtained from a white rock-like mass having small embedment, whose colours are: brown (7.5YR 4/4), yellow (10YR 8/8) and purple (10P 5/8), in accordance with the Munsell colour chart. Its brown and yellow colour is believed to be an indication of iron oxide. The bentonite is fine and has a grey coloration (2.5GY 8.5/2).

The mineralogical compositions of the clay and the bentonite indicate that the clay is composed of kaolinite and quartz, while the bentonite is predominantly composed of montmorillonite. The white coloration of the clay results from the presence of kaolinite.

3.2. Modification of Clay and Bentonite with Sawdust

The geotechnical properties of the clay and bentonite are presented in Tables 1 and 2. According to the Unified Soil Classification System (USCS), the clay is classified as CH – clay of high plasticity. It has a natural moisture content of 10.1, a specific gravity of 2.64 and a plasticity index of 27%. The bentonite has an extremely high plasticity (plasticity index of 56.4%) and its specific gravity is 2.49. When the dry powdered bentonite comes in contact with water, it forms a gel-like slurry – making it difficult for water to flow through it.

The clay-size fraction of the clay makes up 61% of its particles (Fig. 1) and as such influences the overall engineering properties of the soil [26].

Table 1. Geotechnical properties of the natural clay.

Properties		Natural soil *Mean (Standard deviation)*
Classification	Unified Soil Classification System	CH - Clay
Physical	Colour	Pinkish White
	Specific Gravity	2.64 (0.052)
	Liquid Limit (%)	61.5 (0.398)
	Plastic Limit (%)	34.5 (0.657)
	Plasticity Index (%)	27.0 (0.768)
	Maximum Dry Unit weight (kN/m^3)	15.5 (0.208)
	Optimum Moisture Content (%)	19.7 (0.252)
	Coefficient of Permeability (cm/s)	0.189 x 10^{-7} (0.00339 x 10^{-7})
Strength	Unconfined Compressive Strength (kN/m^2)	1148 (5.923)

Table 2. Geotechnical properties of the bentonite.

Properties		Bentonite *Mean (Standard deviation)*
Physical	Colour	Grey
	Specific Gravity	2.49 (0.072)
	Liquid Limit (%)	166.5 (1.354)
	Plastic Limit (%)	110.1 (1.099)
	Plasticity Index (%)	56.4 (1.230)
	Maximum Dry Unit weight (kN/m^3)	12.9 (0.000)
	Optimum Moisture Content (%)	21.1 (0.231)
	Coefficient of Permeability (cm/s)	0.058 x 10^{-7} (0.000968 x 10^{-7})
Strength	Unconfined Compressive Strength (kN/m^2)	347.7 (2.082)

3.2.1. Specific Gravity

The variation of the specific gravities of the clay and bentonite with sawdust are shown in Fig. 3. The specific gravities of the clay and bentonite decreased with an increasing percentage of sawdust in the soil.

The sawust used has a specific gravity of 1.16. Consequently, the specific gravities of the sawdust-treated clay and sawdust-treated bentonite did not deviate from the expectation that partial replacement of the clay (having a specific gravity of 2.64) or bentonite (having a specific gravity of 2.49) with sawdust would cause a reduction in the specific gravity of the modified samples. A study by Tran [27], on how the application of sawdust to an agricultural soil influences its corn yield, reported a reduction in the bulk density (which is related to the specific gravity) of the sawdust-modified soil with increasing sawdust application. This agrees with this study. The replacement of some of the clay and bentonite with sawdust might also have generated increased void spaces within the modified samples.

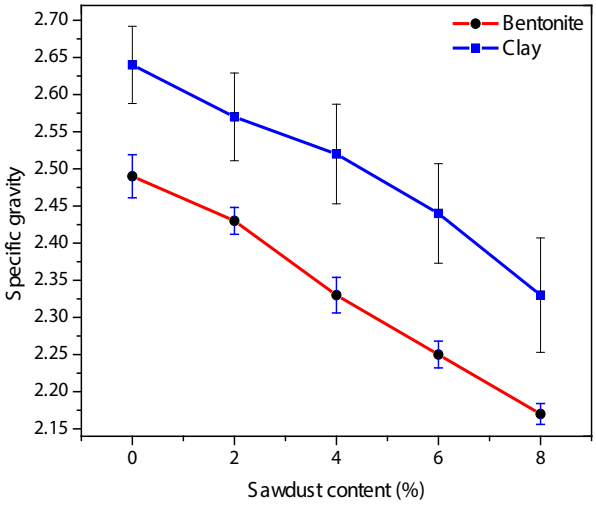

Figure 3. Variation of specific gravities of the clay and bentonite with sawdust.

3.2.2. Atterberg limits

The Atterberg limits of the clay varied with the proportion of sawdust added to it, as illustrated in Fig. 4. The liquid limit and plastic limit of the soil decreased with increasing sawdust content. The mean plasticity indices of the clay and that of its modification with 2% sawdust was comparatively the same, while a subsequent increase in the sawdust content resulted in a decrease in the plasticity index of the clay. The plasticity indices of soils give a measure of their plasticity [26]. Therefore, it can be said that the plasticity of the clay decreased with an increasing percentage of sawdust in the mixture.

When the clay minerals in the soils interact with water, a thin layer of water called the diffuse double layer gets bonded to their surfaces [26, 28, 29], which influences their plasticity. The application of sawdust to the clay makes the sawdust cling around its clay minerals and absorbs water from them – thereby reducing their moisture-holding capacity and their ability to freely interact with themselves and become aggregated. Consequently,

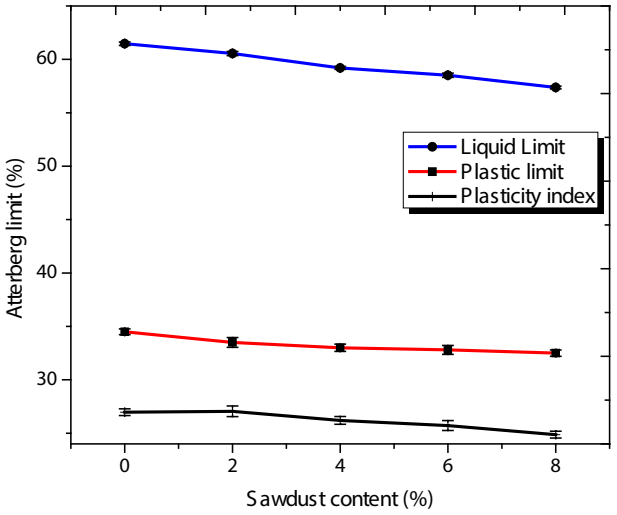

Figure 4. Variation of Atterberg limits of the clay with sawdust.

the plasticity of the clay decreases as its sawdust content increases. This makes the treated clay more workable. This finding reiterates the statement of Abd El Halim and El Baroudy [30] that sawdust can be used to reduce the plasticity of expansive soils.

The variation of the liquid and plastic limits and the plasticity index of the bentonite with sawdust is presented in Fig. 5. The liquid and plastic limits decreased, while the plasticity index of the bentonite surprisingly slightly increased as its sawdust content increased. This may, however, be due to the extremely high plasticity of the bentonite.

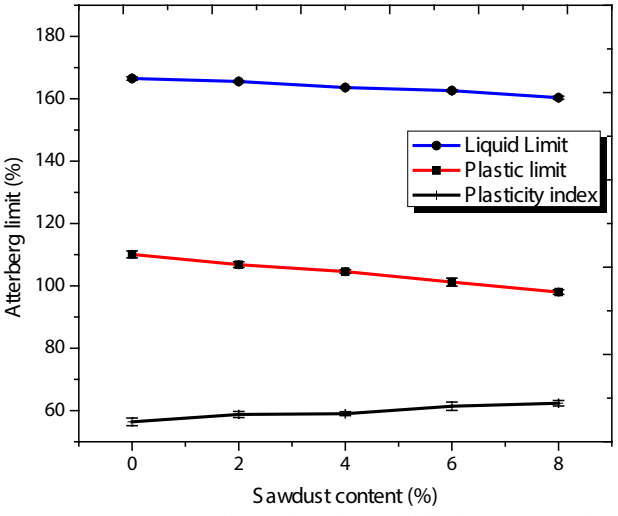

Figure 5. Variation of Atterberg limits of the bentonite with sawdust.

Though sawdust is non-plastic, it is not quite clear why its progressive addition increased the plasticity of the bentonite. Its interaction with bentonite might have transformed it from being non-plastic to behaving like a plastic, thereby increasing the range of water content for which the sawdust-treated bentonite exhibits plastic properties.

3.2.3. Compaction Characteristics

The compaction characteristics of a soil are described by its optimum moisture content (OMC) and maximum dry unit weight (MDUW). The variation of the OMC and MDUW of the clay with sawdust and bentonite with sawdust are graphically illustrated in Figs. 6 and 7.

Figs. 6 and 7 show that the OMC increased, while the MDUW decreased, as the sawdust content in the treated samples increased. With increasing sawdust content, the

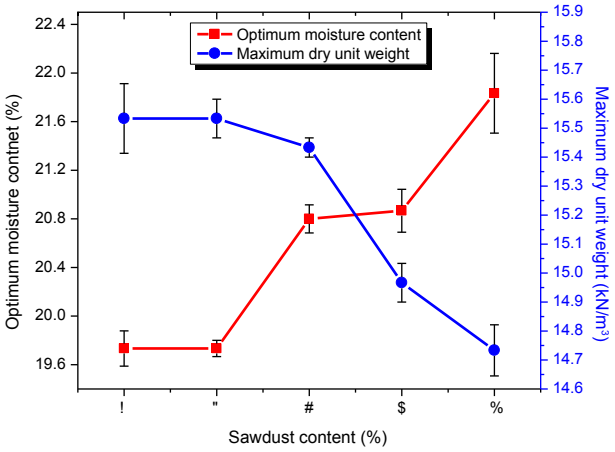

Figure 6. Variation of the compaction characteristics of the clay with sawdust.

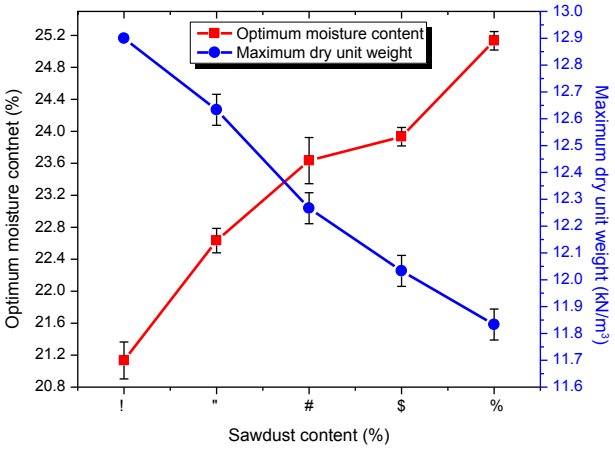

Figure 7. Variation of the compaction characteristics of the bentonite with sawdust.

treated samples required more water in order to attain the MDUW. This is because some of the water in the sawdust-modified samples gets absorbed by the sawdust. However, the MDUW achieved decreased with increasing sawdust content. This can be attributed to the lower specific gravity of the sawdust. The MDUW are lower and the OMC greater for the modified bentonite.

3.2.4. Strength Characteristics

The variation of the unconfined compressive strengths (UCS) of the clay and the bentonite are shown in Fig. 8. The UCS of a soil is a measure of the maximum load it can withstand per unit area, when its lateral confining pressure is zero. The UCS of the treated samples decreased with increasing sawdust content. The sawdust has a low density and compressive strength compared with that of the clay and bentonite. This explains why the UCS of the treated clay and bentonite decreases as their sawdust contents progressively increased.

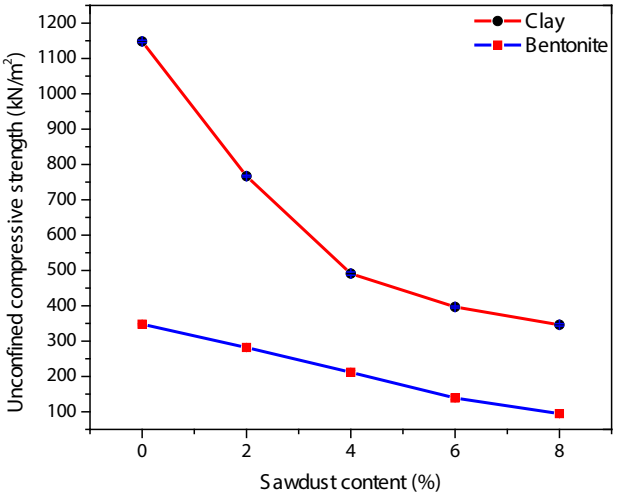

Figure 8. Variation of the UCS of the clay and bentonite with sawdust.

3.2.5. Permeability

The variation of the permeability of the treated clay and bentonite with their sawdust contents are presented in Fig. 9. The permeability of a soil gives a measure of the ease with which water flows through it. Fig. 9 shows that the higher the sawdust content, the easier it is for the water to flow through the sawdust-treated clay and sawdust-treated bentonite. This is attributed to the increasing pore space in the treated clay and bentonite as their sawdust content increases. The SEM morphology for the natural soil and for the soil admixed with varying percentages of sawdust (Fig. 10) show increasing

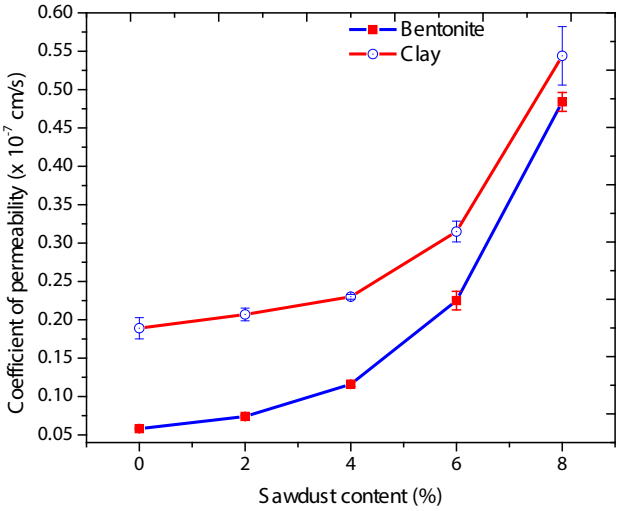

Figure 9. Variation of the permeability of the clay and bentonite with sawdust.

pore space as the percentage of the sawdust in the clay increases. The pore size of the bentonite also increased as its sawdust content increased (Fig. 11).

A typical clay liner material should have a hydraulic conductivity (permeability) less than or equal to 1 x 10^{-7} cm/s and a strength greater than 200 kN/m^2 [31, 32]. The coefficients of permeability of the clay and bentonite are less than 1 x 10^{-7} cm/s, which is generally specified as the hydraulic conductivity requirement that clays need to satisfy in order to be used as landfill-liner materials. The UCS of the clay and bentonite are greater than 200 kN/m^2, indicating that a layer of a lining system using this clay or bentonite can sufficiently support the load from landfilled wastes that may be imposed on it. Also, the modification of the clay with 8% or less sawdust and that of the bentonite with 4% or less sawdust satisfy these permeability and strength requirements. The National Rivers Authority (NRA) [33] stated that a soil to be used as a clay liner should have its liquid limit and plasticity index less than 90% and 65%, respectively, and clay content greater than 10%. The bentonite and its modification with sawdust have their liquid limits greater than 90%. Therefore, this makes the bentonite and its modification with sawdust unstable and unsuitable for use as a landfill liner.

4. CONCLUSIONS

The clay and bentonite samples contain silica, alumina and iron III oxide as their predominant oxides. The clay mineral in the clay is kaolinite, whereas that in the bentonite is montmorillonite, which is highly expansive.

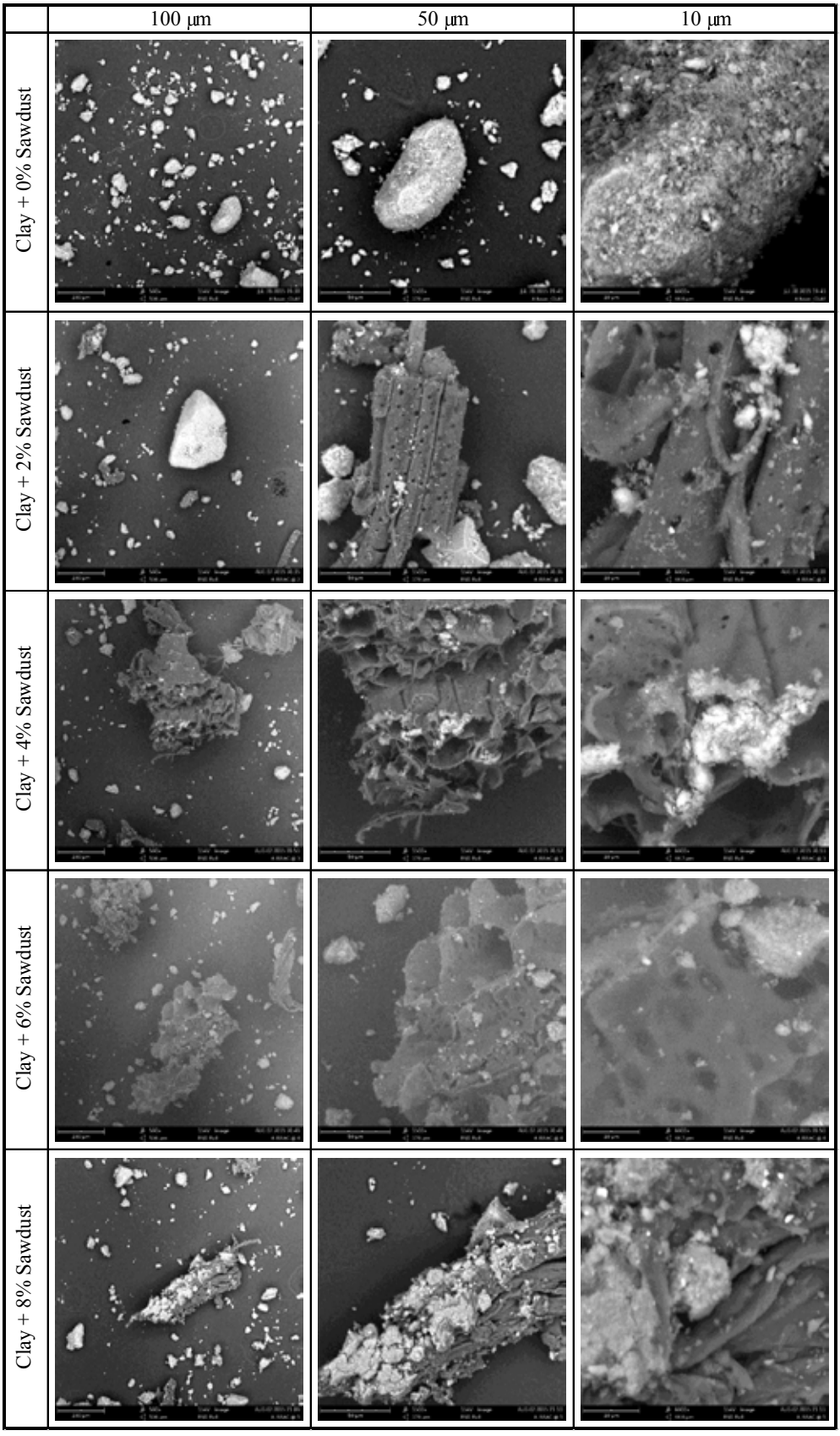

Figure 10. SEM micrograph of the clay with sawdust.

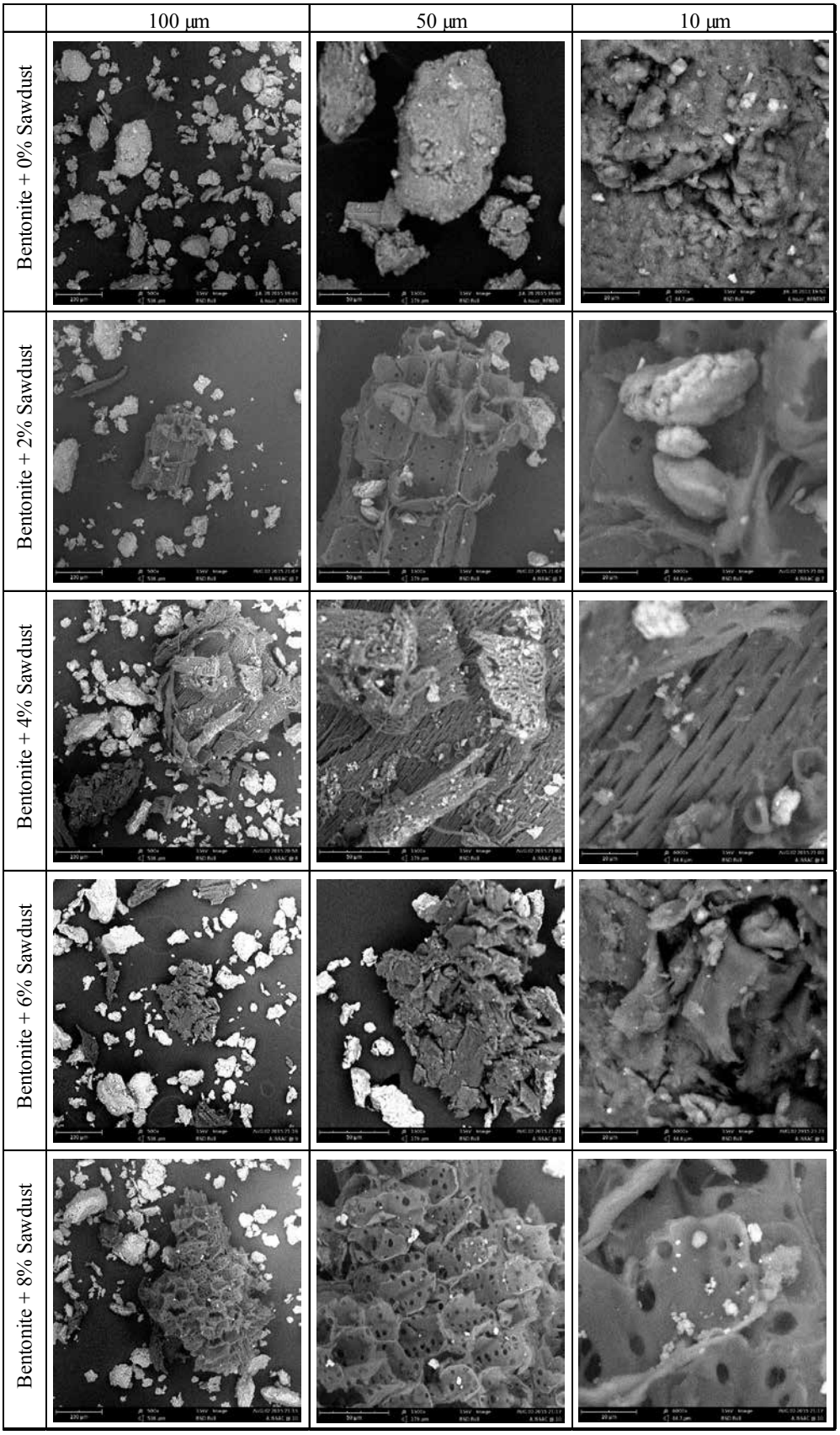

Figure 11. SEM micrograph of the bentonite with sawdust.

The clay is of high plasticity, while the bentonite has an extremely high plasticity.

The modification of the clay with an increasing percentage of sawdust caused a reduction in its specific gravity, plasticity, MDUW and UCS, while it caused an increase in its OMC and permeability. Consequently, improving the workability of the clay, but reducing its strength. The modification of the bentonite with the sawdust resulted in a reduction in its specific gravity, MDUW and UCS, while it increased its plasticity (slightly), OMC and permeability.

The clay and bentonite both have sufficiently low permeability to satisfy the hydraulic conductivity requirement for use as clay liners. The clay and sawdust-modified clay also satisfy the clay content, Atterberg limits and UCS requirements for use as landfill liners, whereas the bentonite and sawdust-modified bentonite did not satisfy the Atterberg limits and UCS requirements (for modification with more than 4% sawdust). An 8% sawdust application to a clay having similar properties as that of this study is recommended for modifying it for use in a landfill-liner system.

Following Bulut and Tez's [18] recommendation of sawdust as a low-cost adsorbent of heavy metals, the implication of these findings is that modification of a clay (having similar properties as that studied and suitable for use as a landfill liner) with sawdust has the potential of improving the removal of hazardous metals from landfills and protecting groundwater. Also, the use of sawdust –which is usually disposed improperly and thereby constitutes a nuisance to the environment and public health – gives assurance of the sustainable development of people and society.

The increase in the permeability of the clay and bentonite with increasing sawdust content indicate that when soil drainage is important to a construction project, sawdust can be used to improve the drainage capacity of clays of very high plasticity by the addition of an appropriate proportion that will not compromise the stability of the layer of earthworks. Sand may be added to the mixture of bentonite and sawdust using a proportion that ensures that the resulting lining system is stable, while the composite satisfies the permeability and strength requirements for use as a landfill liner.

Acknowledgments

Isaac Akinwumi thanks the Commonwealth Scholarship Commission in the UK for the award of a split-site PhD Scholarship.

REFERENCES

[1] Aqeel, A. 2016. Investigation of expansive soils in Obhor Sabkha, Jeddah-Saudi Arabia. Arabian Journal of Geosciences 9, 314, 1–14. DOI: 10.1007/s12517-016-2341-x

[2] Wyoming Office of Homeland Security, 2016. Wyoming State Mitigation Plan 2016 – 2021. Wyoming Office of Homeland Security, Cheyenne, WY, 324p, http://wyohomelandsecurity.state.wy.us/mitigationplanning/Final_Wyoming-State-Mitigation-plan_012516.pdf [accessed 11.08.2016].

[3] Seco, A., Ramirez, F., Miqueleiz, L., Garcia, B. 2011. Stabilization of expansive soils for use in construction. Applied Clay Science 51, 3, 348–352. DOI: 10.1016/j.clay.2010.12.027

[4] Perez-Rea, M., Ayala-Ibarra, T., Castano, V.M. 2015. Prediction of final settlements of buildings constructed on expansive soils. International Journal of Engineering and Technology 4, 3, 424–431. DOI: 10.14419/ijet.v4i3.4165

[5] Nagaraj, H., Munnas, M., Sridharan, A. 2010. Swelling behavior of expansive soils. International Journal of Geotechnical Engineering 4, 1, 99–110. DOI: 10.3328/IJGE.2010.04.01.99-110

[6] Zumrawi, M.M.E. 2000. Performance and design of expansive soils as road subgrade. PhD Thesis, Chang'an University, Xi'an.

[7] Shi, B., Chen, S., Han, H., Zheng, C. 2014. Expansive soil crack depth under cumulative damage. The Scientific World Journal, Article ID 498437, 9p. DOI: 10.1155/2014/498437

[8] Elkady, T.Y. 2016. The effect of curing conditions on the unconfined compression strength of lime-treated expansive soils. Road Materials and Pavement Design 17, 1, 52–69. DOI: 10.1080/14680629.2015.1062409

[9] Komonweeraket, K., Cetin, B., Aydilek, A., Benson, C., Edil, T. 2015. Geochemical analysis of leached elements from fly ash stabilized soils. Journal of Geotechnical and Geoenvironmental Engineering 141, 5, 0001288. DOI: 10.1061/(ASCE)GT.1943-5606.0001288

[10] Akinwumi, I.I. 2014. Soil modification by the application of steel slag. Periodica Polytechnica Civil Engineering 58, 4, 371–377. DOI: 10.3311/PPci.7239

[11] Anggraini, V., Huat, B.B.K., Asadi, A., Nahazanan, H. 2015. Relationship between the compressive and tensile strengths of lime-treated clay containing coconut fibres. Acta Geotechnica Slovenica 12, 1, 49–57.

[12] Akinwumi, I.I., Booth, C.A. 2015. Experimental insights of using waste marble fines to modify

the geotechnical properties of a lateritic soil. Journal of Environmental Engineering and Landscape Management 23, 2, 121–128. DOI: 10.3846/16486897.2014.1002843

[13] Malekzadeh, M., Bilsel, H. 2014. Hydro-mechanical behaviour of polypropylene fiber reinforced expansive soils. KSCE Journal of Civil Engineering 18, 7, 2028–2033. DOI: 10.1007/s12205-014-0389-2

[14] Sivrikaya, O., Yavascan, S., Cecen, E. 2014. Effects of ground granulated blast furnace slag on the index and compaction parameters of clayey soils. Acta Geotechnica Slovenica 11, 1, 19–27.

[15] Ganapathy, G.P., Gobinath, R., Akinwumi I.I., Kovendiran, S., Thangaraj, M., Lokesh, N., Muhamed Anas, S., Arul murugan, R., Yogeswaran, P., Hema, S. 2017. Bio-enzymatic stabilization of a soil having poor engineering properties, International Journal of Civil Engineering 15, 3, 401–409. DOI: 10.1007/s40999-016-0056-8.

[16] Ojuri, O.O. 2015. Geotechnical characterization of some clayey soils for use as landfill liner. Journal of Applied Sciences and Environmental Management 19, 2, 211–217. DOI: 10.4314/jasem.v19i2.6

[17] Burnley, S., Cooke, D., Gladding, T. 2005. T308 Environmental Monitoring, Modelling and Control: Block 4 Solid Wastes Management. The Open University, Milton Keynes.

[18] Bulut, Y., Tez, Z. 2007. Removal of heavy metals from aqueous solution by sawdust adsorption. Journal of Environmental Sciences 19, 160–166. DOI: 10.1016/S1001-0742(07)60026-6

[19] Itoandon, E.E., Olatope, S.O.A., Shobowale, O.O. 2012. Preliminary phytochemical analysis and antimicrobial properties of crude extract of Combretodendron Macrocarpum stem bark. Nigerian Food Journal 30, 2, 51–56. DOI: 10.1016/S0189-7241(15)30035-7

[20] USDA, 2016. Wood technical fact sheet – Combretodendron macrocarpum. http://www.fpl.fs.fed.us/documnts/TechSheets/Chudnoff/African/htmlDocs_africa/Combretodendronmacrocarpum.html [accessed 30.05.16].

[21] Gupta, S., Babu, B.V. 2009. Removal of toxic metal Cr (VI) from aqueous solutions using saw-dust as adsorbent: Equilibrium, kinetics and regeneration studies. Chemical Engineering Journal 150, 2–3, 352–365. DOI: 10.1016/j.cej.2009.01.013

[22] BSI, 1996. Methods of test for soils for civil engineering purposes. BS 1377: Part 2: 1990, British Standards Institution, London.

[23] BSI, 1990. British standard methods of test for soils for civil engineering purposes. BS 1377: Part 4: 1990, British Standards Institution, London.

[24] BSI, 1990. British standard methods of test for soils for civil engineering purposes. BS 1377: Part 7: 1990, British Standards Institution, London.

[25] Head, K.H. 1994. Manual of Soil Laboratory Testing, Volume 2: Permeability, Shear Strength and Compressibility Tests, 2nd edn. Wiley, New York.

[26] Budhu, M. 2011. Soil mechanics and foundations, third edition. John Wiley & Sons Inc., New Jersey.

[27] Tran, H.M. 2005. Quantifying the effects of sawdust application on soil chemical and physical properties and corn yield. Master's Thesis, University of Tennessee, Knoxville.

[28] Akinwumi, I.I., Booth, C.A., Diwa, D., Mills, P. 2016. Cement stabilisation of crude-oil-contaminated soil. Proceedings of the Institution of Civil Engineers – Geotechnical Engineering 169, 4, 336–345. DOI: 10.1680/jgeen.15.00108

[29] Akinwumi, I.I., Ukegbu, I. 2015. Soil modification by addition of cactus mucilage. Geomechanics and Engineering 8, 5, 649–661. DOI: 10.12989/gae.2015.8.5.649

[30] El Halim, A.A., El Baroudy, A.A. 2014. Influence addition of fine sawdust on the physical properties of expansive soil in the Middle Nile Delta, Egypt. Journal of Soil Science and Plant Nutrition 14, 2, 483–490. DOI: 10.4067/S0718-95162014005000038

[31] Guney, Y., Cetin, B., Aydilek, A.H., Tanyu, B.F., Koparal, S. 2014. Utilization of sepiolite materials as a bottom liner material in solid waste landfills. Waste Management 34, 1, 112–124. DOI: 10.1016/j.wasman.2013.10.008

[32] Osinubi, K.J., Nwaiwu C.M.O. 2006. Design of compacted lateritic soil liners and covers. Journal of Geotechnical and Geoenvironmental Engineering 132, 2, 203–213. DOI: 10.1061/(ASCE)1090-0241(2006)132:2(203)

[33] NRA 1989. Earthworks to landfill sites. National Rivers Authority, North-West Region.

NOSILNOSTI TEMELJEV NA NEZASIČENIH ZEMLJINAH

Taha Taskiran
Dicle University,
Faculty of Engineering,
Department of Civil Engineering
21280, Diyarbakir, Turčija
E-pošta: taha@dicle.edu.tr
E-pošta: tahtaskiran@gmail.com

Ključne besede

nezasičene zemljine, nosilnost temeljev na nezasičenih zemljinah, sukcijska trdnost, načrtovanje temeljenja

Izvleček

Raziskovanje nezasičenih zemljin je zelo pomembno, še vedno pa je treba raziskati številne tehnične vidike takšnih zemljin. V prispevku je predlagana nova tehnika, ki napoveduje spreminjanje nosilnosti nezasičenih zemljin z matrično sukcijo. Predlagana metoda je razširitev konvencionalnih teorij nosilnosti in konceptualno temelji na logaritemskem modelu strižne trdnosti nezasičenih zemljin, ki vključujejo le en neznan nezasičen parameter (vstopno vrednost zraka, AEV). Možnost napovedi nosilnosti nezasičenih zemljin kažejo efektivni parametri zasičene strižne trdnosti c 'in Ø' in AEV iz retencijske krivulje zemljina--voda (SWRC). Glede na to, da je potrebno nove metode potrditi s podatki drugih raziskovalcev, se je predlagana enačba preizkusila s pomočjo avtorjeve objavljene eksperimentalne študije nezasičenih zemljin ter nekaterih poročanih eksperimentalnih študij o strižni trdnosti za nezasičene zemljine in modelne obremenitve temeljev na nezasičenem pesku pod nadzorovanimi sukcijskimi pogoji. Rezultati študije kažejo, da obstaja dobra primerjava med "nezasičenimi nosilnostmi", dobljenimi s predvidenimi in izmerjenimi nezasičenimi parametri trdnosti (c_{total}, Ø), pa tudi med izmerjenimi/izračunanimi vrednostmi nosilnosti modela obremenjenega temeljenja. Izkazalo se je, da za to ni potrebe po kompleksnih nezasičenih preskusnih napravah, ter da se lahko s pomočjo predlagane enačbe napove nosilnost nezasičenih drobnozrnatih in peščenih zemljin, za katere potrebujemo samo en nezasičen parameter, ki ga je mogoče pridobiti iz SWRC ali predvideti z uporabo osnovnih indeksnih lastnosti zemljin.

AN UNSATURATED-SOILS APPROACH TO THE BEARING CAPACITY OF FOUNDATION STRUCTURES

Taha Taskiran
Dicle University,
Faculty of Engineering,
Department of Civil Engineering
21280, Diyarbakir, Turkey
E-mail: taha@dicle.edu.tr
E-mail: tahtaskiran@gmail.com

Keywords

unsaturated soils, unsaturated bearing capacity, suction strength, foundation design

Abstract

Unsaturated soils are maintaining their importance for researchers and there is still much need to investigate the many engineering aspects of these soils. A new technique is proposed here to predict the variation of the bearing capacity of unsaturated soils with matric suction. The proposed method is an extension of conventional bearing-capacity theories and conceptually based on the logarithmic model of the shear strength of unsaturated soils, which only include one unknown, unsaturated parameter (the air-entry value, AEV). The possibility of predicting the unsaturated bearing capacity of soils is shown by the saturated effective shear-strength parameters c' and Ø' and the AEV from the soil-water retention curve (SWRC). Considering the necessity of validating new methods with other researchers' data, the proposed equation is tested using the published unsaturated experimental study by the author, in addition to some reported experimental studies on the shear strength for unsaturated soils and also a model footing loading on unsaturated sand under controlled suction conditions. The results of the study indicate that there is a good comparison between the "unsaturated bearing capacities" obtained via predicted and measured unsaturated strength parameters (c_{total}, Ø) and also between the measured/calculated bearing values of a model footing loading. Consequently, it is shown that, without needing complex unsaturated testing facilities, the proposed equation is capable of predicting the unsaturated bearing capacity for both fine-grained and sandy soils, requiring only one unsaturated parameter, which can be obtained from the SWRC or predicted using the basic soil-index properties.

1 INTRODUCTION

One of the important engineering properties required for the design of shallow foundations is the bearing capacity. Several approaches are available in the literature for a determination of the bearing capacity of soils based on the saturated shear-strength parameters ([1], [2]). However, in some situations, shallow foundations are located above the ground-water table where the soil is under capillary tension and thus in a state of unsaturated condition. Besides, many kinds of natural soils, such as desiccated silts and clays, transported soils, residual soils and artificial compacted soils, are found in the unsaturated condition where $u_w<0$. Nevertheless, the bearing capacities of soils are often determined by assuming fully saturated conditions, ignoring the influence of the capillary stresses or the matric suction. Therefore, a bearing-capacity estimation of the shallow foundations using conventional approaches may not be reliable, leading to uneconomic designs.

Several researchers performed investigations on the bearing capacity of unsaturated soils ([3], [4], [5], [6], [7]) All these studies have shown that there is a significant contribution of the matric suction to the bearing capacity of unsaturated soils. However, limited theoretical research work is reported in the literature with respect to the interpretation of the bearing capacity of unsaturated soils ([3], [8]).

In this study, a semi-empirical equation is proposed to predict the variation of the bearing capacity of unsaturated soils with matric suction, using the saturated shear-strength parameters c' and $\emptyset'$ and the air-entry value. The equation presented in this paper is developed by extending the concepts for predicting the shear strength of unsaturated soils proposed by Kayadelen et al. [9]. The equation proposed here is exercised for other studies reported in the literature that include a variation of the cohesion with the matric suction for fine-grained soils and also a sand-box model footing bearing capacity test results of unsaturated coarse-grained soils. In the content of this study, benefiting from the previously reported, unsaturated test results, unsaturated bearing capacities for a typical square footing (B=L=1m) were calculated based on unsaturated, experimental soil properties and ones obtained with the theoretical equation proposed here and a comparison was made between the bearing capacities. The studies presented in this paper show that there is a good comparison between the bearing capacities of an example square footing via theoretically and experimentally obtained soil parameters.

2 REVIEW OF THE BEARING CAPACITY OF UNSATURATED SOILS

Meyerhof [2] proposed an equation for predicting the bearing capacity of shallow strip footings for the soil failure mechanism. This equation is valid for strip footings resting in a homogenous soil and subjected to a vertical loading.

$$q_u = c'N_c\varepsilon_c + qN_q\varepsilon_q + 0{,}5B\gamma N_\gamma\varepsilon_\gamma \qquad (1)$$

where:

q_u = ultimate bearing capacity, kPa
q = overburden pressure, kPa
c' = effective cohesion, kPa
ε_c, ε_q, ε_γ = shape factors due to cohesion, overburden and unit weight
N_c, N_q, N_γ = bearing capacity factors due to cohesion, surcharge and unit weight, respectively
γ = soil unit weight, kN/m^3
B = footing width, m

As in the case of saturated soil, the bearing capacity of unsaturated soils is similarly calculated using two different methods, which are the 'effective stress approach' (ESA) and the 'total stress approach' (TSA). Oloo [4] proposed a method to predict the bearing capacity of surface footing on unsaturated fine-grained soils as extending the effective stress approach (ESA) as follows:

$$q_{ult(unsat)} = \{c' + (u_a - u_w)_b \tan\emptyset' + [((u_a - u_w) - (u_a - u_w)_b] \tan\emptyset^b\}N_c + 0{,}5B\gamma N_\gamma \qquad (2)$$

where;

$(u_a - u_w)_b$ = Air – entry value of soil
$(u_a - u_w)$ = Matric suction

Due to the limitations that the bearing capacity varies linearly and decreases beyond the residual water content for the coarse-grained soils, and converges to a certain value for fine-grained soils, which is not the general behaviour for the equation proposed by Oloo [4], Vanapalli and Mohammed [6] proposed a relationship that contains a nonlinear variation of the bearing capacity of unsaturated soils with respect to the matric suction for surface footings extending the ESA approach. The term $S^\varphi \tan\emptyset'$ considers the non-linear variation of the shear strength of unsaturated soils using a fitting parameter, φ. Equation (3) can be used to predict the bearing capacity of unsaturated soils that desaturate on the application of a matric suction.

$$q_u = [c' + (u_a - u_w)_b(1 - S^\varphi \tan\emptyset') + (u_a - u_w)_{AVR}S^\varphi \tan\emptyset']N_c\varepsilon_c + 0.5B\gamma N_\gamma\varepsilon_\gamma \qquad (3)$$

where:

φ = bearing capacity fitting parameter
ε_c, ε_γ = shape factors due to cohesion and unit weight
$(u_a - u_w)_{AVR}$ = Average matric suction below the foundation

The evaluation of change in pore water pressure within the effective stress zone of a foundation is relatively complex and depends on many factors, such as climatic changes, the amount of influx and outfluxes of water, soil properties, depth of the underground water table, etc. The hydrostatic line relative to the groundwater table represents an equilibrium condition where there is no flux to ground at the ground surface. During dry periods, the pore water pressure becomes more negative than that represented by hydrostatic line, and the opposite condition occurs during wet periods [7].

In arid and semi-arid areas the underground water table is found at a relatively deeper part of the soil profile, and

thus soils are under a highly negative pore-water condition. The assumption of a shallower groundwater table and a hydrostatic line in such climatic conditions results in lower suction and thus lower unsaturated bearing capacity than the actual case, which causes it to remain on the safe side for foundation design.

The average matric suction below the footing can be found in Fig. 1 (Vanapalli and Mohammed, [6]).

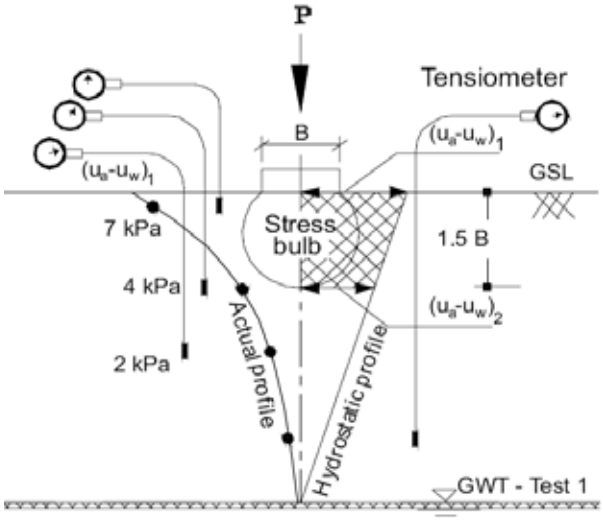

Figure 1. Procedure used for determining the average matric suction below the footing ([6]).

Vanapalli and Mohamed [6] extended Eq. (3) for an estimation of the bearing capacity of unsaturated fine-grained soils and suggested that the fitting parameter, φ, is a function of the plasticity index, I_p , as shown in Eq. (4) (φ = 1 for I_p = 0). They also experimentally found that for coarse-grained soils that φ has a value of 1. The advantage of this model is that it is capable of modelling "decrease attenuation" beyond the residual water content for some soils.

$$\varphi = -0{,}003\left(I_p\right)^2 + 0{,}3988\left(I_p\right) + 1 \qquad (4)$$

Vanapalli and Oh [10] analysed two more sets of in-situ plate load test results ([5], [11]) and showed that the φ value is constant (i.e., φ = 3.5) for I_p values greater than 8%.

Some researchers performed an unsaturated loading test on site to investigate the characteristics of an unsaturated bearing capacity. Among them, Schnaid et al. [12] performed in-situ plate (0.3, 0.45, 0.6, 0.7 and 1 m) load tests on unsaturated fine-grained soils. They found that the bearing-capacity values that they calculated by the ESA were 4 to 6 times greater than the measured values. Similar trends were also observed for the in-situ plate (Dia. = 0.8 m) load tests results by Costa et al. [5]. Most researchers, for the ESA approach, interpreted the discrepancy between the measured and the predicted values as resulting from the poorly-defined drainage conditions of the pore air and water of unsaturated conditions and also due to not observing a well-defined "general shear failure" mode, which is not the most common case for unsaturated soils for both in-situ plate load and model footing tests ([4], [13], [12], [5], [11], [14]).

The behaviour of the bearing mechanism for unsaturated, fine-grained soils below footings was considered by some researchers ([13], [15]) as an occurring punching shear failure (PSF) mechanism under a total stress condition (TSA). For PSF conditions, a compressible block of soil beneath the footing is taken into consideration and slip surfaces below the footings are typically not extended to the ground surface, but instead limits to the vertical planes of that soil block. For fine-grained soils, Vanapalli et al. [13] extended the above concept and proposed a method to estimate the bearing capacity using unconfined compression-test results, as shown in Eq. (5).

$$q_{ult(unsat)} = \left[\frac{q_{u(unsat)}}{2}\right] \varepsilon_{cv} N_{cw} \qquad (5)$$

where

$q_{ult(unsat)}$ = ultimate bearing capacity for unsaturated soil,
$q_{u(unsat)}$ = unconfined compressive strength for unsaturated soil,
N_{CW} = bearing-capacity factor with respect to the constant water-content condition
ε_{cv} = shape factor with respect to the constant water-content condition.

Using fine-grained soils, Vanapalli et al. [13] carried out small-scale model footing tests (B × L = 50 × 50 mm) for varying matric suction values of the foundation soil (0, 55, 100, 160, 205 kPa) to study the validity of Eq. (5) and to determine the bearing-capacity factor, N_{cw}. They found that the calculated bearing capacities using Eqn 5 were in good agreement with the measured values as N_{cw} was taken as 5.14 that is used for the Skempton [16] bearing-capacity theory. Using the in-situ plate load tests results by Costa et al. [5], Vanapalli [13] also showed the comparison between the measured bearing-capacity values and those also extending both the ESA (i.e. Eq. (2) along with the reduction factors approach and the TSA (Eq. (5)) towards the bearing capacity. The results showed that the bearing-capacity values estimated by extending the TSA are conservative and reasonable, whereas those estimated by extending the ESA are significantly overestimated.

Consoli et al. [14] performed in-situ plate (1 m × 1 m) load tests in a residual homogeneous, cohesive soil (I_p = 20%). The bearing-capacity values estimated using the ESA were obtained overestimated by 1.5–2.5 times compared to the measured values. On the other hand, the bearing capacity calculated by the TSA using the average unconfined compressive strength (i.e., 50.2 kPa) was obtained with approximately the same as measured value of 1 m square concrete footing.

Oh and Vanapalli [17] proposed a model to predict the variation of shear strength of the "unsaturated fine grained" soils with respect to suction using the shear strength derived from an unconfined compression test for the specimens under saturated conditions and the SWCC as presented below. After obtaining the unsaturated cohesion for the interested matric suction value it will become possible to calculate the bearing capacity of footing benefiting from Eqn. 5 in the context of the TSA.

$$c_{u(unsat)} = c_{u(sat)}\left[1 + \frac{(u_a - u_w)}{P_a/_{101,3}}(S^v)/\mu\right] \qquad (6)$$

The studies performed by various researches ([17], [16], [10]) have shown that either by laboratory or in-situ tests, the measured unsaturated bearing-capacity values of a footing resting on unsaturated soils are in good agreement with the predicted results calculated by TSA, while it is noticeably overestimated by ESA. It can be concluded that more theoretical/laboratory works are still needed for more accurately predicting the unsaturated bearing capacities of footings, especially by ESA.

Therefore, in the content of the current study a semi-empirical model were presented for predicting the variation of unsaturated bearing capacity for both coarse- and fine-grained soils. The model is simple, requires only one unsaturated parameter (air entry value) from the soil-water characteristic curve (i.e., SWCC). The proposed model can have practical use and it enables a smooth transition between the unsaturated and saturated soil behaviour. That means the proposed semi-empirical models converts to conventionally used equations when the matric suction value is zero (i.e., the saturated condition).

3 AN EQUATION FOR THE BEARING CAPACITY OF UNSATURATED SOILS

Several investigators reported that the behaviour of the shear strength due to suction has a non-linear character. We previously proposed a non-linear equation for a variation of the shear strength with respect to the matric suction, matching experimental data with a matching function and assumed *logarithmic* relation between the suction strength and the matric suction ([9]). The suction contribution to shear strength was offered in a relation, as stated below:

$$\tau_{us} = \tan\emptyset'(u_a - u_w)_b + P_{at})\ln\left[\frac{(u_a - u_w) + P_{at}}{P_{at}}\right] \qquad (7)$$

Equation (7) reflects the contribution of the matric suction to the shear strength using only one additional parameter of unsaturated properties, which is the air-entry value. This contribution might be thought to be a part of the total cohesion of unsaturated soils. Therefore, the total cohesion can be expressed as shown below:

$$c_{Total} = c' + \tan\emptyset'(u_a - u_w)_b + P_{at})\ln\left[\frac{(u_a - u_w) + P_{at}}{P_{at}}\right] \quad (8)$$

As can be seen, the total cohesion is composed of two parts, which is the effective cohesion (c') and the suction contribution to the cohesion $\tan\emptyset'(u_a - u_w)_b + P_{at})\ln\left[\frac{(u_a - u_w) + P_{at}}{P_{at}}\right]$, respectively. For normally consolidated saturated cohesive soils, both the effective cohesion (c') and the suction part of the total cohesion are approximately zero and as the cohesive soils move away from saturated conditions, the suction-contribution part becomes effective and the soil gains cohesion. At this stage, the magnıtude of the cohesion is greatly enhanced due to the level of suction. For the granular soils, the effective cohesion for granular soil is approximately null, while the second part of the cohesion, which is due to suction, forms the total cohesion for the unsaturated condition, and this can also be considered as apparent cohesion for the granular soil under unsaturated conditions.

On the other hand, the equation proposed for the bearing capacity of saturated soils can be written as given below for adopting the bearing capacity of the surface footings, taking account of the influence of the shear strength contribution due to the matric suction for unsaturated soils:

$$q_u = \left[c' + \tan\emptyset'(u_a - u_w)_b + P_{at})\ln\left[\frac{(u_a - u_w) + P_{at}}{P_{at}}\right]\right]N_c\varepsilon_c + \\ + 0.5B\gamma N_\gamma\varepsilon_\gamma \qquad (9)$$

where:

$(u_a - u_w)_b$ = Air-entry value of the foundation soil
ε_c, ε_γ = shape factors due to cohesion and unit weight (Meyerhof)
$(u_a - u_w)$ = matric suction (can be taken as the average matric suction below the footing within the effective stress zone).

The matric suction can be obtained as stated below:

$$(u_a - u_w) = (u_a - u_w)_{AVR} = {}^1/_2 \left[(u_a - u_w)_1 + (u_a - u_w)_2\right] \quad (10)$$

The hydrostatic water-pressure distribution that was given in Fig. 1 can be used to obtain the average matric suction below the footing, considering the effective stress zone, for practical engineering purposes. The average suction within the effective stress zone can also be measured via proper suction devices for more accurate values of the average suction.

The bearing-capacity contribution due to the matric suction can be obtained from a part of Equation (9), which is equal to $N_c \varepsilon_c \left[\tan \emptyset' (u_a - u_w)_b + P_{at}) \ln \left({}^{(u_a - u_w) + P_{at}}/_{P_{at}} \right)\right]$.

As can be seen, the AEV is the only unsaturated parameter in Eqn. (9), and it needs to be measured in the laboratory or on site, or obtained in any indirect way. The air-entry value (AEV) corresponds to the value of the negative pore-water pressure when the largest voids or pores begin to drain freely. It is a function of the maximum pore size in the soil and is also influenced by the pore-size distribution within a soil. Soils with large, uniformly shaped pores have relatively low AEVs, such as uniform sandy soils with a wider distribution of pore sizes, such as well graded silts that have a relatively higher AEV. The pores between the individual clay particles in clayey soil are small and this results in a higher value of AEV. The AEV values of soils are obtained from the volumetric water-content function of the soils and it generally varies in a narrow range, especially for sandy and silty soils, and therefore the predictions for AEV mostly do not give values that are far away from the measured values.

It is not especially difficult to obtain a direct measurement of a volumetric water-content function in a laboratory, but it requires time and finding special equipment. It is, however, standard practice to obtain a grain-size distribution curve and many soil laboratories have the facilities to obtain the grain-size distribution curves. Based on basic soil properties such as the soil grain size distribution, void ratio, Atterberg limits, several researchers presented various methods to predict the volumetric water-content function ([18], [19], [20], [21]). As an example, Aubertin et al.'s [20] method predicts the volumetric water-content function using basic soil properties such %10 and % 60 passing, void ratio and liquid limit.

Alternatively, there are some sample water-content function curves prepared for practical engineering purposes, and these curves can be used to provide an AEV value regarding the type of soils. Consequently, it is seen that with the proposed method with Eqn. 9 used here, the unsaturated bearing capacity can be calculated using saturated parameters (c', Ø') and basic soil parameters such as the grain size distribution and the index properties.

4 COMPARISON OF THE BEARING CAPACITIES OF UNSATURATED SOILS

In order to examine the performance of the unsaturated bearing-capacity equation, Eqn. 9, it benefited from the results of an experimental unsaturated shear strength study carried out by one previous experimental study by the author (Kayadelen et. al. [9]) and by some other researchers. Considering the difficulty of performing unsaturated tests and also the necessity of validating new methods with other previous study data, the current working methods were followed. The experimental saturated strength parameters, such as the effective cohesion c' and the internal friction angle Ø', were collected from previous published works carried out by the author and some other researchers and using Eqn. 8 the total cohesion, c_{total}, for unsaturated soils corresponding to various suctions were calculated. Based on calculated unsaturated strength parameters, the unsaturated bearing capacities of a typical square footing (1 m × 1 m) were calculated by the method proposed here ($q_{ult\ (with\ calculated\ parameters)}$) and also by means of the measured parameters ($q_{ult\ (with\ measured\ parameters)}$). Additionally, a sand-box measurement performed by Vanapalli et. al. [13] for the bearing capacity of the model footing on unsaturated sand with controlled suctions was also used to validate the proposed method. Bearing capacities were also calculated by the proposed Eqn. 9 and a comparison was made using the measured values obtained in the sand box.

For the current study, the saturated/unsaturated bearing capacities were calculated corresponding to various matric suction values (Ex: 0, 50, 100, 200, 300, 400 kPa) for typical model square footing. The total cohesion, c_{total}, (effective cohesion with suction strength contribution) were calculated for different suction values, while the internal friction angle, Ø', was taken as a constant for each interested soil. As can be seen from previous studies, the internal friction angle does not change considerably during the wetting/drying process for the unsaturated condition, especially for dealing with a range of suctions in most engineering practice (0–500 kPa). Among these studies, Vanapalli [22] showed results where Ø', independent of the suction for a glaciall till, was tested at various densities and initial water contents for a suction range of 0–500 kPa. Karube [23],

Table 1.Soil properties studied by various researchers.

Strength Parameters				
Reference	Soil Type	Ø'(°)	Air-entry value (kPa)	c' (kPa)
Vanapalli et. al. (1996)	Glacial Till compacted	23	32	0
Gan et. al. (1988)	Glacial Till	25.5	35	10
Miao et. al. (2002)	Nanyang expansive soil	21.3	25	32
Kayadelen et. al. (2007)	Residuel Clay	21.9	40	14.82
Vanapalli and Fathi (2007)	Sandy soil	35	3	0

Table 2. Comparison of calculated and measured bearing capacities and total cohesions.

Matric suction (kPa)	0	50	100	250	400	500
Calculated cohesion (c_{total})	0	14	38.47	70.36	90.48	100.77
q_{ult} (bearing capacity, Eqn 9, with measured parameters by Vanapalli et. al. (1996))	56	608	924	1975	2475	2764
q_{ult} (bearing capacity calculated by Eqn 9)	56	424	1068	1906	2435	2705

reported similar results for a kaolinite. Drumright [24] reported that Ø' was slightly influenced by the suction. Escario and Juca [25] found that Ø' was independent of the suction for Madrid clayey sand. Therefore, for most engineering purposes it would apparent that can be assumed as constant between the suction values of 0–500 kPa.

The reported soil properties and explanations about testing programs given by various researchers were summarized in Table 1 and in the following paragraphs.

The unsaturated shear strength behaviour of a statically compacted glacial till at three different water contents and densities, which are represented by optimum, dry and wet of optimum, were studied by Vanapalli et al. [26]. The experimental results of the unsaturated shear strength were compared with the predicted shear strengths. The cohesions calculated by Eqn. 8 corresponding to various suctions, bearing capacities results by Eqn. 9 using measured /calculated unsaturated parameters (c_{total} , Ø') are presented in Table 2 and Fig. 2 respectively.

Gun et al. [27] performed a series of consolidated, drained, single-stage and multi-stage direct shear tests on saturated/unsaturated compacted specimens prepared by Indian head glacial till at optimum conditions. The matric suctions ranged from 0 to 500 kPa. The cohesion calculated by Eqn. 8, with the bearing-capacity results using measured /calculated unsaturated parameters (c_{total} , Ø') by Eqn. 9, are presented in Table 3 and Fig. 3, respectively.

Miao et al. [28] performed a series of tri-axial tests under saturated/unsaturated conditions on remoulded

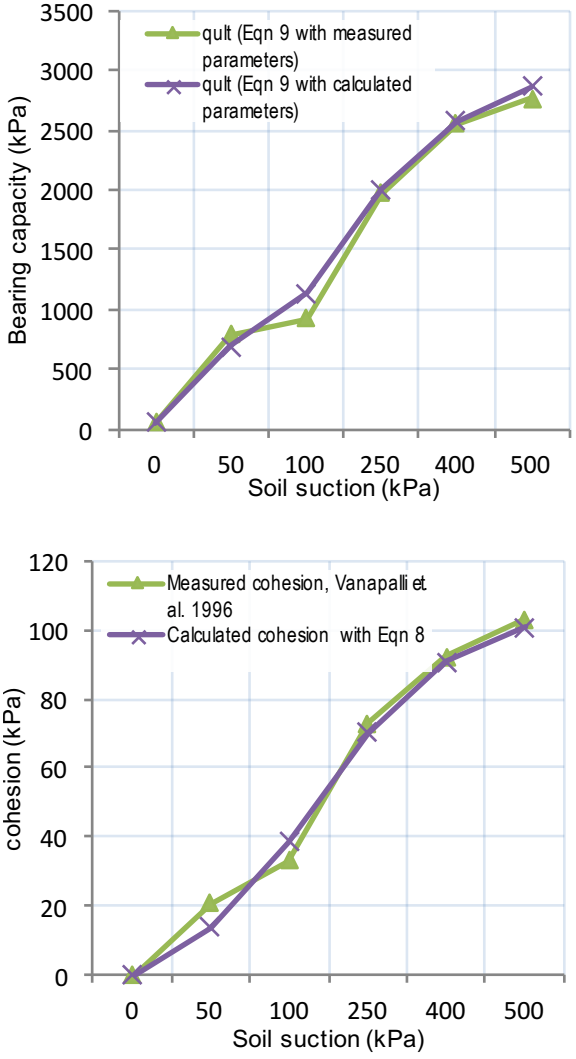

Figure 2. Comparison of calculated bearing capacities and total cohesions with measured values.

Table 3. Comparison of calculated and measured bearing capacities and total cohesions.

Matric suction (kPa)	0	50	100	200	300	400
Calculated cohesion (c_{total})	10	36.08	54.64	80.86	100	113.96
q_{ult} (bearing capacity, Eqn 9, with measured parameters by Vanapalli et. al. (1996))	410	1216	1849	2765	3345	3797
q_{ult} (bearing capacity calculated by Eqn 9)	410	1251	1850	2696	3313	3763

Table 4. Comparison of calculated and measured bearing capacities and total cohesions.

Matric suction (kPa)	0	50	80	120	200
Calculated cohesion (c_{total})	32	51.75	60.66	70.44	85.67
q_{ult} (bearing capacity, Eqn 9, with measured parameters by Vanapalli et. al. (1996))	779	1221	1400	1677	2098
q_{ult} (bearing capacity calculated by Eqn 9)	779	1233	1439	1665	2015

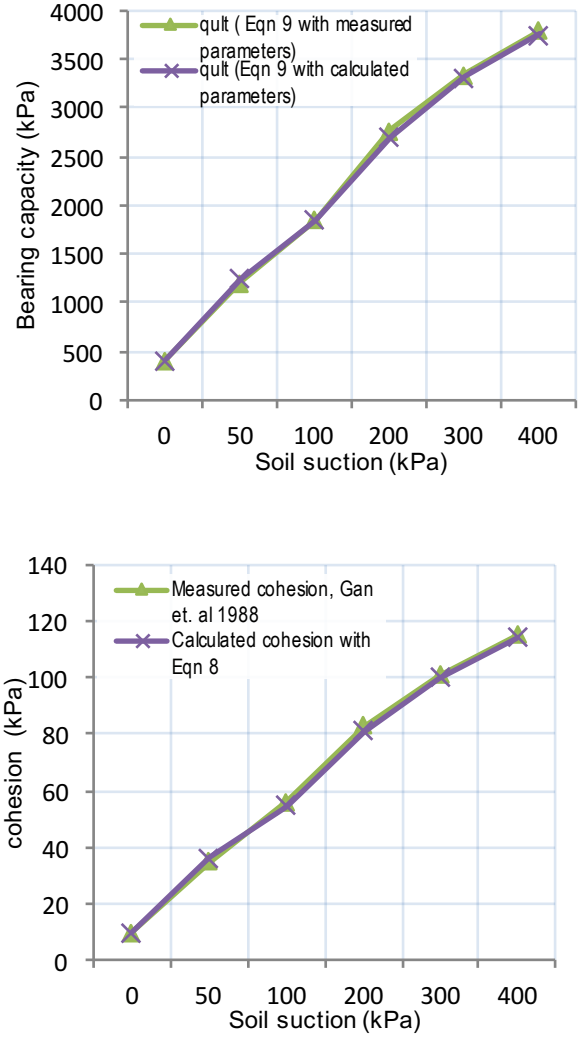

Figure 3. Comparison of calculated bearing capacities and total cohesions with measured values.

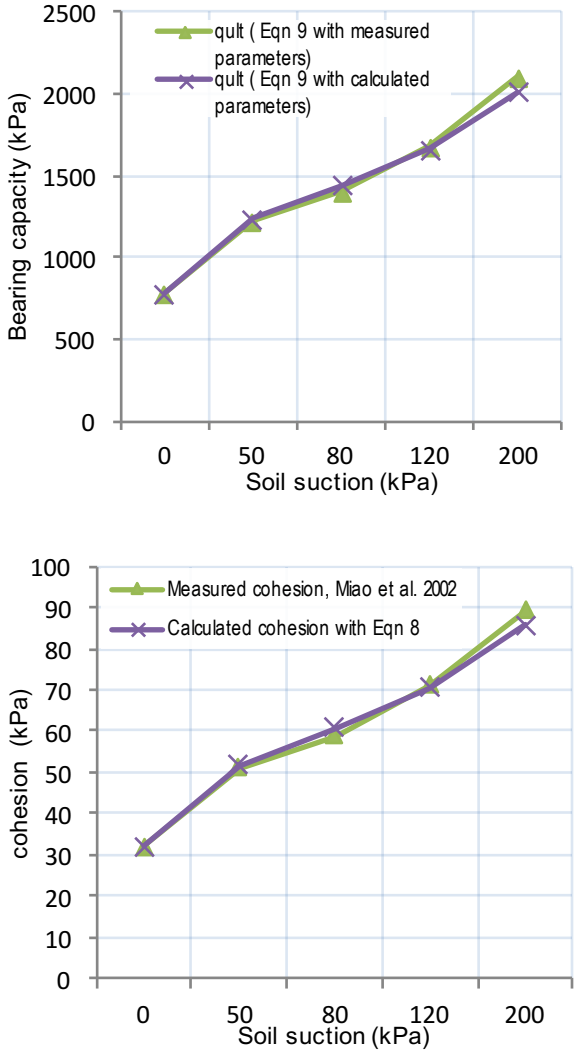

Figure 4. Comparison of calculated bearing capacities and total cohesions with measured values.

Table 5. Comparison of calculated and measured bearing capacities and total cohesions.

Residuel clay (kPa)	0	50	100	200	400
Measured cohesion(c_{total})	14.82	35.24	46.72	69.56	98.32
Calculated cohesion c_{total} ()	14.82	37.6	52.65	74.86	102.91
q_{ult} (bearing capacity, Eqn 9, with measured parameters by Kayadelen et. al. 2007)	403,69	896	1173	1724	2417
q_{ult} (bearing capacity calculated by Eqn 9)	403,69	953	1316	1852	2528

Nanyang expansive soil prepared with predetermined water contents using the static compaction effort. The unsaturated tests are performed by controlling the suction in $u_s = (u_a - u_w)$, = 50, 80, 120 and 200 kPa using unsaturated tri-axial apparatus. The cohesion calculated by Eqn. (8), bearing capacities results using measured / calculated unsaturated parameters (c_{total} , Ø'), by Eqn. 9 are presented in Table 4 and Fig. 4, respectively.

The series of laboratory tests were performed by author (Kayadelen et. al. [9], author in)) using a tri-axial shear test on saturated/unsaturated residual clayey soil, including high contents of semectite and chlorite minerals. The tests were conducted on the undisturbed soil specimens under consolidated and drained conditions. A total of 12 unsaturated tests were performed and axis translation technique, as described by Fredlund and Rahardjo [7], was applied to the specimens. The air-entry value was also calculated by the method proposed by Aubertin et al [20] using %10 and % 60 passing in the grain size distribution chart and the liquid limit. The air-entry value was calculated as 40 kPa, the same as the air-entry value obtained from the experimental SWCC.

The shear strength tests were performed on both saturated and unsaturated soil specimens, which have varying matric suctions ranging from 50 to 400 kPa. The measured cohesion and calculated values with Eqn. (8), bearing capacities results, using measured/calculated unsaturated parameters (ctotal , Ø'), by Eqn. (9 were presented in Table 5 and in Fig. 5, respectively.)

Vanapalli and Fathi [6] performed a number of bearing-capacity tests by means of 100 mm × 100 mm square model footing in test tank by imposing matric suction to compacted coarse-grained soil in the range 0 to 6 kPa. By adjusting the water table level in the test tank, fully saturated and unsaturated conditions of the compacted sand in the test tank were achieved. In the testing program, they measured the bearing capacity of the model footing for 0, 2, 4 and 6 kPa imposed suctions of the foundation soil. They found that a considerable increase in the bearing capacity observed due to the contribution of matric suction for unsaturated condition.

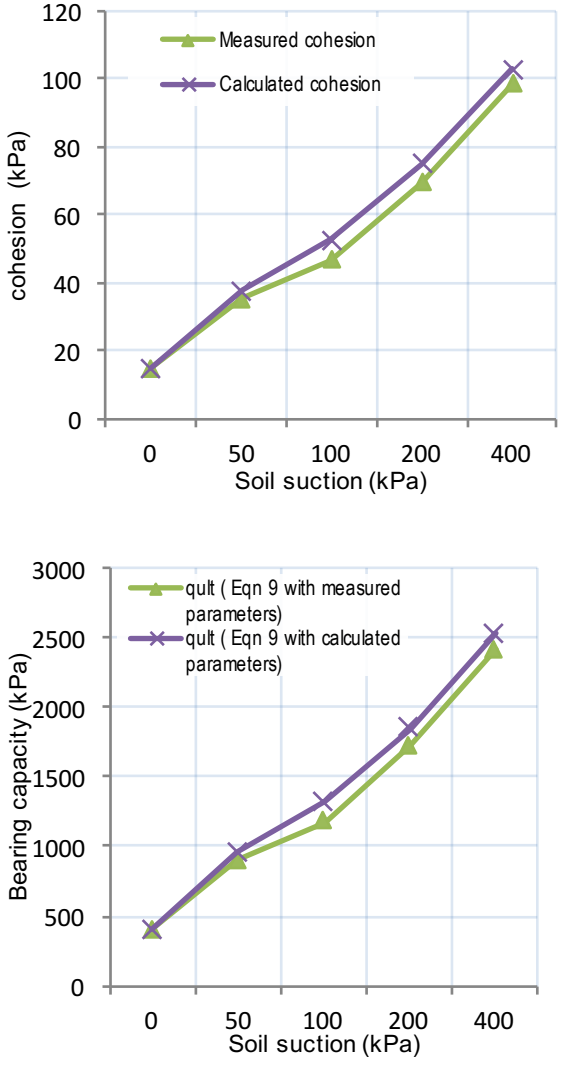

Figure 5. Comparison of calculated bearing capacities and total cohesions with measured values.

The cohesion calculated by Eqn. (8) and bearing capacities by Eqn. (9) are presented in Table 6 and measured/predicted cohesions values are given in Fig. 6

As the total cohesion is examined, it can be seen that it is composed of two parts, which are the effective cohesion (c') and the suction contribution to cohesion

Table 6. Comparison of calculated and measured bearing capacities and total cohesions.

Matric suction (kPa)	0	2	4	6
Calculated cohesion(appearent)	0	1.43	2.83	4.2
$q_{ult,measured}$(model footing by Vanapalli and Fathi (2007))	100	575	700	860
q_{ult} (bearing capacity calculated by Eqn 9)	483	598	710	820

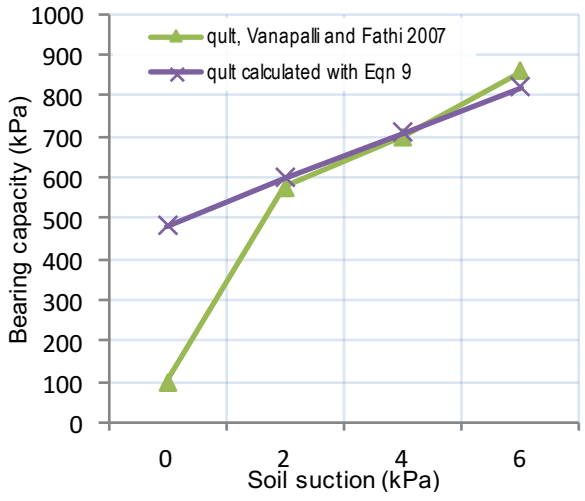

Figure 5. Comparison of calculated bearing capacities and total cohesions with measured values.

$(u_a - u_w)\tan Ø^b$, respectively. Since the effective cohesion for granular soil is approximately null, the second part of the cohesion, which is due to suction, forms the total cohesion and this can also be considered as the apparent cohesion for the granular soil under unsaturated conditions. In contrast to saturated soils, the cohesions calculated herein for the granular soil corresponding to various suction values should be considered in this context.

5 CONCLUSIONS

In this paper a simple technique is proposed for predicting the bearing capacity of unsaturated soils using the saturated shear strength parameters c' and Ø' and the air-entry value (AEV) of the soil for both coarse-and fine-grained soils. Based on the soil's grain size distribution, using several methods, such as the one proposed by Aubertin et al (2003), the AEV can be obtained from the volumetric water-content function with basic soil parameters by %10 and % 60 passing, the void ratio and the liquid limit. Another way to obtain the AEV is to use ready sample functions prepared for different types of soils. Therefore, a quite approximate AEV can be obtained without any complicated test, but only needing simple geotechnical laboratory index tests that are found in everywhere.

The new method proposed here is conceptually in the frame of effective stress approach (ESA). The results of the study indicate that there is a good comparison between the measured and predicted bearing capacity values. Eqn. 9 can also be used to calculate the unsaturated bearing capacity of foundations for practical engineering purposes, provided that we obtain the AEV from the basic soil properties.

Eqn.9 implies that the variations in the bearing capacity for unsaturated soils mainly depend on the total cohesion rather than internal friction angle, since as reported by many earlier researchers, the friction angle does not change noticeably in the unsaturated zone. Therefore, for the unsaturated zone the "total cohesion" and thus the matric suction contribution to the total cohesion become significant on the bearing capacity and it determines the magnitude of bearing capacity. Therefore, it can be said that the nonlinearity in the variation of the bearing capacity with suction is due to similar behaviour in the variation of the cohesion with suction (see Fig. 2 to Fig. 6).

Consequently, this study introduced a method of calculating the bearing capacity of unsaturated soils with a new approach, which only requires one more unsaturated parameter. This study introduced a new, simple method and validates it with various types of materials, but considering the complexity/uncertainty in behaviour of unsaturated soils, the author encourages more experimental works to encompass the method for widespread use.

REFERENCES

[1] Terzaghi, K. 1943. Theoretical soil mechanics. John Wiley and Sons, New York.
[2] Meyerhof, G.G. 1951. The ultimate bearing capacity of foundations. Geotechnique 2, 4, 301–332.

DOI: 10.1680/geot.1951.2.4.301
[3] Steensen-Bach, J.O., Foged, N., Steenfelt, J.S. 1987. Capillary induced stresses – fact or fiction? Ninth ECSMFE, Groundwater Effects in Geotechnical Engineering, Dublin, pp. 83–89.
[4] Oloo, S.Y. 1994. A bearing capacity approach to the design of low volume traffic roads. Ph.D. Thesis, University of Saskatchewan, Canada.
[5] Costa, Y.D., Cintra, J.C., Zornberg, J.G. 2003. Influence of matric suction on the results of plate load tests performed on a lateritic soil deposit. Geotechnical Testing Journal, 26, 2, 219–226. DOI: 10.1520/GTJ11326J
[6] Vanapalli, S.K., Mohamed, F.M.O. 2007. Bearing capacity of model footings in unsaturated soils, In Experimental Unsaturated Soil Mechanics 112, Springer Proceedings in Physics, USA, pp. 483-493. DOI: 10.1007/3-540-69873-6_48
[7] Fredlund, D.G., Rahardjo, H. 1993. Soil mechanics for unsaturated soils, 1st Ed. Wiley, New York.
[8] Oloo, S.Y., Fredlund, D.G., Gan, J.K.M. 1997. Bearing capacity of unpaved roads. Canadian Geotechnical Journal 34, 3, 398–407. DOI: 10.1139/t96-084
[9] Kayadelen, C., Tekinsoy, M. A., Taskiran, T. 2007. Influence of matric suction on shear strength behaviour of a residual clayey soil. Environmental Geotechnics Journal, 53, 891–901. DOI: 10.1007/s00254-007-0701-2
[10] Vanapalli, S.K., Oh, W.T. 2010. Mechanics of unsaturated soils for the design of foundation structures. EMESEG'10 Proceedings of the 3rd WSEAS international conference on Engineering Mechanics Structures, Engineering Geology, Greece, pp. 363-377.
[11] Rojas, J.C., Salinas, L.M., Seja, C. 2007. Plate-load tests on an unsaturated lean clay, In Experimental Unsaturated Soil Mechanics, Vol.112, Springer Proceedings in Physics, USA, pp. 445-452. DOI: 10.1007/3-540-69873-6_44
[12] Schnaid, F., Consoli, N.C., Cumdani, R., Milititsky, J. 1995. Load-settlement response of shallow foundations in structured unsaturated soils, Proceedings of the 1st International Conference on Unsaturated Soils, Paris, pp. 999-1004.
[13] Vanapalli, S.K., Oh, W.T., Puppala, A.J. 2007. Determination of the bearing capacity of unsaturated soils under undrained loading conditions, Proceedings of the 60th Canadian Geotechnical Conference, Ottawa, pp. 1002-1009.
[14] Consoli, N.C., Schnaid, F., Milititsky, J., 1998. Interpretation of plate load tests on residual soil site. Journal of Geotechnical and Geoenvironmental Engineering 124, 9, 857-867. DOI: 10.1061/(ASCE)1090-0241(1998)124:9(857)
[15] Yamamoto, N., Randolph, M.F., Einav, I. 2008. Simple formulas for the response of shallow foundations on compressible sands. International Journal of Geomechanics, ASCE, 8, 4, 230-239. DOI:10.1061/(ASCE)1532-3641(2008)8:4(230)
[16] Skempton, A.W. 1948. The $\varphi_u = 0$ analysis for stability and its theoretical basis. Proceedings of the 2nd International Conference of Soil Mechanics and Foundation Engineering, Rotterdam, pp. 72-77.
[17] Oh, W.T., Vanapalli, S.K. 2009. A simple method to estimate the bearing capacity of unsaturated fine-grained soils. Proceedings of the 62nd Canadian Geotechnical Conference, Halifax, pp. 234-241.
[18] Arya, L.M., Paris, J.F. 1981. A physico-empirical model to predict the soil moisture characteristic from particle size distribution and bulk density data. Soil Science of Society America Journal 45, 1023-1030. DOI:10.2136/sssaj1981.03615995004500060004x
[19] Fredlund, M.D., Fredlund, D.G., Wilson, G.W. 1997. Prediction of the soil-water characteristic curve from the grain-size distribution curve. Proceedings of the 3rd Symposium on Unsaturated Soil, Brazil, pp. 13-23.
[20] Aubertin, M., Mbonimpa, M., Bussière, B., Chapuis, R.P. 2003. A model to predict the water retention curve from basic geotechnical properties. Canadian Geotechnical Journal 40, 6, 1104- 1122. DOI: 10.1139/t03-054
[21] Shoarian Sattari, A., Toker, N.K. 2016. Obtaining soil-water characteristic curves by numerical modelling of drainage in particulate media. Computers and Geotechnics Journal 74, 196- 210. DOI:10.1016/j.compgeo.2016.01.006
[22] Vanapalli, S.K. 1994. Simple test procedure and their interpretation in evaluating the shear strength of unsaturated soils. Ph.D. Thesis, University of Saskatchewan, Saskatoon.
[23] Karube, D. 1988. New concept of effective stress in unsaturated soil and its proving test. In Advanced Triaxial Testing Of Soil And Rock 977, ASTM, USA, pp. 539-552. DOI: 10.1520/STP29097S
[24] Drumright, E.E. 1989. The contribution of matric suction to the shear strength of unsaturated soils. Ph.D. Thesis, Colorado State University, Fort Colins.
[25] Escario, V., Juca, J. 1989. Strength and deformation of partly saturated soils. Proceedings of the 12th International Conference on Soil Mechanics and Foundation Engineering, Rio de Janeiro, pp. 43-46.
[26] Vanapalli, S.K., Fredlund D.G., Pufahal, D.E., Clifton, A.W. 1996. Model for the prediction of shear strength with respect to soil suction.

Canadian Geotechnical Journal 33, 3, 379–392. DOI:10.1139/t96-060

[27] Gan, J.K.M., Rahardjo, H., Fredlund, D.G. 1988. Determination of the shear strength parameters of an unsaturated soil using the direct shear test. Canadian Geotechnical Journal 25, 3, 500–510. DOI:10.1139/t88-055

[28] Miao, L., Liu, S., Lai, Y. 2002. Research of soil–water characteristics and shear strength features of nanyang expansive soil. Engineering Geology 65, 4, 261–267. DOI:10.1016/S0013-7952(01)00136-3

POENOSTAVLJENI PRISTOP K OCENJEVANJU VPLIVA ENEGA PILOTA NA PORAZDELITEV NAPETOSTI V TLEH

Ping Li
Hohai University,
210098, Nanjing, Ljudska republika Kitajska

Tao Yu *(vodilni avtor)*
Hohai University,
210098, Nanjing, Ljudska republika Kitajska
E-pošta: yutaohhu@163.com

Dongdong Zhang *(vodilni avtor)*
PLA University of Science and Technology,
Nanjing 210007, Ljudska republika Kitajska
E-pošta: zhangdodo_163@163.com

Ključne besede

analitična rešitev, razporeditev napetosti v tleh, trenje na plašču; nosilnost noge

Izvleček

Članek prikazuje poenostavljeno analitično rešitev za ocenjevanje porazdelitve napetosti v tleh v odvisnosti od dimenzije posameznega pilota. Eksponentno naraščajoče mejno trenje vzdolž plašča je izračunano s pomočjo ravnovesne analize elementa tal, ki obdaja pilot. Predlagana sta porazdelitev napetosti v tleh zaradi eksponentno naraščajočega trenja na plašču pilota in enakomerno porazdeljena nosilnost osnove pilotov. Primerjava tako ocenjene napetosti v tleh z izvirno rešitvijo Geddesa je potrdila veljavnost podanih izpeljav in dobljenih enačb.

A SIMPLIFIED APPROACH TO ESTIMATING THE SOIL STRESS DISTRIBUTION DUE TO A SINGLE PILE

Ping Li
Hohai University,
210098, Nanjing, PR China

Tao Yu *(corresponding author)*
Hohai University,
210098, Nanjing, PR China
E-mail: yutaohhu@163.com

Dongdong Zhang *(corresponding author)*
PLA University of Science and Technology,
Nanjing 210007, PR China
E-mail: zhangdodo_163@163.com

Keywords

analytical solution; soil stress distribution; skin friction; end bearing

Abstract

This paper reports a simplified analytical solution for estimating the soil stress distribution due to pile dependence on the pile dimensions. The exponentially increasing ultimate skin friction along the pile shaft is derived by means of an equilibrium analysis of the soil element around the pile. The soil stress distribution due to the exponentially increasing skin friction and uniformly distributed end bearing of the piles is proposed. The estimated soil stresses are compared using the original Geddes solution, which validates the derivation and formulae obtained.

1 INTRODUCTION

The Boussinesq solution [1] is normally used to estimate the soil stress distribution due to a vertical point load applied to the ground surface. It proposes that the ground is a semi-infinite, elastic, isotropic and homogeneous medium that obeys Hooke's law. Through integration, the stress distribution induced by any type of external vertical load can be obtained. Thus, the ground surface settlement can be calculated using a layer-wise summation. However, there are many cases in which the vertical loads are applied not to the ground surface, but to the interior of a semi-infinite medium, i.e., the stress condition during excavation and in deep foundations. Problems based on these conditions cannot be solved using the Boussinesq method. Mindlin [2] carried out some theoretical analyses based on Boussinesq's assumption to estimate the stress induced by an internal point load applied to positions in an isotropic, homogeneous, elastic half-space. Because the stress distribution due to an internal point load can be obtained using this approach, the stress due to any type of internal loading (i.e., increments varying linearly, uniform with circular and rectangular distributions), can also be calculated by integration.

Based on an ideal elastic soil mass assumption, the Mindlin solution has been widely used to analyze the behavior of pile foundations, such as Geddes [3], Seed and Reese [4], D' Appolonia and Romualdi [5], Coyle and Reese [6], Poulos and Davis [7], Ramiah and Chickanagappa [8], Clancy and Randolph [9], Horikoshi and Randolph [10], and Kitiyodom and Matsumoto [11]. Based on the Mindlin solution, some load-transfer mechanisms of inclusion were reported by Luk&Keer [12] and Selvadurai & Rajapakse [13]. Suriyamongkal et al. [14] investigated the stress distribution in soil induced by piles under a vertical applied load in order to develop the radial ring forces and vertical forces acting on the interior of a half space. The soil stress for pile

foundations has been analyzed by Geddes [3] based on the Mindlin solution, in which the end bearing (EB) of the pile foundation is assumed to be a point load on the center of the cross-section of the pile toe, and the skin friction (SF) is modeled as a line load distributed along the vertical axis of the pile shaft. Due to the complexity of the integral equation and the limited computer availability, the solution was used in practice up until approximately 1966. Geddes [15] reported tabulated values (m and n) of the stress coefficients that were defined as the relevant stress value simply multiplied by H^2/P to determine one of the stress components at a point, where H is the pile length and P is the applied load, and they were widely used in practice. However, Wang & Pan reported [15, 16] that the Geddes solution does not account for the cross-sectional geometry and dimensions because the distance between the calculated position and the point load does not vary with these factors. This simplification causes some errors, particularly for non-circular piles by Lv et al [17] and Zhang et al.[18] and for circular piles with large cross-sectional diameters. In addition, the skin friction is ideally simplified as a uniform and/or linear variation along the pile shaft, as reported by Wang et al. [19].

This paper modifies the assumptions of the Geddes solution so that the skin friction is distributed on the external surface of the pile shaft and the end bearing is uniformly distributed on the pile toe. The skin friction is derived via equivalent analyses. Analytical solutions are derived by considering the effects of the pile dimensions, and are calculated using MATLAB software.

2 BASIC ASSUMPTIONS

There are four basic assumptions: (1) the construction effects on piles are not considered; (2) the ground is assumed to be a semi-infinite, isotropic and homogeneous medium; (3) the skin friction is distributed on the external surface of the pile shafts and the end bearing is uniformly distributed on the pile toes; and (4) the ultimate skin friction is exponentially increased with the pile depth. The technique of this analytical solution is illustrated by Figure 1. The soil stress at the point (r_j, α_j) is governed by the distance between the position of (r_j, α_j) to the position of the skin friction and the end bearing. In the Geddes solution, this distance is r, which is constant for piles with different diameters. In this analytical solution, this distance is r', which varies with (r_i, α_i), i.e., the pile dimension. The stress distributions due to the skin friction and the end bearing can be analyzed using the normalized stress coefficient by multiplying the relevant stress and H^2/P.

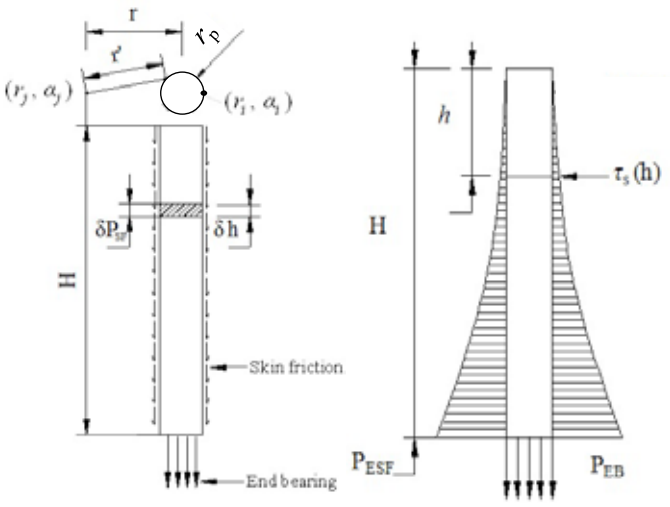

Figure 1. Graphical representation of the technique for the exponentially increased skin friction and the uniformly distributed end bearings.

3 DERIVATION PROCEDURES

Under ideal conditions, the effective vertical stress of the semi-infinite ground (σ_v') at depth z is $\sigma_v' = \gamma' z$, where γ' is the effective unit weight of the soil. However, due to the existence of piles, the ground is influenced by vertical shearing effects at the pile-soil interfaces. The free bodies of a soil element adjacent to the pile shafts are equivalently analyzed, as shown in Figure 2.

According to the theory of the vertical shearing mechanism, the skin friction on the pile surface,τ_s , is not entirely equal to the shear stress on the free body of

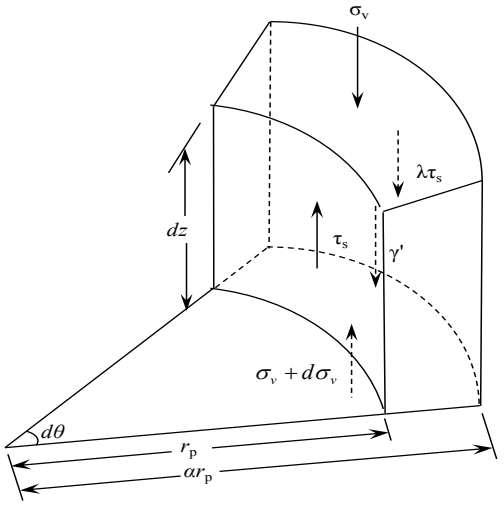

Figure 2. Equilibrium analysis.

the soil element. For a circular pile with a diameter of r_p, the influencing zone of the skin friction is αr_p. The ratio of the shear stress, $\lambda\tau_s$, to the skin friction is λ. The equilibrium equation of the free body was derived from σ_v', τ_s, and $\lambda\tau_s$ as follows:

$$\frac{\mathrm{d}\sigma_{\mathrm{v}}'}{\mathrm{d}z}=\frac{2\eta K\sigma_{\mathrm{v}}'\tan\delta}{r_{\mathrm{p}}}+\gamma' \qquad (1)$$

$$\eta=\frac{\alpha\lambda-1}{\alpha^2-1} \qquad (2)$$

where K denotes the coefficient of earth pressure at rest. In this analysis, the interactions between the adjacent free bodies are taken as the internal force of a soil element. The top and the bottom areas of the free body are

$$A_{\mathrm{top}}=A_{\mathrm{bottom}}=(\alpha^2-1)r_{\mathrm{p}}^2\mathrm{d}\theta/2 \qquad (3)$$

The inner surface area of the free body is

$$A_{\mathrm{inner}}=\gamma_{\mathrm{p}}\mathrm{d}\theta\mathrm{d}z \qquad (4)$$

The outer surface area of the free body is

$$A_{\mathrm{outer}}=\alpha\gamma_{\mathrm{p}}\mathrm{d}\theta\mathrm{d}z \qquad \textbf{(5)}$$

It is assumed that the local shaft friction at failure, τ_s, is governed by the Coulomb equation according to Lehane et al.[20]:

$$\tau_s=c'+K\sigma_v'\tan\delta \qquad (6)$$

where δ is the friction angle of the pile-soil interface. The effective cohesion (c') is not considered in general. The integration of Eq.1 and the incorporation of the boundary condition yields

$$\sigma_{\mathrm{v}}'=\frac{r_{\mathrm{p}}\gamma'}{2\eta K\tan\delta}\left(\mathrm{e}^{\frac{2\eta K\tan\delta}{r_{\mathrm{p}}}z}-1\right) \qquad (7)$$

The parameters K and δ remain constant along the pile length at the ultimate stress state. Therefore, the ultimate skin friction on the pile surfaces, τ_s, is obtained by

$$\tau_{\mathrm{s}}=K\sigma_{\mathrm{v}}'\tan\delta=\frac{r_{\mathrm{p}}\gamma'}{2\eta}\left(\mathrm{e}^{\frac{2\eta K\tan\delta}{r_{\mathrm{p}}}z}-1\right) \qquad (8)$$

After the integration of Eq. (8) on the pile surface, the total force due to an external skin friction is obtained by

$$P_{ESF}=\frac{\pi r_{\mathrm{p}}^2\gamma'}{\eta}\left[\frac{r_{\mathrm{p}}\left(\mathrm{e}^{\frac{2\eta K\tan\delta}{r_{\mathrm{p}}}z}-1\right)}{2\eta K\tan\delta}-z\right] \qquad (9)$$

The skin friction on the pile surfaces over a normalized depth δh is $\delta P_{ESF}=\int\tau_s ds\delta h$. The normalized soil stress H^2/P_{ESF} at any position due to the exponentially increased skin friction is given by

$$I_{ESF}=\frac{H^2}{P_{ESF}}\int_0^H\int_l\tau_s\sigma_z dsdh \qquad (10)$$

where I_{ESF} is the normalized soil stress due to the exponentially increased skin friction; l denotes the pile perimeter; P_{ESF} is the total force due to the external skin friction, which is determined by Eq. (9); σ_z is the stress at any given position M(x, y, z) due to an internal point load P(0, 0, h), which is obtained by Mindlin [2]

$$\sigma_z=\frac{P}{8\pi(1-\mu)}\left[\frac{(1-2\mu)(z-h)}{R_1^3}-\frac{(1-2\mu)(z-h)}{R_2^3}+\frac{3(z-h)^3}{R_1^5}+\frac{30hz(z+h)^3}{R_2^7}+\frac{3z(3-4\mu)(z+h)^2-3h(z+h)(5z-h)}{R_2^5}\right] \qquad (11)$$

where μ is the Poisson ratio, $R_1=\sqrt{x^2+y^2+(z-h)^2}$ and $R_2=\sqrt{x^2+y^2+(z+h)^2}$.

The end bearing over the normalized cross-sectional area δA is $\delta_{PEB}=(P_{EB}/A)\delta A$. The normalized soil stress H^2/P_{EB} at any position due to the end-bearing pressure is given by

$$I_{EB}=\frac{H^2}{P_{EB}}\iint_A\frac{P_{EB}}{A}\sigma_z dxdy \qquad (12)$$

where I_{EB} is the normalized soil stress due to the end-bearing pressure; A denotes the cross-sectional area of the piles.

4 COMPARISONS AND ANALYSES

In a comparison of the differences between the Geddes's solution and this analytical solution, Figures 3a and 3b show the calculated normalized soil stress due to skin friction and the end bearing using these two methods, respectively. The subject is a circular pile with a diameter of r_p= 2.0 m. The soil column 3 m away from the vertical axis of the pile shaft is chosen for the analysis, i.e., r = 3 m.

It is found that the soil stress due to the skin friction estimated using this analytical solution is smaller than that of the Geddes solution. The differences are the result of two factors: first, the skin friction in the Geddes solution is assumed to be located at the vertical axis of the pile shaft, but the skin friction in this analytical solution

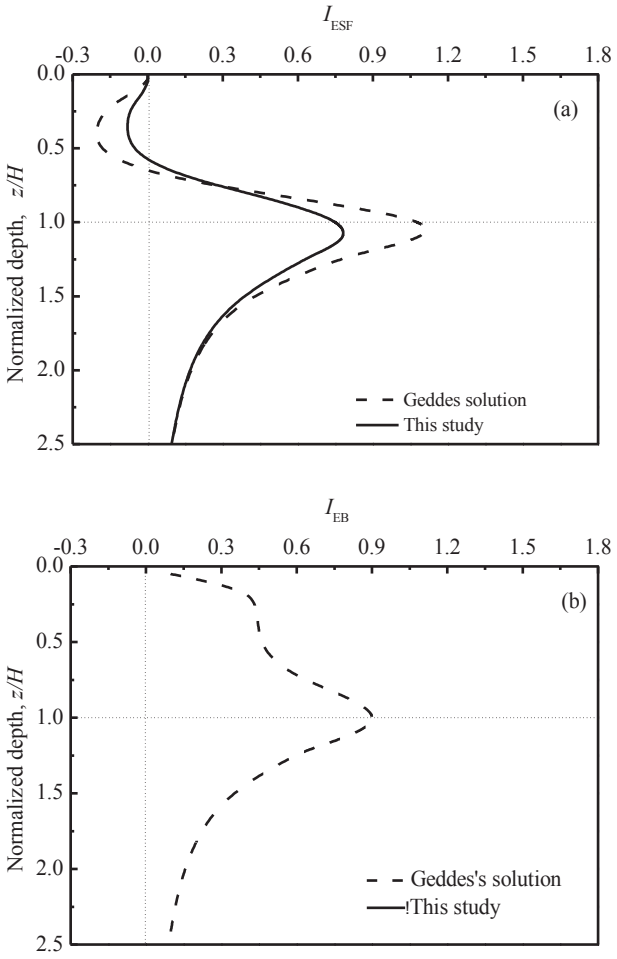

Figure 3. Calculated normalized soil stress due to (a) skin friction and (b) end bearing.

distributes on the pile surface; second, the skin friction in the Geddes solution is assumed to be a linear variation along the depth, but the skin friction in this analytical solution exponentially increases with the pile depth. For the elastic ground, since the skin friction increases along the pile shaft, there are negative values that can be ignored, meaning the extension is in the surrounding soil. Below the pile toe, the soil stress decreases with depth, indicating the elimination of skin friction effects.

However, the soil stress due to the end bearing estimated using this analytical solution is larger than that of the Geddes solution. This difference is mainly caused by the simplification of the end bearing in the Geddes solution. It assumes that the end bearing is a point load acting on the center of the pile toe. However, in this analytical solution, the end bearing is assumed to be uniform load acting on the pile toe. The similar trend of soil stress estimated using these two methods improves the reasonability of this analytical solution.

5 CONCLUSIONS

This paper modifies the assumptions of the Geddes solution that the skin friction is distributed on the external surface of the pile shaft and the end bearing is uniformly distributed on the pile toe. The skin friction is derived by means of an equilibrium analysis on the soil element around the pile shaft, obtaining an exponentially increasing skin friction along the pile shaft. Then, an analytical solution, dependent on the pile dimension, for estimating the soil stress distribution due to an exponentially increasing skin friction and the uniformly distributed end bearing of piles is presented. The calculated soil stresses are compared using the original Geddes solution, which validates the derivation and formulae obtained. It is found that the soil stress due to exponentially increasing skin friction using this analytical solution is smaller than that due to the linearly increased skin friction using the Geddes solution. In addition, the soil stress due to the uniform end bearing using this analytical solution is larger than that caused by the point end bearing using the Geddes solution.

Acknowledgment

The authors wish to thank the National Science Foundation of China (No.51408187, 51408607), the Natural Science Foundation of Jiangsu Province, China (No. BK20140850, BK20171399), and the China Postdoctoral Science Foundation Grant (No. 2016M592932).

REFERENCES

[1] Boussinesq, J. 1885. Application des potentiels: à l'étude de l'équilibreet du mouvement des solid esélastiques. Gauthier-Villard, Paris.
[2] Mindlin, R.D. 1936. Force at a point in the interior of a semi-infinite solid. Physics 7, 195-202.
[3] Geddes, J.D. 1953.The bearing capacity of piles. Thesis, London, UK: University of Durham.
[4] Seed, H.B., Reese, L.C. 2004. The action of soft clay along friction piles. American Society of Civil Engineers Transactions (ASCE) 122, 731-764.
[5] D'Appolonia, E., Romualdi, J.P. 1963. Load transfer in end-bearing steel H-piles. Proc. ASCE 89, SM2, l-25.
[6] Coyle, H.M., Reese, L.C. 1966. Load transfer for axially loaded piles in clay. J. Soil Mech. Fdns. Div. Am. Sot. Civ. Eng. 92, SM2, l-26.
[7] Poulos, H.G., Davis, E.H. 1968. The settlement behaviour of single axially loaded incompressible

piles and piers. Geotechnique 18, 3, 351-371. DOI: https://doi.org/10.1680/geot.1968.18.3.351

[8] Ramiah, B.K., Chickanagappa, L.S. 1978. Stress distribution around batter piles. Journal of the Geotechnical Engineering Division (ASCE) 104, 229–247.

[9] Clancy, P., Randolph, M.F. 1993. An approximate analysis procedure for piled raft foundations. International Journal for Numerical and Analytical Methods in Geomechanics 17, 849-869. DOI: 10.1002/nag.1610171203

[10] Horikoshi, K., Randolph, M.F. 1999. Estimation of overall settlement of piled rafts. Soils and Foundations 39, 2, 59–68. DOI: http://doi.org/10.3208/sandf.39.2_59

[11] Kitiyodom, P., Matsumoto, T. 2002. A simplified analysis for piled raft and pile group foundations with batter piles. International Journal for Numerical and Analytical Methods in Geomechanics 26, 1349–1369. DOI: 10.1002/nag.248

[12] Luk, V.K., Keer, L.M. 1979. Stress analysis for an elastic half space containing an axially-loaded rigid cylindrical rod. International Journal of Solids Structures 15, 805-827. DOI: https://doi.org/10.1016/0020-7683(79)90006-4

[13] Selvadurai, A.P.S., Rajapakse, R.K.N.D. 1985. On the load transfer from a rigid cylindrical inclusion into an elastic half space. International Journal of Solids Structures 21, 12, 1213-1229. DOI: https://doi.org/10.1016/0020-7683(85)90005-8

[14] Suriyamongkal, S., Karasudhi, P., Lee, S.L. 1973. Axially Loaded Rigid Cylindrical Body Embedded in an Elastic Half-Space. 13th Midwestern Mechanics Conference, 333-347.

[15] Geddes, J.D. 1966.Stresses in Foundation Soils Due to Vertical Subsurface Loading. Geotechnique 16, 3, 231-255. DOI: https://doi.org/10.1680/geot.1966.16.3.231

[16] Wang, C.D., Pan, E. 2004. Stresses due to vertical subsurface loading for an inhomogeneous cross-anisotropic half-space. International Journal for Numerical and Analytical Methods in Geomechanics 28, 12, 1233–55. DOI: 10.1002/nag.385

[17] Lv, Y.R., Liu, H.L., Ng, C.W.W., Gunawan, A., Ding, X.M. 2014. A modified analytical solution of soil stress distribution for XCC pile foundations. Acta Geotechnica 9, 3, 529-546. DOI: 10.1007/s11440-013-0280-1

[18] Zhang, D.D., Lv, Y.R., Liu, H.L., Wang, M.Y. 2015. An analytical solution for load transfer mechanism of XCC pile foundations. Computers and Geotechnics 67, 2015, 223-228. DOI: https://doi.org/10.1016/j.compgeo.2015.03.006

[19] Wang, Y., Lv, Y.R., Zhang, D.D., Zhou, J.Y. 2016. A Fundamental Study of the Performance of X-Section Cast-in-Place Concrete Single Piles. Acta Geotechnica Slovenica 13, 1.

[20] Lehane, B.M., Jardine, R.J., Bond, A.J. 1993. Mechanisms of shaft friction in sand from instrumented pile tests. ASCE Journal of Geotechnical Engineering 119, 1, 19-35.

UČINKI ZNAČILNOSTI DELCEV NA STRIŽNO TRDNOST APNENČASTIH PESKOV

Pham Huu Ha Giang *(vodilni avtor)*
Ghent University,
Department of Civil Engineering
905 B-9052 Zwijnaarde, Belgija
E-pošta: huuhagiang.pham@ugent.be

Can Tho University,
Department of Civil Engineering
3-2 Street, Can Tho, Vietnam
E-mail: phhgiang@ctu.edu.vn

P. O. Van Impe
Department of Geotechnical Eng. at JDN - Jan De Nul Group
Tragel 60, 9308 Hofstade-Aalst, Belgija

W. F. Van Impe
Ghent University,
Department of Civil Engineering
905 B-9052 Zwijnaarde, Belgija

Patrick Menge
Dredging International
Scheldedijk 30, 2070 Zwijndrecht, Belgija

Veerle Cnudde
Ghent University,
Department of Geology and Soil Science
Krijgslaan 281, S8 9000, Gent, Belgija

Wim Haegeman
Ghent University,
Department of Civil Engineering
905 B-9052 Zwijnaarde, Belgija

Ključne besede

strižna trdnost, sferičnost, oblika delcev, apnenčasti pesek

Izvleček

V prispevku je prikazana 3D analiza za določitev oblike in velikosti delcev kremenčevih in apnenčastih peskov. Ugotovili smo, da so delci apnenčastega peska manj sferični od kremenčevih in zdrobljenih apnenčastih peskov. Poleg tega rezultati kažejo, da je povprečna sferičnost (SPH) inverzno proporcionalna z velikostjo delcev. Vseeno pa imajo v vsakem vzorcu večji delci višje vrednosti SPH kot manjši delci. Poleg tega 3D analiza daje manjše delce kot sejalna analiza (SA). Zaradi različnih oblik delcev, ki povzročajo povezovanje delcev, velja zlasti za apnenčast pesek, da delci ne morejo skozi sita s svojo najkrajšo dimenzijo. V članku so obravnavani učinki značilnosti delcev na lastnosti strižne trdnosti. Čeprav apnenčast pesek kaže višje vrhnje in residualne vrednosti parametrov strižne trdnosti, doseže pri majhni strižni specifični deformaciji nižjo strižno trdnost in nižjo dilatacijo kot kremenčev pesek. Poleg tega ugotovitve dokazujejo, da residualna strižna trdnost narašča s srednjo velikostjo delcev. Vzorec z manjšimi delci kaže manj dilatacije pri nizki vertikalni napetosti, medtem ko visoka vertikalna napetost povzroči manjšo kompresijo. Zveza med obliko delcev in lastnostmi strižne trdnosti je obravnavana na podlagi rezultatov 3D analize.

EFFECTS OF PARTICLE CHARACTERISTICS ON THE SHEAR STRENGTH OF CALCAREOUS SAND

Pham Huu Ha Giang *(corresponding author)*
Ghent University,
Department of Civil Engineering
905 B-9052 Zwijnaarde, Belgium
E-mail: huuhagiang.pham@ugent.be

Can Tho University,
Department of Civil Engineering
3-2 Street, Can Tho, Viet Nam
E-mail: phhgiang@ctu.edu.vn

P. O. Van Impe
Department of Geotechnical Eng. at JDN - Jan De Nul Group
Tragel 60, 9308 Hofstade-Aalst, Belgium

W. F. Van Impe
Ghent University,
Department of Civil Engineering
905 B-9052 Zwijnaarde, Belgium

Patrick Menge
Dredging International
Scheldedijk 30, 2070 Zwijndrecht, Belgium

Veerle Cnudde
Ghent University,
Department of Geology and Soil Science
Krijgslaan 281, S8 9000, Gent, Belgium

Wim Haegeman
Ghent University,
Department of Civil Engineering
905 B-9052 Zwijnaarde, Belgium

Keywords
shear strength, sphericity, particle shape, calcareous sand

Abstract

The paper presents a 3D analysis (3DA) to evaluate the particle shape and size of silica and calcareous sands. The particles of calcareous sand are found to be less spherical than those of silica and crushed calcareous sands. Furthermore, the results indicate that the average sphericity (SPH) holds an inverse relationship to the particle size. However, in each sample the larger particles have higher SPHs than the smaller particles. In addition, the 3DA yields smaller particles than the sieve analysis (SA). Owing to a variety of particle shapes, causing particle interlocking, especially for calcareous sand, the particles cannot pass through the sieves by their shortest dimension. This paper discusses the effects of particle characteristics on the shear strength properties. Although the calcareous sand shows higher peak and residual shear strength properties, it tends to reach a lower shear strength at a small shear strain and a lower dilation than the silica sand. Moreover, the findings prove that the residual shear strength increases with the mean particle size. The sample with smaller particles shows less dilation under low vertical stress, while high vertical stress yields less compression. The relationship between the particle shape and shear strength properties is discussed based on the 3DA results.

1 INTRODUCTION

Particle characteristics (shape and size) are very important parameters affecting the shear strength properties. The determination of these shear strength properties requires expensive laboratory testing, so correlations between shear strength properties and particle characteristics can become more meaningful for both the design and construction of soil foundations. In particular, for calcareous sands, the collection of representative samples for the field conditions is much more difficult. Almost all measured soil parameters do not reflect the exact soil state prior to seismic loading. Under these conditions, a change in the grain characteristics might occur in calcareous sands. The skeletal particles of calcareous sands are varied and diverse in their size, shape and ability to resist mechanical and chemical effects. They are very angular [1–3] and exist at a higher void ratio than silica sands [4–7].

In previous studies on granular soils, it is observed that the relationship between sphericity (SPH) and particle size is not evident in previous studies. For silica sands, the larger particles are the most spherical [8, 9]. However, the results for different types of material and the database of previous studies show that no unique relationship exists between grain size and grain shape [4, 10, 11].

Recently, Dewen et al. [12] confirmed an increase in SPH with decreasing particle size for beach sands.

To measure and quantify particle shape, a two-dimensional (2D) microscopic method is commonly used, not only to directly evaluate the roundness of the particle, but also to estimate the form of the particle based on visual 2D plane imaging. In the 2D method, the thickness of the particle is estimated by the shadow projection of the particle. Compared to a three-dimensional (3D) method, the 2D method has some disadvantages. For sample selection, handling fine particles one by one is very time consuming, particles are handled randomly and particle spacing is often not sufficient to allow a clear shadow between adjacent particles. Therefore, the result of the 2D analysis is dependent on the arrangement of particles to capture 2D images. Although the 2D method can provide particle morphology, it can underestimate the true SPH of the particles [13]. Moreover, owing to the variation in particle shape, the use of roundness charts for silica sands based on 2D plane images cannot be used to determine the roundness for calcareous sands. Indeed, the 2D method is more applicable to grains where the longest and intermediate axes of particles can be easily presented parallel to the surface, whereas the shortest axis is perpendicular. In recent years, some techniques have been developed to identify particle morphology in 3D, such as automated serial sectioning tomography (a practical way to rebuild the 3D image from a succession of 2D ones), scanning transmission electron microscopy tomography using electron beams instead of X-ray, and X-ray computed tomography.

The influence of grain size distribution (GSD) on the shear strengths of soils shows that well-graded sand gives a higher shear strength than uniformly graded sand [14, 15]. The shear strength increases due to gradation broadening. This effect is examined by the void ratio decrease as the range of particle sizes increases [16]. Currently, there is still no consensus regarding the effect of morphology (shape and size) causing an increase or decrease in the shear strength properties of silica sands. Several studies reported that the particle size gave no significant difference in the shear strength [16, 17]. In contrast, other studies [18–20] revealed that the increase in particle size led to an increase in the shear strength. In addition, flaky and angular particles are found to increase the shear resistance [16, 21]. Kara [22] also showed that the peak friction angle increased with an increasing particle size, but there was no significant impact of the particle size on the residual friction angle at the critical state. Furthermore, Vangla et al. [23] found that the particle size had no influence on the peak friction angle, but affected the residual friction angles.

Compared to silica sands, calcareous sands are found to show greater shear strength properties [1, 3, 24–26] and a dilative behavior at low relative densities [2]. This behavior reflects the greater interlocking in calcareous sand due to the effect of particle shape. Indeed, the angular and less spherical particles do not move around each other easily, causing an increase in the dilation compared with smooth and rounded particles. The limited rotation and movement of the particles result in an increase in the inter-particle contact and, consequently, the shear strength [3, 27]. In addition, it is clear that the differences in mineral composition and gradation between silica and calcareous sands cause the difference in the shear strength properties. Previous studies also show the specific gravities of calcareous sands greater than 2.7 and larger than those of silica sands (approximately 2.65). Additionally, silica sands are generally a uniform grade, whereas the particles of calcareous sands are very angular and vary in size and shape, producing well-graded distribution curves. In conclusion, the current results of particle characteristics correlated to the shear strength properties are limited, especially for calcareous sands.

In this study, 3D particle measurements and analyses based on the data collected using X-ray micro-computed tomography (X-ray CT) are performed on three fractions of particles of a calcareous sand to determine the particle size and shape. The particle size and shape indices such as the Corey shape index (CSI), disc-rod index (DRI) and true SPH of each fraction are presented. For comparison, 3D particle tests are also performed on the same fractions of particles of the crushed calcareous sand and a silica sand. Finally, the shear behavior of the calcareous sand is investigated and correlated to the particle sphericity for calcareous sands.

2 MATERIALS & METHODOLOGY

2.1 Materials

The tests are initially performed on two types of sands. The calcareous sand, Sarb sand (S), used in this study is obtained from an artificial island in Abu Dhabi, while Mol sand (silica sand) is taken from Antwerpen, Belgium.

The purpose of this study is also to determine the effect of crushing on the particle shape. Therefore, the S sand is crushed under two loading conditions (dynamic and static loadings). Thus, the dynamic crushing method using a vibrating table in accordance with ASTM D4253 [28] is selected because it yields much more crushed particles. New particles produced by S sand under

Table 1. Physical properties of the studied materials.

Physical properties	Mol	SMol	VS	S	S2	S3	S4	S5	S6
Specific gravity, G_s	2.637	2.787	2.787	2.787	2.787	2.787	2.787	2.787	2.787
Mean grain size, D_{50} (mm)	0.167	0.167	0.425	0.73	0.205	0.408	0.565	0.815	1.135
Uniformity coefficient, C_u	1.44	1.44	5.429	3.46	-	-	-	-	-
Coefficient of curvature C_c	0.93	0.930	0.809	1.12	-	-	-	-	-
Maximum void ratio, e_{max}	0.93	1.340	0.956	1.33	1.376	1.435	1.556	1.752	1.835
Minimum void ratio, e_{min}	0.581	0.843	0.508	0.903	0.933	0.973	1.042	1.172	1.224
Maximum dry density, $\rho_{d(max)}$ (g/cm^3)	1.668	1.512	1.848	1.464	1.441	1.412	1.365	1.283	1.253
Minimum dry density, $\rho_{d(min)}$ (g/cm^3)	1.366	1.191	1.425	1.196	1.173	1.144	1.09	1.013	0.983

dynamic loading are called VS sand. Following this, S, VS and Mol sands are sieved to separate every fraction of particles and to remove particles larger than 4 mm. In addition, S sand particles are then used to match the grain size distribution (GSD) of the Mol sand, called SMol, to investigate the effect of the different material with the same C_u on the shear strength properties.

For the 3D scan, each sample is prepared by collecting the particles of the fraction obtained from the sieve. The following fractions of the three sands (Mol, S, VS) are selected for scanning: No. 90: 160-250 μm (Mol and S2), No. 35: 500-630 μm (S4 and VS4) and No. 18: 1-1.25 mm (S6 and VS6). The physical properties of the studied sands and fractions of S (S2, S3, S4, S5, S6) and VS (VS4, VS6) sands are summarized in Table 1 and the grain size distribution (GSD) curves are shown in Figure 1.

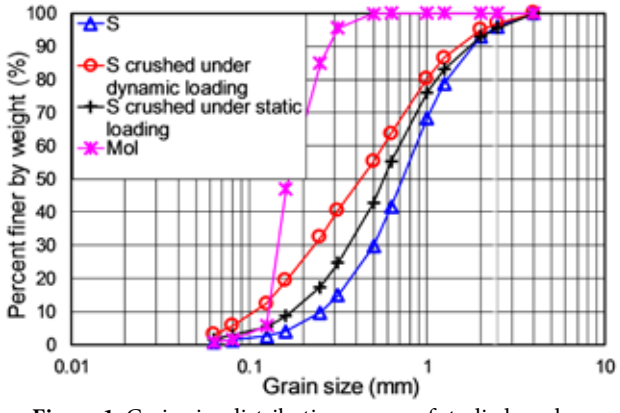

Figure 1. Grain size distribution curves of studied sands.

2.2 Methodology

3D particle evaluation and direct shear tests are performed in this study. The procedure of the 3D measurement and analysis consists of a scanner operation, tomographic reconstruction, 3D analysis (3DA) and visualization. The scanner operation is performed at the Center for X-Ray Tomography at Ghent University (UGCT). The whole system includes hardware for scanning and data acquisition and software tools for reconstructing radiographs and 3D visualization. These are briefly described below.

2.2.1 X-ray computed tomography

X-ray CT is a non-destructive technique to visualize the internal structure of objects and obtain 3D information regarding their shape. The X-ray CT device used in this study is a high-resolution X-ray CT (HRXCT) scanner developed by Masschaele et al. (2007) [29] at UGCT. Normally, an X-ray CT scanner includes an X-ray source and an X-ray detector connected to a computer. Unlike medical scanners, the source-detector is fixed, while the object, which is placed on a rotary stage (rotation angles from 0° to 360°) between the source and the detector, is rotated during scanning.

2.2.2 Octopus software

The software, Octopus (formerly known as Morpho+), is based on several algorithms and was developed in-house by Vlassenbroeck et al. (2007) [30] at UGCT. Octopus allows a determination of the porosity and the volume fraction of a component in the dataset [31]. Over the past few years, the program has been modified and extended to meet user demands and is now upgraded continuously. There are two separate packages to collect 3D information, the Octopus Analysis package and the Octopus Visualization package. The results of each step in the Octopus Analysis are shown in 2D, and Octopus Visualization is used to turn the analysis dataset 2D into a 3D view.

In order to evaluate the particle size, the maximum opening (MO) and minimum closing (MC) are calculated for each particle. MO is defined as the diameter

of the largest inscribed sphere in an object and MC is the diameter of the smallest circumscribed sphere in an object. The MO and MC of a particle are shown in Figure 2a. In the figure, MO is the lower limit for an object to pass through a virtual sieve mesh, while MC is used to determine the upper limit. For measuring the particle SPH, the equivalent diameter is defined as the diameter of a sphere with the number of voxels inside an object, and then the SPH of the object is calculated as the ratio of the MO to the equivalent diameter. In addition, an equivalent ellipsoid with the same moments of inertia as the object is used to calculate the disc-rod index and the shape index.

The analysis results are plotted on a diagram proposed by Illenberger [32] in which the Corey shape index (*CSI* defined as $S/(IL)^{1/2}$) is plotted against the disc-rod index ($DRI=(L-I)/(L-S)$) (L, I and S denote the longest, intermediate and shortest lengths of the particle, respectively). Illenberger's diagram delineates the areas for different types of shapes, including sphere, compact disc, compact blade, compact rod, disc, blade, rod, extreme disc, extreme blade, and extreme rod, as shown in Figure 3.

2.2.3 3D analysis

After acquiring the radiographs covering 360°, the tomographic reconstruction phase is processed to create 2D slices registered as 16-bit images by using the reconstruction software Octopus package. In the reconstruction phase, the obtained 2D projections are transformed into cross-sections through the sample using a filtered back algorithm. In the 3DA, the sample is expressed as a volume of voxels (3D pixels). The flowchart for the 3D particle analysis consists of loading the volume, filtering, thresholding, filling holes, labeling, distance map, object separation and rejoining, as demonstrated in Figure 2b. First, all the 2D slices obtained from the reconstruction volume are loaded into the computer memory. In this step, several parameters can be changed, such as the circular region of interest, the scale of data (16bit, 8bit) and the size calibration (voxel retrieved in μm). In the second step, i.e., filtering, the noise is removed using a bilateral filter (an extension of the Gaussian filter) to obtain clean images. For thresholding, the images are converted into binary images, with red and green representing the strong and weak thresholds, respectively. In this study, dual thresholding is applied to reduce the sensitivity to residual image noise. After thresholding, some voxels can be isolated if they are not connected to a voxel of the same binary value. Therefore, filling holes can help turning background voxels completely enclosed by foreground voxels into foreground voxels. In the fourth step, labeling is performed on the segmented images to assign a proper name to each particle based on foreground pixels in the binary image. For calculating the MO of a particle, the closest distance to the border of the particle is determined. This step is called the distance map. Additionally, after labeling, there is a remaining inter-connectivity between the particles due to the limited contrast or resolution of scanning, particle separation can be performed on the distance map of the

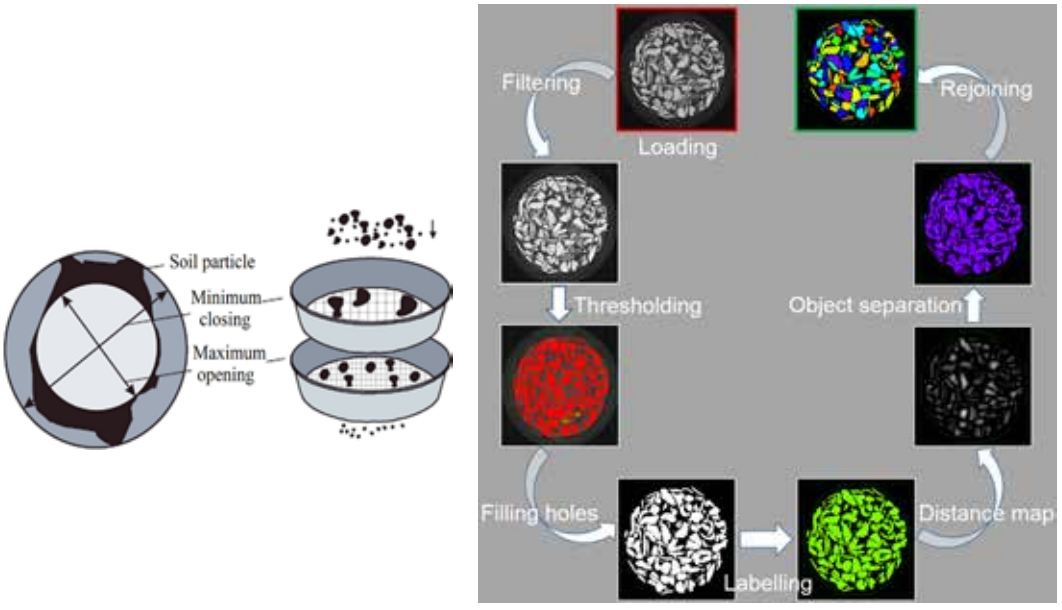

Figure 2. 3D analysis: (a) definition of MO and MC illustrated by Cnudde et al. [31], (b) Flow-chart of 3D analysis.

objects. In the final step, after separation, the software allows the manual rejoining or deleting of separated particles, or applying a smart rejoin operation. These steps are also described in previous studies [30, 33].

After rejoining, a script file of particles can be created that saves the particle properties, such as the number of particles; width, height, depth and volume of particles; equivalent ellipsoid; equivalent diameter; MC; MO; surface and SPH. The output data is extracted using MATLAB, and then transferred to Excel to perform the analysis efficiently.

2.2.4 3D visualization

The database of the 3D analysis is visualized by the package software Octopus 3D Viewer. The particles are rendered in arbitrary colors to present the contrast among individual particles with the different colors showing a variation of SPH (see Figure 6).

2.2.5 Direct shear tests

The second scope is to study the influence of particle morphology (shape and size) on the shear strength properties of calcareous sand and is conducted by direct shear tests. All the tested samples are molded into a metal shear box of 60 × 60 mm and 32.2 mm in height, consolidated at various normal stresses (50, 100, and 200 kPa), and sheared at a constant strain rate of 0.07815 mm/min. Due to the limit of horizontal displacement, all the tests are sheared up to 10% of the shear strain, which are considered as the residual shear strengths.

Two series of direct shear tests are performed. For series 1, the effects of particle shape and material composition of the silica sand (Mol) and the artificial calcareous sand (SMol) are studied. For series 2, the tests are performed on five fractions of S sand with different D_{50}. In the study, the Mohr-Coulomb failure criterion is used to obtain the peak and residual shear strength and internal friction angle of the sands. The dilation angle (ψ) is expressed by the ratio of incremental vertical displacement δ_y to the horizontal incremental displacement δ_x ($\tan\psi = \delta_y/\delta_x$). After shearing, a sieve analysis is also performed to determine possible crushing of the particles of the tested samples.

3 RESULTS AND DISCUSSION

3.1 3D particle shape

The distribution of the particle shape is plotted in Figure 3. In this figure, a significant difference in shape index for the same fraction of particles (160-250 μm) between silica sand (Mol) and calcareous sand (S2) is seen. The shape index in the Mol sand is found to be higher than that in S2. However, it is not easy to see the difference in the particle shape between the test samples due to the difference in the number of particles (N). Therefore, the percentage of particle shapes in each sample is demonstrated as in Figure 4. In Figure 4, the silica sample (Mol) contains more spheres and blades compared to rods and discs. In calcareous sand, the blades appear the most,

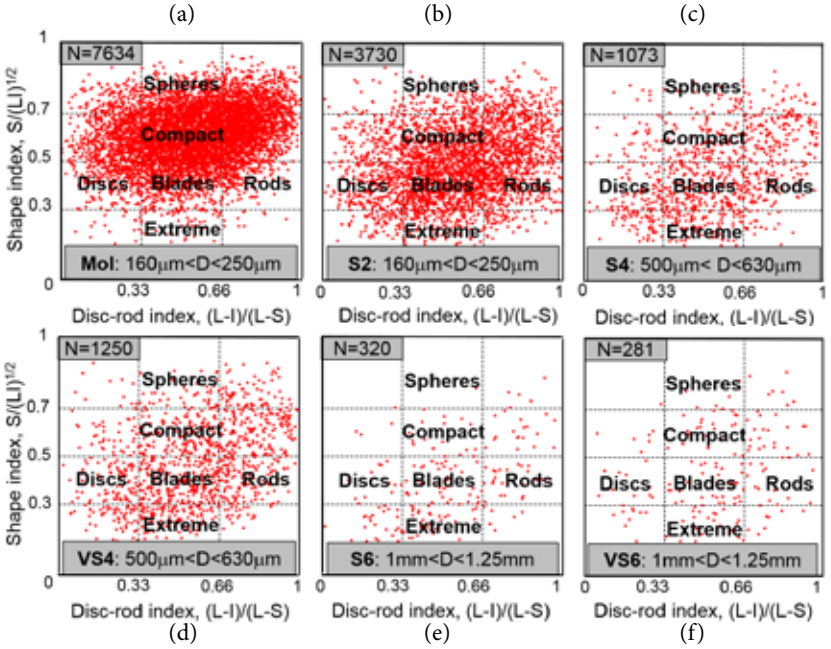

Figure 3. Form diagram of the tested samples (N is number of particles).

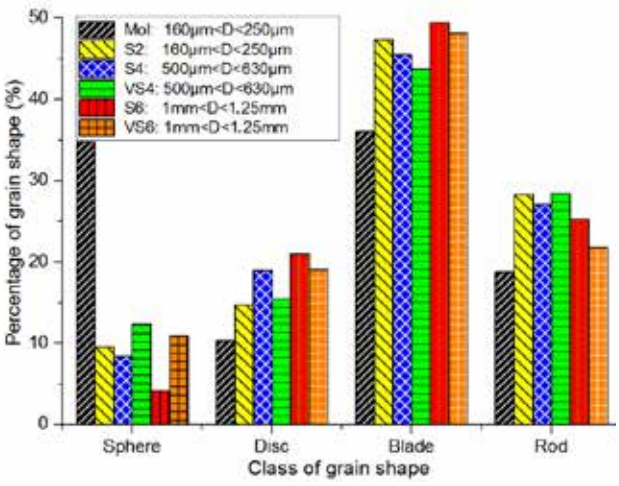

Figure 4. Percentage of grain shape.

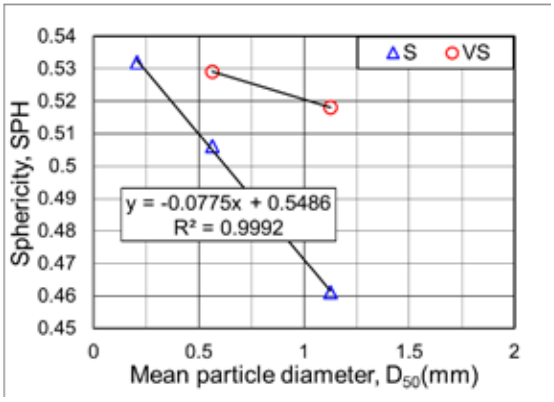

Figure 5. Relationship between sphericity and mean particle diameter.

followed by rods, discs and spheres. For S sand, the fraction of smaller particles tends to contain more spheres and rods and fewer discs than the fraction of larger particles. This is also found for the crushed samples (VS4 and VS6).

The main purpose of this 3D analysis is to determine the relationship between the grain shape and size for calcareous sand. Therefore, the average SPH of each sample and the mean grain size obtained by sieve analysis (SA) are given in Figure 5. It is observed from Figure 5 that the SPH increases with a decrease in the grain size. The best-fit curve is represented by a linear trend line, as shown in Eq. 1, with a very good coefficient of determination (R2 ≈1) for S sand.

$$SPH = -0.0775^{*} D_{50} + 0.5486 \qquad (1)$$

Further, Figure 5 shows that at the same particle sizes (500–630 μm and 1–1.25 mm) the crushed samples (VS4, VS6) give higher values of SPH than the S samples (S4, S6). In particular, both sands (S, VS) seem to have an equivalent SPH for small particles (D < 0.167 mm).

Figure 6 demonstrates the 3D rendered images of all the tested samples with the corresponding SPH values. The average SPH value in each sample is also mentioned in Figure 6.

In addition, the results of the 3DA are compared to those of the sieve analysis (SA). In Figure 7, it is clear that there is a significant difference in the grain size obtained with the two methods, in particular for calcareous sand. The 3DA gives smaller values of particle sizes than the SA. Figure 7 also shows a greater difference for the fraction of larger particles (smaller SPH). Apart from errors due to resolution that may occur in the 3D

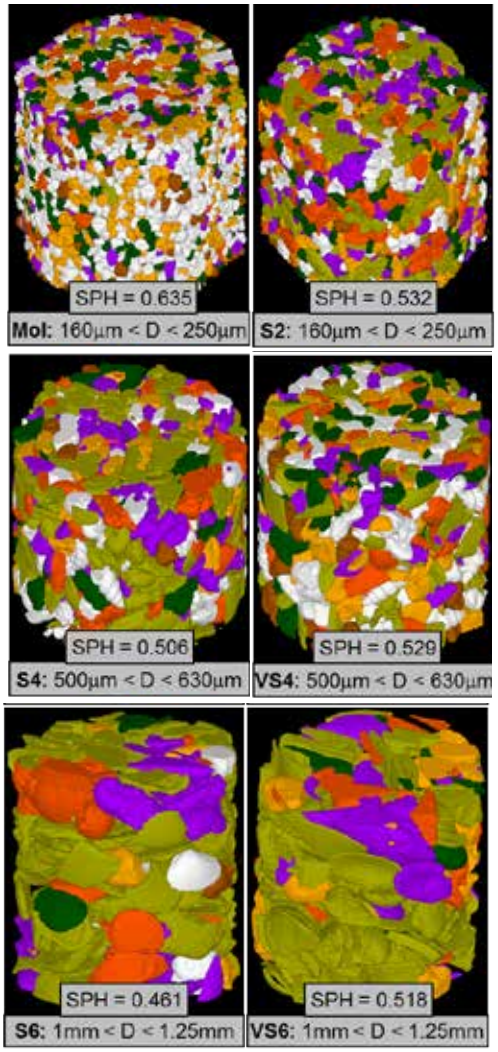

Figure 6. Simulated samples of silica and calcareous sands with 3D rendered by Octopus visualization.

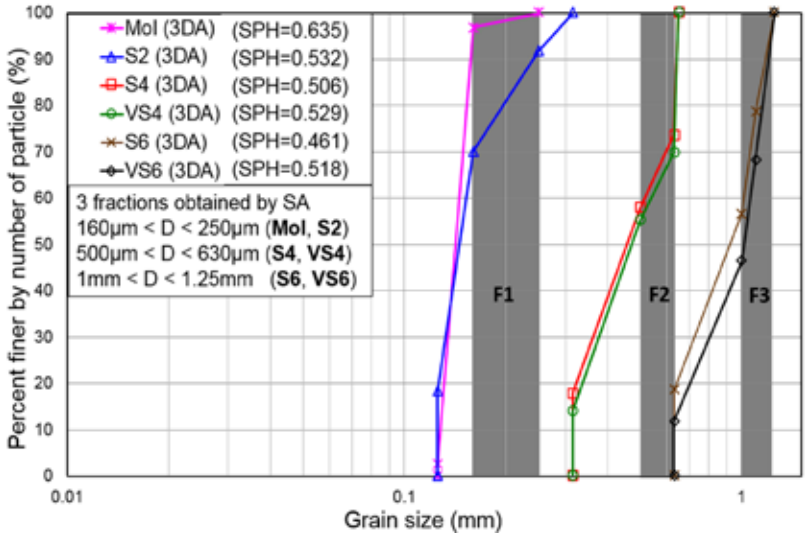

Figure 7. Comparison between 3DA and SA.

method, the difference between the results of SA and 3DA is mainly due to the effect of particle shape in this study. Namely, some particles can pass through the sieve by their intermediate or longest dimension, and particles are retained on the sieve owing to particle interlocking caused by various particle shapes. In this case, it can be concluded that the particle shape has an influence on the SA results. The difference in grain size distribution curves obtained by the 3DA between the VS and S samples are also presented in Figure 7. The difference becomes smaller in a smaller particle range. The results of the 3DA show that the VS samples (VS4, VS6) have larger particles than the S samples (S4, S6), but the VS samples have higher values of SPH. This means that after crushing the particle shape of calcareous sand tends to become more spherical, and the number of particles like blades or discs decreases (Figure 4).

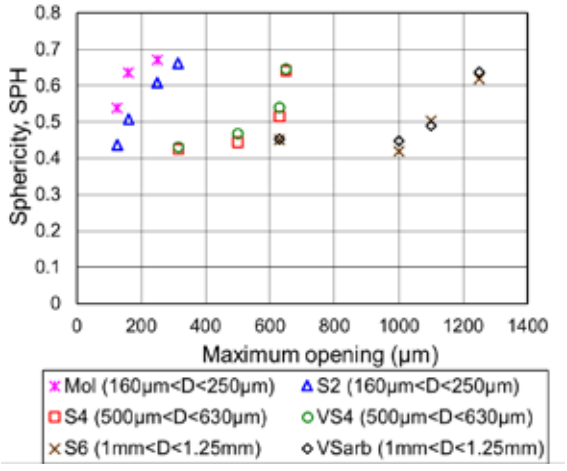

Figure 8. Relationship between sphericity and grain size (MO).

Figure 8 displays the relationship between SPH and MO for each sample. The results show that there is a similar tendency in each sample with MO increasing with an increasing SPH. It is noted that particles with greater SPHs pass through a sieve more easily. As a result, in each sample the smaller particles have lower SPHs than the larger particles.

It is known that the void ratio is dependent on the shape of the particles. In this study, the determination of the maximum and minimum void ratios is considered as an alternative method to see the effect of particle shape on density. The results conducted according to the Japanese Geotechnical Society standard JIS A 1224, 2009 [34] are shown in Table 1. It is clear that the void ratios of SMol are higher than that of Mol sand. This is a reasonable result and once again confirms the results of the 3DA as the void ratios (e_{max} and e_{min}) decrease with increasing SPH.

3.2 Effects of particle characteristics on shear strength properties

The results of the direct shear tests are plotted as shear stress versus shear strain, and as vertical displacement against shear strain (Figure 9). Table 2 summarizes all the results of the direct shear tests. The void ratio and relative density after the consolidation of each tested sample are mentioned in the table. Based on the results of the sieve analysis, there is no crushing after shearing in all the tested samples.

3.2.1 Comparison of calcareous and silica sands

The comparison of the test results of Mol and SMol sands for medium and dense samples (D_r = 40%, D_r =

Table 2. Direct shear test results.

Sample	Normal stress σ'_v (kPa)	Dry density ρ_d (g/cm3)	Void ratio e	Relative density, D_r (%)	Peak shear strength, τ_p (kPa)	Peak friction angle, ϕ_p (°)	Residual shear strength, τ_r (kPa)	Residual friction angle, ϕ_r (°)	Maximum dilation angle, ψ_{max} (°)
SMol	50	1.315	1.119	44.6	-	-	30	30.9	5.4
	100	1.323	1.106	47.0	-	-	63	32.1	6.3
	200	1.331	1.094	49.5	-	-	137	34.5	1.6
	50	1.445	0.928	82.8	40	38.6	38	36.9	11.2
	100	1.450	0.922	84.1	74	35.3	71	35.2	7.0
	200	1.463	0.904	87.6	167	39.9	157	38.1	2.3
Mol	50	1.486	0.774	44.7	-	-	28	28.4	9.5
	100	1.496	0.762	48.0	-	-	56	29.4	7.6
	200	1.510	0.747	52.5	-	-	116	30.1	4.8
	50	1.604	0.644	81.9	36	36.1	31	31.5	12.7
	100	1.606	0.642	82.4	67	34.0	62	31.7	11.6
	200	1.610	0.638	83.7	148	36.4	135	32.1	13.9
S2	50	1.274	1.187	42.7	-	-	27	28.8	6.7
	100	1.285	1.168	46.9	-	-	63	32.1	5
	200	1.287	1.164	47.8	-	-	142	35.5	-
S3	50	1.243	1.242	41.9	-	-	28	29.2	9.3
	100	1.250	1.229	44.7	-	-	70	35.1	6.7
	200	1.257	1.217	47.3	-	-	146	36.1	-
S4	50	1.196	1.330	44.0	-	-	31	31.7	13.3
	100	1.203	1.317	46.5	-	-	75	36.7	10.8
	200	1.208	1.307	48.5	-	-	157	38.1	-
S5	50	1.114	1.501	43.3	-	-	32	32.9	12.6
	100	1.122	1.485	46.1	-	-	77	37.7	7.1
	200	1.133	1.459	50.6	-	-	163	39.2	-
S6	50	1.086	1.565	44.1	-	-	38	36.9	14.7
	100	1.096	1.543	47.8	-	-	89	41.6	6.7
	200	1.107	1.517	52.1	-	-	181	42.2	-

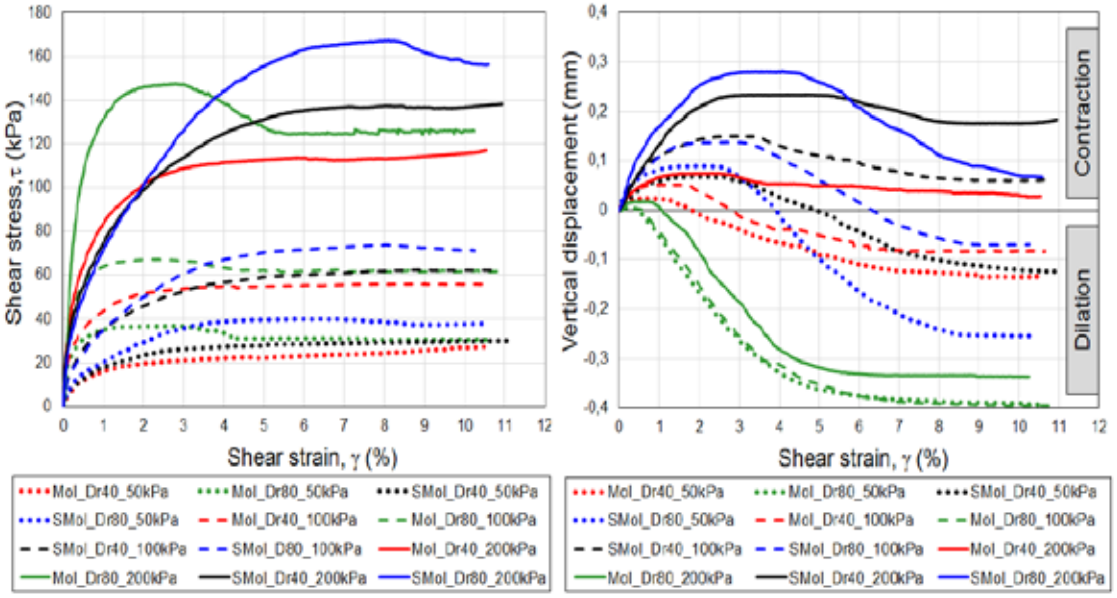

(a) Effect of difference in soil type, especially in particle shape (series 1)

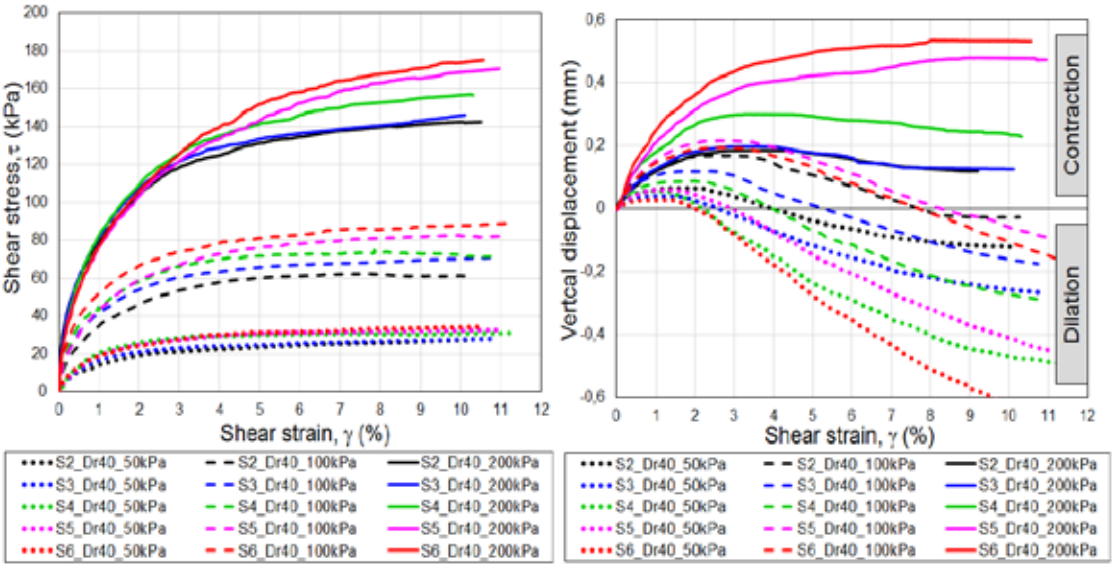

(b) Effect of mean grain size D_{50} (series 2)

Figure 9. Results of direct shear tests.

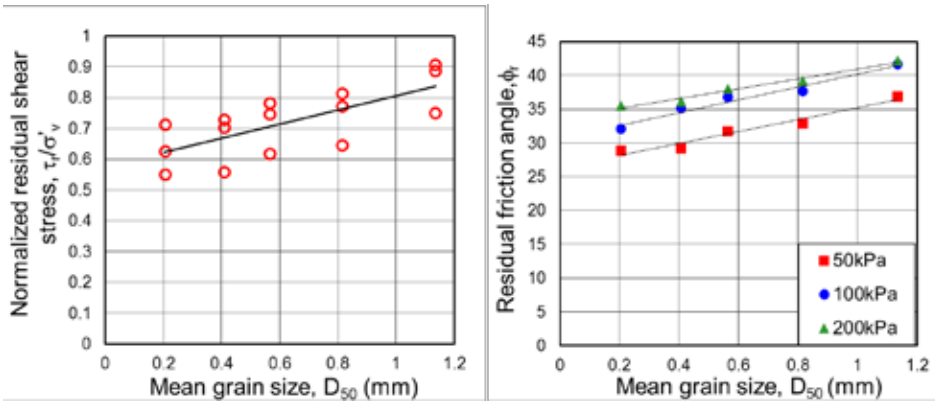

(a) Relationship between shear properties and D_{50}

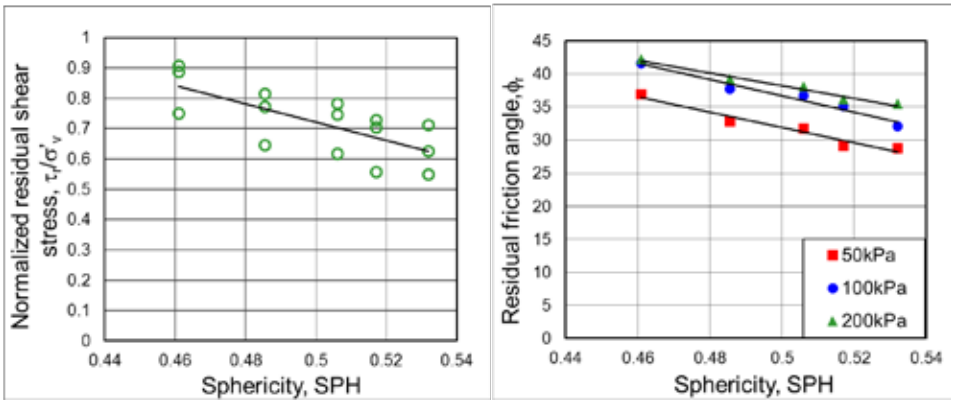

(b) Relationship between shear properties and sphericity (SPH)

Figure 10. Relationship between shear properties and particle characteristics (D_{50}, SPH) at various normal stress for medium dense samples.

80%) are shown in Figure 9a. As expected, an increase in the initial relative density and normal stress leads to an increase in the peak shear stress determined for both sands. In Table 2, the SMol sand has higher shear strengths and friction angles at the peak and residual states than Mol sand. Under constant normal stress, the difference in residual stresses between the samples at 40% and 80% of the initial relative density for Mol sand is less than that in SMol sand. These results indicate that the initial relative densities of the samples have an influence on the shear strength and friction angle at the residual state (γ = 10%), which is significant for calcareous sand. From the literature, the critical state is found to be independent of the initial relative density, suggesting that to reach a critical state in each test, the tests should be performed to a higher shear strain (e. g, γ = 15% or 20%).

Figure 9a further shows that dilation is observed in most of the tests at the end of shearing. The dense samples are found to have a higher dilation than the medium dense samples. Figure 9a strongly indicates that during shearing the volume change response of the samples in both sands is dependent on the normal stress. The greater the loading, the lower the dilation. In addition, Table 2 shows that at similar initial relative densities, the SMol samples with higher void ratios are compressed easily, leading to having smaller dilation angles in comparison with the Mol samples. The maximum dilation angle (ψmax) ranges from 2.3° to 11.2° for the calcareous sand and 4.8° to 13.9° for the silica sand.

Interestingly, although the peak and residual strengths of the SMol samples are higher than those of the Mol samples, the Mol samples reach higher stresses than the SMol samples at small shear strains in the early state of shearing. This trend can be seen clearly in the dense samples (D_r = 80%). It is suggested that the various grain morphologies in the samples leading to greater particle interlocking and an increase in the number of inter-particle contacts causes the increase in shear strength properties for SMol sand, especially during the dilation process.

3.2.2 Effect of mean grain size D_{50} on the shear strength properties

The variation of the shear strength properties with the grain size for calcareous sand is shown in Figure 9b. In all the samples, the shear stress increases and reaches a residual state at γ = 10% without any indication of the peak. As expected, the vertical displacement is found to increase with increasing normal stress for all the samples. For each particle size, the results also show an increase in the residual friction angle at a higher normal stress, as summarized in Table 2. In Figure 9b, it is clear that the sample with larger particles having less SPH and stronger interlocking causes higher shear strength. In addition, the contractive and dilative behaviors of the samples are significantly dependent on normal stress. Although the shear stress reaches a residual state without any indication of the peak, the dilation occurs for the sample with larger particles under low normal stress. Under the normal stress of 50kPa, the sample with larger particles shows much more dilation phase than the sample with smaller particles, indicating that the dilation angle increases with increasing particle size under low load. However, this trend starts to divert under the higher normal stress of 100kPa, and finally, the completely opposite tendency is observed under 200kPa, where the sample of larger particles shows more contraction. This phenomenon is caused by the difference in particle movement, dependent on the particle size, and is explained as follows. Under a low normal stress, the sample with larger particles having greater particle hardness, greater particle angularity (or less particle SPH) and the uniformity of particle size in the sample can provide an interaction between the particles where the contact points of the particle edges (roughness) are strong enough to restrain the particle movement. However, under a higher load, the particle movement increases owing to the contributions of higher void ratio and particle polishing. In short, the volume change of the samples is dependent on the normal stress and the compression or dilation increases with the increase in particle size. Further, the relationship between shear strength properties and particle size is demonstrated in Figure 10a. It is observed that the shear strength and friction angle at residual state increase as the particle size increases for various normal stresses.

3.2.3 Correlations between shear strength properties and sphericity

Using Eq. 1, the SPHs interpolated for other uniform particle sizes are calculated and listed in Table 3.

Table 3. Particle characteristics of the tested sands.

Sand	Sieve size (mm)	D_{50} (mm)	Sphericity, SPH
S2	0.16-0.25	0.205	0.532
S3	0.315-0.5	0.408	0.517
S4	0.5-0.63	0.565	0.506
S5	0.63-1	0.815	0.485
S6	1-1.25	1.135	0.461

The correlations between the shear strength properties and particle shape corresponding to the effect of D_{50} are proposed for the calcareous sand under the various normal stresses (50, 100 and 200 kPa) shown in Figure 10b. The results show that the residual shear strength and friction angle decrease with an increasing SPH. Also, in Figure 10b the best-fit lines of the SPH and friction angle are proposed. The distance between the lines becomes smaller at higher normal stresses (100 and 200 kPa). It can be suggested that the correlations converge to a straight line under high normal stress.

4 CONCLUSIONS

The 3DA on the particles of the calcareous and silica sands is studied based on the data collected using X-ray CT. The particles of calcareous sand are found to show smaller sphericity (SPH) than those of silica and crushed calcareous sands. For calcareous sand, the particle shapes in descending order are blades, rods, discs and spheres; whereas silica sand contains more spheres and blades compared to rods and discs. These findings are consistent with the results obtained from the experiments of the maximum and minimum void ratios of the tested sands. It is proved that the SPH increases with decreasing grain size. However, in each sample, the smaller particles have lower SPH than the larger particles. Further, the 3DA gives smaller particle sizes than the sieve analysis (SA). Particle shape is found to be the main factor affecting the SA results. This is due to particle interlocking caused by various particle shapes, especially for the calcareous sand.

In this study, the correlations between the 3D particle shape and the size (D_{50}) are established. From the direct shear drained test results, the main conclusions can be drawn as follows:

- At the same C_u, the behavior of calcareous and silica sands are quite different. Although the calcareous sand with particles has more angularity and less SPH is formed at a higher void ratio, it gives higher peak and residual shear strength properties and tends to reach a lower shear strength at a small shear strain and a lower dilation than the silica sand. This tendency is seen clearly in the dense sample. The variety of particle shapes increases with the particle interlocking and the number of inter-particle contacts and causes increasing shear strength properties, especially during the dilation process.
- For calcareous sand, the increase in the particle size D_{50} leads to the growth in shear strength properties in the residual state. The compression and dilation curves of the calcareous sands are affected strongly by the normal stress. The range of compression and dilation phases increases with increasing particle size. The sample with larger particles, showing less particle movement for re-arrangement under low stress, causes more dilation, whereas the sample with smaller particles giving less particle movement under high stress shows less compression.
- The critical state may not be reached in this study. This supposes that the ultimate state for calcareous sand can be indicated at higher shear strain than silica sand.

REFERENCES

[1] Hassanlourad, M., Rasouli, M.R., Salehzadeh, H. 2014. A comparison between the undrained shear behavior of carbonate and quartz sands. Int. J. Civ. Eng. 12, 4, 338–350.

[2] Safinus, S., Hossain, M.S., Randolph, M.F. 2013. Comparison of stress-strain behaviour of carbonate and silicate sediments. Proc. 18th Int. Conf. on Soil Mechanics and Geotechnical Engineering, pp. 267–270.

[3] Brandes, H.G. 2011. Simple shear behavior of calcareous and quartz sands. Geotech. Geol. Eng. 29, 1, 113–126. DOI: 10.1007/s10706-010-9357-x

[4] Cho, G.C., Dodds, J., Santamarina, J.C. 2006. Particle shape effects on packing density, stiffness, and strength: natural and crushed sands. J. Geotech. Geoenvironmental Eng. 132, 5, 591–602. DOI: 10.1061/(ASCE)1090-0241(2006)132:5(591)

[5] Bui, M.T., Clayton, C.R.I., Priest, J.A. 2007. Effects of particle shape on Gmax of geomaterials. Proc. 4th Int. Conf. on Earthquake Geotechnical Engineering, No. 1536.

[6] Siang, A.J.L.M., Wijeyesekera, D.C., Zainorabidin, A., and Bakar, I. 2012. The effects of particle morphology (shape and sizes) characteristics on its engineering behaviour and sustainable engineering performance of sand. Int. J. Integr. Eng. 4, 3, 27–37.

[7] Miura, K., Maeda, K., Furukawa, M., Toki, S. (1998). Mechanical characteristics of sands with different primary properties. Soils Found. 38, 4, 159–172.

[8] Pettijohn, F.J., Lundahl, A.C. 1943. Shape and roundness of Lake Erie beach sands. J. Sediment. Res. 13, 2, 69–78. DOI: 10.1306/D426919D-2B26-11D7-8648000102C1865D

[9] Pollack, J.M. 1961. Significance of compo-

sitional and textural properties of South Canadian River channel sands, New Mexico, Texas, and Oklahoma. J. Sediment. Res. 31, 1, 15–37. DOI: 10.1306/74D70AEC-2B21-11D7-8648000102C1865D

[10] Das, N., Ashmawy, A.K. 2007. Relationship between grain size and shape of natural and crushed sand. Proc. of Geo-Denver 2007, New Peaks in Geotechnics, Denver, Colorado, United States, pp. 1–10. DOI: 10.1061/40917(236)25

[11] Barrett, P.J. 1980. The shape of rock particles: a critical review. Sedimentology 27, 3, 291–303. DOI: 10.1111/j.1365-3091.1980.tb01179.x

[12] Dewen, L., Yanrui, K., Dawei, L. 2015. Comparison of grain-size and grain-shape characters of alluvial and lakeshore sands based on dynamic image analysis. Quat. Sci. 35, 2, 484–492.

[13] Sun, Y., Indraratna, B., Nimbalkar, S. 2014. Three-dimensional characterization of particle size and shape for ballast. Geotech. Lett. 4, 197–202. DOI:10.1680/geolett.14.00036

[14] Yan, W.M., Dong, J. 2011. Effect of particle grading on the response of an idealized granular assemblage. Int. J. Geomech. 11, 4, 276–285. DOI: 10.1061/(ASCE)GM.1943-5622.0000085

[15] Lun, A.C.Y. 2011. Influence of grain size distribution on shear strength of sand. UG. Thesis, Universiti Teknologi Malaysia.

[16] Selig, E., Roner, C. 1987. Effects of particle characteristics on behavior of granular material. Transp. Res. Rec. 1131, 1–6.

[17] Madhavi Latha, G., Sitharam, T.G. 2008. Effect of particle size and gradation on the behaviour of granular materials simulated using DEM. Indian Geotech. J. 38, 1, 68–88.

[18] Ueda, T., Matsushima, T., Yamada, Y. 2011. Effect of particle size ratio and volume fraction on shear strength of binary granular mixture. Granul. Matter. 13, 6, 731–742. DOI: 10.1007/s10035-011-0292-1

[19] Pakbaz, M.S., Moqaddam, A.S. 2012. Effect of sand gradation on the behavior of sand-clay mixtures. Int. J. GEOMATE 3, 1, 325–331.

[20] Alias, R., Kasa, A., Taha, M.R. 2014. Particle size effect on shear strength of granular materials in direct shear test. Int. J. Civil. Env. Struct. Constr. Archit. Eng. 8, 11, 733–736.

[21] Li, Y., Huang, R., Chan, L.S., Chen, J. 2013. Effects of particle shape on shear strength of clay-gravel mixture. KSCE J. Civ. Eng. 17, 4, 712–717. DOI: 10.1007/s12205-013-0003-z

[22] Kara, E.M. 2013. Contribution of particles size ranges to sand friction. Eng. Technol. Appl. Sci. Res. 3, 4, 497–501.

[23] Vangla, P., Madhavi, G. 2015. Influence of particle size on the friction and interfacial shear strength of sands of similar morphology. Int. J. Geosynth. Gr. Eng 1, 1, 1–12. DOI: 10.1007/s40891-014-0008-9

[24] Desrosiers, R., Silva, A.J. 2002. Strength behavior of marine sands at elevated confining stresses. Mar. Georesources Geotechnol. 20, 1, 1–19. DOI: 10.1080/106411902753556834

[25] Ghionna, V.N., Caridi, G., Porcino, D. 2008. Undrained monotonic and cyclic simple shear behaviour of carbonate sand. Géotechnique 58, 8, 635–644. DOI: 10.1680/geot.2007.00036

[26] Cabalar, A.F., Dulundu, K., Tuncay, K. 2013. Strength of various sands in triaxial and cyclic direct shear tests. Eng. Geol. 156, 92–102. DOI: 10.1016/j.enggeo.2013.01.011

[27] Potticary, M., Zervos, A., Harkness, J. 2016. The Effect of particle elongation on the strength of granular materials. Proc. 24th UK Conf. Association for Computational Mechanics in Engineering, pp. 31–34.

[28] ASTM D 4253-00. 2006. Standard test methods for maximum index density and unit weight of soils using a vibratory table. ASTM International, West Conshohocken, PA, USA.

[29] Masschaele, B.C., Cnudde, V., Dierick, M., Jacobs, P., Van Hoorebeke, L., Vlassenbroeck, J. 2007. UGCT: New X-ray radiography and tomography facility. Nucl. Instruments Methods Phys. Res., Section A: Accelerators, Spectrometers, Detectors and Associated Equipment 580, 1, 266–269. DOI: 10.1016/j.nima.2007.05.099

[30] Vlassenbroeck, J., Dierick, M., Masschaele, B., Cnudde, V., Van Hoorebeke, L., Jacobs, P. 2007. Software tools for quantification of X-ray microtomography at the UGCT. Nucl. Instruments Methods Phys. Res., Section A: Accelerators, Spectrometers, Detectors and Associated Equipment 580, 1, 442–445. DOI: 10.1016/j.nima.2007.05.073

[31] Cnudde, V., Dewanckele, J., De Boever, W., Brabant, L., De Kock, T. 2012. 3D characterization of grain size distributions in sandstone by means of X-ray computed tomography. Quant. Mineral. Microanal. Sediments Sediment. Rocks 42, 99–113.

[32] Illenberger, W.K. 1991. Pebble shape (and size!). J. Sediment. Res. 61, 5, 756–767. DOI: 10.1306/D42677C6-2B26-11D7-8648000102C1865D

[33] Brabant, L., Vlassenbroeck, J., De Witte, Y., Cnudde, V., Boone, M., Dewanckele, J., Van Hoorebeke, L. 2011. Three-dimensional analysis of high-resolution X-ray computed tomography data

with Morpho+. Microscopy and Microanalysis 17, 2, 252–63. DOI: 10.1017/S1431927610094389

[34] JIS A 1224. 2009. Test method for minimum and maximum densities of sands. Japanese Geotechnical Society, Soil Testing Standards, Tokyo, pp.136-138.

NAVODILA AVTORJEM

Vsebina članka

Članek naj bo napisan v naslednji obliki:

- Naslov, ki primerno opisuje vsebino članka in ne presega 80 znakov.
- Izvleček, ki naj bo skrajšana oblika članka in naj ne presega 250 besed. Izvleček mora vsebovati osnove, jedro in cilje raziskave, uporabljeno metodologijo dela, povzetek izidov in osnovne sklepe.
- Največ 6 ključnih besed, ki bi morale biti napisane takoj po izvlečku.
- Uvod, v katerem naj bo pregled novejšega stanja in zadostne informacije za razumevanje ter pregled izidov dela, predstavljenih v članku.
- Teorija.
- Eksperimentalni del, ki naj vsebuje podatke o postavitvi preiskusa in metode, uporabljene pri pridobitvi izidov.
- Izidi, ki naj bodo jasno prikazani, po potrebi v obliki slik in preglednic.
- Razprava, v kateri naj bodo prikazane povezave in posplošitve, uporabljene za pridobitev izidov. Prikazana naj bo tudi pomembnost izidov in primerjava s poprej objavljenimi deli.
- Sklepi, v katerih naj bo prikazan en ali več sklepov, ki izhajajo iz izidov in razprave.
- Vse navedbe v besedilu morajo biti na koncu zbrane v seznamu literature, in obratno.

Dodatne zahteve

- Vrstice morajo biti zaporedno oštevilčene.
- Predložen članek ne sme imeti več kot 18 strani (brez tabel, legend in literature); velikost črk 12, dvojni razmik med vrsticami. V članek je lahko vključenih največ 10 slik. Isti rezultati so lahko prikazani v tabelah ali na slikah, ne pa na oba načina.
- Potrebno je priložiti imena, naslove in elektronske naslove štirih potencialnih recenzentov članka. Urednik ima izključno pravico do odločitve, ali bo te predloge upošteval.

Enote in okrajšave

V besedilu, preglednicah in slikah uporabljajte le standardne označbe in okrajšave SI. Simbole fizikalnih veličin v besedilu pišite poševno (npr. *v*, *T* itn.). Simbole enot, ki so sestavljene iz črk, pa pokončno (npr. Pa, m itn.). Vse okrajšave naj bodo, ko se prvič pojavijo, izpisane v celoti.

Slike

Slike morajo biti zaporedno oštevilčene in označene, v besedilu in podnaslovu, kot sl. 1, sl. 2 itn. Posnete naj bodo v katerem koli od razširjenih formatov, npr. BMP, JPG, GIF. Za pripravo diagramov in risb priporočamo CDR format (CorelDraw), saj so slike v njem vektorske in jih lahko pri končni obdelavi preprosto povečujemo ali pomanjšujemo.

Pri označevanju osi v diagramih, kadar je le mogoče, uporabite označbe veličin (npr. *v*, *T* itn.). V diagramih z več krivuljami mora biti vsaka krivulja označena. Pomen oznake mora biti razložen v podnapisu slike.

Za vse slike po fotografskih posnetkih je treba priložiti izvirne fotografije ali kakovostno narejen posnetek.

Preglednice

Preglednice morajo biti zaporedno oštevilčene in označene, v besedilu in podnaslovu, kot preglednica 1, preglednica 2 itn. V preglednicah ne uporabljajte izpisanih imen veličin, ampak samo ustrezne simbole. K fizikalnim količinam, npr. *t* (pisano poševno), pripišite enote (pisano pokončno) v novo vrsto brez oklepajev. Vse opombe naj bodo označene z uporabo dvignjene številke[1].

Seznam literature

Navedba v besedilu

Vsaka navedba, na katero se sklicujete v besedilu, mora biti v seznamu literature (in obratno). Neobjavljeni rezultati in osebne komunikacije se ne priporočajo v seznamu literature, navedejo pa se lahko v besedilu, če je nujno potrebno.

Oblika navajanja literature

V besedilu: Navedite reference zaporedno po številkah v oglatih oklepajih v skladu z besedilom. Dejanski avtorji so lahko navedeni, vendar mora obvezno biti podana referenčna številka.

Primer: »..... kot je razvidno [1,2]. Brandl and Blovsky [4], sta pridobila drugačen rezultat…«

V seznamu: Literaturni viri so oštevilčeni po vrstnem redu, kakor se pojavijo v članku. Označimo jih s številkami v oglatih oklepajih.

Sklicevanje na objave v revijah:

[1] Jelušič, P., Žlender, B. 2013. Soil-nail wall stability analysis using ANFIS. Acta Geotechnica Slovenica 10(1), 61-73.

Sklicevanje na knjigo:
[2] Šuklje, L. 1969. Rheological aspects of soil mechanics. Wiley-Interscience, London
Sklicevanje na poglavje v monografiji:
[3] Mitchel, J.K. 1992. Characteristics and mechanisms of clay creep and creep rupture, in N. Guven, R.M. Pollastro (eds.), Clay-Water Interface and Its Rheological Implications, CMS Workshop Lectures, Vol. 4, The clay minerals Society, USA, pp. 212-244..
Sklicevanje na objave v zbornikih konferenc:
[4] Brandl, H., Blovsky, S. 2005. Slope stabilization with socket walls using the observational method. Proc. Int. conf. on Soil Mechanics and Geotechnical Engineering, Bratislava, pp. 2485-2488.
Sklicevanje na spletne objave:
[5] Kot najmanj, je potrebno podati celoten URL. Če so poznani drugi podatki (DOI, imena avtorjev, datumi, sklicevanje na izvorno literaturo), se naj prav tako dodajo.

Podatki o avtorjih

Članku priložite tudi podatke o avtorjih: imena, nazive, popolne poštne naslove, številke telefona in faksa, naslove elektronske pošte. Navedite kontaktno osebo.

Sprejem člankov in avtorske pravlce

Uredništvo si pridržuje pravico do odločanja o sprejemu članka za objavo, strokovno oceno mednarodnih recenzentov in morebitnem predlogu za krajšanje ali izpopolnitev ter terminološke in jezikovne korekture. Z objavo preidejo avtorske pravice na revijo ACTA GEOTECHNICA SLOVENICA. Pri morebitnih kasnejših objavah mora biti AGS navedena kot vir.

Vsa nadaljnja pojasnila daje:

Uredništvo
ACTA GEOTECHNICA SLOVENICA
Univerza v Mariboru,
Fakulteta za gradbeništvo, prometno inženirstvo in arhitekturo
Smetanova ulica 17, 2000 Maribor, Slovenija
E-pošta: ags@uni-mb.si

INSTRUCTIONS FOR AUTHORS

Format of the paper

The paper should have the following structure:

- A Title, which adequately describes the content of the paper and should not exceed 80 characters;
- An Abstract, which should be viewed as a mini version of the paper and should not exceed 250 words. The Abstract should state the principal objectives and the scope of the investigation and the methodology employed; it should also summarise the results and state the principal conclusions;
- Immediately after the abstract, provide a maximum of 6 keywords;
- An Introduction, which should provide a review of recent literature and sufficient background information to allow the results of the paper to be understood and evaluated;
- A Theoretical section;
- An Experimental section, which should provide details of the experimental set-up and the methods used to obtain the results;
- A Results section, which should clearly and concisely present the data, using figures and tables where appropriate;
- A Discussion section, which should describe the relationships shown and the generalisations made possible by the results and discuss the significance of the results, making comparisons with previously published work;
- Conclusions, which should present one or more conclusions that have been drawn from the results and subsequent discussion;
- A list of References, which comprises all the references cited in the text, and vice versa.

Additional Requirements for Manuscripts

- Use double line-spacing.
- Insert continuous line numbering.
- The submitted text of Research Papers should cover no more than 18 pages (without Tables, Legends, and References, style: font size 12, double line spacing). The number of illustrations should not exceed 10. Results may be shown in tables or figures, but not in both of them.
- Please submit, with the manuscript, the names, addresses and e-mail addresses of four potential referees. Note that the editor retains the sole right to decide whether or not the suggested reviewers are used.

Units and abbreviations

Only standard SI symbols and abbreviations should be used in the text, tables and figures. Symbols for physical quantities in the text should be written in Italics (e.g. *v*, *T*, etc.). Symbols for units that consist of letters should

be in plain text (e.g. Pa, m, etc.).
All abbreviations should be spelt out in full on first appearance.

Figures

Figures must be cited in consecutive numerical order in the text and referred to in both the text and the caption as Fig. 1, Fig. 2, etc. Figures may be saved in any common format, e.g. BMP, JPG, GIF. However, the use of CDR format (CorelDraw) is recommended for graphs and line drawings, since vector images can be easily reduced or enlarged during final processing of the paper.

When labelling axes, physical quantities (e.g. *v*, *T*, etc.) should be used whenever possible. Multi-curve graphs should have individual curves marked with a symbol; the meaning of the symbol should be explained in the figure caption. Good quality black-and-white photographs or scanned images should be supplied for the illustrations.

Tables

Tables must be cited in consecutive numerical order in the text and referred to in both the text and the caption as Table 1, Table 2, etc. The use of names for quantities in tables should be avoided if possible: corresponding symbols are preferred. In addition to the physical quantity, e.g. *t* (in Italics), units (normal text), should be added on a new line without brackets.
Any footnotes should be indicated by the use of the superscript[1].

LIST OF references

Citation in text

Please ensure that every reference cited in the text is also present in the reference list (and vice versa). Any references cited in the abstract must be given in full. Unpublished results and personal communications are not recommended in the reference list, but may be mentioned in the text, if necessary.

Reference style

Text: Indicate references by number(s) in square brackets consecutively in line with the text. The actual authors can be referred to, but the reference number(s) must always be given:

Example: "... as demonstrated [1,2]. Brandl and Blovsky [4] obtained a different result ..."

List: Number the references (numbers in square brackets) in the list in the order in which they appear in the text.

Reference to a journal publication:
[1] Jelušič, P., Žlender, B. 2013. Soil-nail wall stability analysis using ANFIS. Acta Geotechnica Slovenica 10(1), 61-73.

Reference to a book:
[2] Šuklje, L. 1969. Rheological aspects of soil mechanics. Wiley-Interscience, London

Reference to a chapter in an edited book:
[3] Mitchel, J.K. 1992. Characteristics and mechanisms of clay creep and creep rupture, in N. Guven, R.M. Pollastro (eds.), Clay-Water Interface and Its Rheological Implications, CMS Workshop Lectures, Vol. 4, The clay minerals Society, USA, pp. 212-244.

Conference proceedings:
[4] Brandl, H., Blovsky, S. 2005. Slope stabilization with socket walls using the observational method. Proc. Int. conf. on Soil Mechanics and Geotechnical Engineering, Bratislava, pp. 2485-2488.

Web references:
[5] As a minimum, the full URL should be given and the date when the reference was last accessed. Any further information, if known (DOI, author names, dates, reference to a source publication, etc.), should also be given.

Author information

The following information about the authors should be enclosed with the paper: names, complete postal addresses, telephone and fax numbers and E-mail addresses. Indicate the name of the corresponding author.

Acceptance of papers and copyright

The Editorial Committee of the Slovenian Geotechnical Review reserves the right to decide whether a paper is acceptable for publication, to obtain peer reviews for the submitted papers, and if necessary, to require changes in the content, length or language.
On publication, copyright for the paper shall pass to the ACTA GEOTECHNICA SLOVENICA. The AGS must be stated as a source in all later publication.

For further information contact:

Editorial Board
ACTA GEOTECHNICA SLOVENICA
University of Maribor,
Faculty of Civil Engineering, Transportation Engineering and Architecture
Smetanova ulica 17, 2000 Maribor, Slovenia
E-mail: ags@uni-mb.si

NAMEN REVIJE

Namen revije ACTA GEOTECHNICA SLOVENICA je objavljanje kakovostnih teoretičnih člankov z novih pomembnih področij geomehanike in geotehnike, ki bodo dolgoročno vplivali na temeljne in praktične vidike teh področij.

ACTA GEOTECHNICA SLOVENICA objavlja članke s področij: mehanika zemljin in kamnin, inženirska geologija, okoljska geotehnika, geosintetika, geotehnične konstrukcije, numerične in analitične metode, računalniško modeliranje, optimizacija geotehničnih konstrukcij, terenske in laboratorijske preiskave.

Revija redno izhaja dvakrat letno.

AIMS AND SCOPE

ACTA GEOTECHNICA SLOVENICA aims to play an important role in publishing high-quality, theoretical papers from important and emerging areas that will have a lasting impact on fundamental and practical aspects of geomechanics and geotechnical engineering.

ACTA GEOTECHNICA SLOVENICA publishes papers from the following areas: soil and rock mechanics, engineering geology, environmental geotechnics, geosynthetic, geotechnical structures, numerical and analytical methods, computer modelling, optimization of geotechnical structures, field and laboratory testing.

The journal is published twice a year.

AVTORSKE PRAVICE

COPYRIGHT

ODGOVORNOST

RESPONSIBILITY

9771854017001

Univerza v Mariboru

www.fg.um.si

SLOVENSKO GEOTEHNIŠKO DRUŠTVO • SLOVENIAN GEOTECHNICAL SOCIETY

www.sloged.si

Univerza v Ljubljani

Fakulteta za gradbeništvo in geodezijo

Naravoslovnotehniška Fakulteta

www.fgg.uni-lj.si
www.ntf.uni-lj.si

SLOVENSKO DRUŠTVO ZA PODZEMNE GRADNJE

SLOVENIAN SOCIETY FOR UNDERGROUND STRUCTURES

www.ita-slovenia.si